Multirotor Whirl Flutter

A semi-analytical approach

D. I. Castillo Capponi

Aerospace Structures & Computational Mechanics





Multirotor Whirl Flutter

A semi-analytical approach

by

D. I. Castillo Capponi

to obtain the degree of Master of Science at the Delft University of Technology, to be defended publicly on Tuesday June 29, 2022 at 15:00.

Student number: 5139600

Project duration: September 1, 2021 – June 29, 2022

Thesis committee: Dr. J. Sodja, TU Delft, Supervisor

Dr. ir. R. De Breuker,
Dr. ir. T. Sinnige,
TU Delft, Chair
TU Delft, Examiner
TU Delft, Examiner
TU Delft, Examiner



Preface

This thesis report represents the work carried out in the last part of my MSc in Aerospace Engineering. It was a long process, with highs and lows, and it would not have been possible without the support of all the people that surrounded me during this process.

First, I want to thank my supervisors Prof. Jurij Sodja and Roeland De Breuker for their guidance and support throughout the thesis. Their insight helped and motivated me to tackle the most difficult tasks of the thesis project. Also I want to thank them for telling me take a break sometimes and guide me to look at the problem from another perspective.

I also want to thank my family for the support in the last years, to my parents and brothers for the conversations that helped me to get through when I was fustrated, and also to the family holidays that brought me new energy and motivation. A special mention to my oldest brother Pablo, who helped me with the engineering and mathematics of some of the most difficult parts of the thesis project.

Finally, I would like to thank Heike, who was very supportive during the process, in the good and bad times. Also, I'm grateful of my friends and volleyball team that were always there when I needed someone to talk or to get distracted.

D. I. Castillo Capponi Delft, June 2022

Abstract

In the last few years, a new aircraft configuration has been developed: the electric Vertical Take-off/Landing aircraft (eVTOL). To improve aircraft efficiency, structures are lighter and more flexible, and therefore are prone to aeroelastic interaction with the aerodynamic forces. Due to the structure's flexible nature and the use of propellers for propulsion, eVTOL aircraft are prone to whirl flutter, which consists of a dynamic instability produced by the propeller aerodynamics and structure interaction.

This thesis aims to assess whirl flutter in a multirotor VTOL, considering rigid propellers in thrusting conditions. A semi-analytical model was developed for two types of configurations: one propeller and two counter-rotating propellers at the tip of a cantilever beam structure. The model is comprised of three parts: steady propeller aerodynamics, unsteady whirl forces and structure dynamics.

The steady propeller aerodynamics in thrust conditions were obtained through blade element momentum theory (BEMT) for a rigid propeller. Some modifications were included on the BEMT to account for the effects of the front propeller on the rear propeller in a counter-rotating configuration. The BEMT flow characteristics were coupled to a quasi-steady aerodynamics perturbation model using strip theory, based on Houbolt and Reed [1]. The model includes lift and drag effects of the blades to obtain the forces produced by the whirl motion of the propeller. Rotational symmetry was used to obtain the propeller whirl forces.

Additionally, the beam structure was modeled using a space frame finite element model with 12 degrees of freedom per element, in combination with an independent two-degrees of freedom system model of the propeller-pylon structure. Then, the structure dynamics were derived for the propeller-pylon structure and included in the system structural dynamics. Afterward, the unsteady whirl forces were coupled to the structural dynamics using state-space representation, which allowed the stability analysis of the system using eigenanalysis.

The model developed in this thesis was used to analyze whirl flutter on an octocopter designed by the company Betronka SPA for all the designed flight conditions. The flow was considered to be always perpendicular to the propeller plane of rotation and the only independent variables were the inflow velocity and propeller angular velocity. Afterward, to study the thrust influence on whirl flutter, flow velocities and propeller angular velocities above the designed limit were studied, in order to find the main trends of thrust effects for conventional and counter-rotating configurations.

The main findings of the stability analysis show that the evaluated multirotor does not suffer from whirl flutter for both configurations (conventional and counter-rotating propellers). The counter-rotating propeller configuration is more stable compared to the default configuration, increasing the whirl flutter speeds. Thrust conditions stabilize the default configuration, increasing the propeller angular speed to encounter whirl flutter by 4%. It was also found that thrust conditions are negligible for counter-rotating propeller configuration considering variable angular velocity. On the contrary, thrust effects are destabilizing for both configurations when considering variable propeller inflow speed.

Contents

		-
Stat 2.1	of the art review3Whirl Flutter32.1.1 Whirl flutter accidents42.1.2 Whirl flutter model42.1.3 Whirl flutter aerodynamics62.1.4 Influence of major parameters in whirl flutter82.1.5 Thrust effect92.1.6 Tiltrotor whirl flutter9Propeller aerodynamics102.2.1 Blade element momentum theory122.2.2 Counter rotating propellers BEMT12	3 3 4 4 6 8 9 9 1 2
Pro	eller aerodynamics	5
3.1	Blade element momentum theory (BEMT) 3.1.1 Momentum theory 3.1.2 Blade element theory 3.1.3 Correction factors 3.1.4 Extrapolation of lift and drag coefficients for an airfoil 3.1.5 Final equations 3.1.6 Validation of BEMT 3.1.7 Extension of BEMT to counter-rotating propellers Whirl flutter aerodynamics 3.2.1 Perturbation quantities 3.2.2 Propeller unsteady forces using strip theory 3.2.3 Unsteady forces extension for counter-rotating propellers 3.2.4 Comparison with previous models and experiments 3.3.5 Final equations 4.5 Final equations 4.6 Validation of BEMT 4.7 Extension of BEMT 4.8 Sinal equations 4.9 Sinal equations 4.0 Sinal	5 7 3 3 3 4 9 0
4.1	4.1.1 Damping	5
5.1	·	
		
	The state of the s	
	·	
5.2		
5.3	· · · ·	
5 <i>1</i>		
5.4	5.4.1 Mode tracking 47	
	1.1 State 2.1 State 2.1 State 2.1 State 2.2 State 2.3 Struct 3.1 Struct 4.1 State 3.2 Struct 4.1 State 3.2 State 3.2	1.1 Document outline 2 State of the art review 2 2.1 Whirl Flutter 2 2.1.1 Whirl flutter accidents 2 2.1.2 Whirl flutter aerodynamics 6 2.1.3 Whirl flutter aerodynamics 6 2.1.4 Influence of major parameters in whirl flutter 5 2.1.5 Thrust effect 5 2.1.6 Tillrotor whirl flutter 5 2.2 Propeller aerodynamics 10 2.2.1 Blade element momentum theory 11 2.2.2 Counter rotating propellers BEMT 12 2.3 Research Questions and Objectives 13 3.1 Blade element momentum theory (BEMT) 16 3.1.1 Momentum theory 14 3.1.2 Blade element theory 13 3.1.3 Correction factors 16 3.1.4 Extrapolation of lift and drag coefficients for an airfoil 18 3.1.5 Final equations 18 3.1.6 Validation of BEMT 18 3.1.7 Extension of BEMT to counter-rotating propellers 22 3.2 Whirl flutter aerodynamics 22 3.2.2 Propeller unsteady forces using strip theory 23 3.2.3 Unsteady forces extension for counter-rotating propeller

viii Contents

6	Ana	lysis a	nd results	49
	6.1 Octocopter Parameters			49
			Propeller conditions for the multirotor designed flight conditions	
	6.2	Result	s and discussion	52
		6.2.1	Whirl flutter analysis for the multirotor flight conditions	52
		6.2.2	Modal analysis with respect to the inflow velocity	
			Influence of different advance ratios considering variable inflow velocity	56
		6.2.4	Influence of different advance ratios considering variable propeller angular veloc-	
			ity	57
7	Con	clusior	ns	59
Α	Fini	te elem	ent frequency convergence study	61
В	Stru	ctural	mode shapes	63
С	Con	npariso	n between forces using the exact solution for a 2 blades propeller and rota-	
	tion	al symi	metry approximation	65

List of Figures

2.1	Idealized gyroscopic model [21]	4
2.2	Backward mode (a) and forward mode (b) [21]	5
2.3	Stable (a) and unstable gyroscopic oscillation (b) [21]	5
2.4	Whirl forces respect to gyroscopic system degrees of freedom (adapted from [5])	6
	Aerodynamics forces arising from pitching deflection, (c) retreating blade at the left side	Ū
2.5		
	of the propeller propeller disk and (d) advancing blade blade at the right side of the	
	propeller propeller disk [5].	7
2.6	Aerodynamics forces arising from yawing velocity, (c) retreating blade at the left side of	
	the propeller propeller disk and (d) advancing blade blade at the right side of the propeller	
	propeller disk [5]	7
2.7	Aerodynamics forces arising from pitching angular velocity, (c) retreating blade at the	•
2.1		
	top side propeller propeller disk and (d) advancing blade blade at the bottom side of the	_
	propeller propeller disk [5].	8
2.8	Whirl flutter boundary and divergence for different advance ratios [21]	9
2.9	Influences of structural damping and propeller – pivot point distance on whirl flutter (γ is	
	the system structural damping) [21]	10
2 10	Whirl flutter boundary (stiffness remains constant) [21].	11
	Discretization of rotor disk [53].	11
2.12	Blade element diagram [50]	12
3.1	Right: Blade annular elements [53]. Left: propeller stream tube [50].	15
3.2	Blade element diagram.	17
3.3	Lift coefficient C_L of CLARK-Y [71]	
3.4	Drag coefficient C_D of CLARK-Y [71]	20
3.5	Thrust coefficient for propeller C [70]	20
3.6	Power coefficient for propeller C [70]	20
3.7	counter-rotating propeller model (adapted from [65]).	21
3.8	Blade element diagram for a counter-rotating propeller.	22
		23
3.9	Whirl forces of the gyroscopic system [5].	
	Perturbation quantities due to whirl motion.	24
	Model used to get the aerodynamic forces	24
3.12	Front view of the propeller model with four blades	24
3.13	Whirl forces of the propeller related to blade thrust and torque	28
	Comparison for aerodynamic derivative $C_{z,\theta}$	
	Comparison for aerodynamic derivative $C_{m,\psi}$	
	Comparison for aerodynamic derivative $C_{m,q}$	32
3.10	Companson for derodynamic derivative $c_{m,q}$	32
4 1	Frame element degrees of freedom (modified from [76])	33
	Clamped beam model for validation of finite element code	36
4.2	Clamped bearn model for validation of limite element code	30
5.1	Diagram of the aeroelastic model.	40
		_
5.2	Propeller-beam system model	41
5.3	Propeller-beam system degrees of freedom	41
6 1	Simplified model geometry.	49
6.1		
6.2	Simplified model geometry for the counter-rotating configuration	49
	Octocopter beam geometry	50
	Lift coefficient C_L of the propeller airfoil	50
65	Drag coefficient C of the propeller airfoil	50

x List of Figures

6.6	Thrust coefficient C_T against propeller advance ratio J	52
6.7	First bending x-axis damping coefficient for default propeller configuration	53
6.8	First bending x-axis frequency for the default propeller configuration	53
6.9	First bending x-axis damping coefficient for the counter-rotating propeller configuration .	53
	First bending x-axis mode frequency for the counter-rotating propeller configuration	53
	First bending z-axis mode damping coefficient for the default propeller configuration	54
		54
	First bending z-axis frequency for the default propeller configuration	
	First bending z-axis damping coefficient for the counter-rotating propeller configuration .	54
	First bending z-axis frequency for the counter-rotating propeller configuration	54
6.15	Damping coefficient for constant advance ratio $J = 0.12$ and variable inflow velocity for	
	a default propeller configuration	55
6.16	Frequency for constant advance ratio $J = 0.12$ and variable inflow velocity for a default	
	propeller configuration	55
6.17	Mode shape of the unstable mode at the flutter speed	55
	Damping coefficient for constant advance ratio $J = 0.12$ and variable inflow velocity for	
	a counter-rotating propeller configuration	56
6 10	Frequency for constant advance ratio $J = 0.12$ and variable inflow velocity for a counter-	•
0.15	rotating propeller configuration	56
6 20	First bending z-axis mode damping coefficient for different advance ratios <i>J</i> and variable	50
0.20	, ,	5 7
0 04	inflow velocity a default propeller configuration	57
6.21	First bending z-axis mode frequency for different advance ratios <i>J</i> and variable inflow	
	velocity a default propeller configuration	57
6.22	First bending z-axis mode damping coefficient for different advance ratios <i>J</i> and variable	
	inflow velocity for a counter-rotating propeller configuration	57
6.23	First bending z-axis mode frequency for different advance ratios <i>J</i> and variable inflow	
	velocity for a counter-rotating propeller configuration	57
6.24	First bending z-axis mode damping coefficient for different advance ratios <i>J</i> and variable	
	propeller angular velocity for a default propeller configuration	58
6.25	First bending z-axis mode frequency for different advance ratios <i>J</i> and variable propeller	
	angular velocity for a default propeller configuration	58
6.26	First bending z-axis mode damping coefficient for different advance ratios <i>J</i> and variable	
	propeller angular velocity for a counter-rotating propeller configuration	58
6.27	First bending z-axis mode frequency for different advance ratios <i>J</i> and variable propeller	
·	angular velocity for a counter-rotating propeller configuration	58
	angular volocity for a counter rotating propositor consignation	00
A.1	Convergence study for first bending x-axis	61
	Convergence study for first bending z-axis	61
	Convergence study for second bending x-axis	
	Convergence study for second bending z-axis	61
A.5	Convergence study for third bending x-axis	62
_		
A.6	Convergence study for first torsion	62
A.7	Convergence study for third bending z-axis	62
A.8	Convergence study for fourth bending x-axis	62
D 4	Made shape of first handing viewis	63
B.1	Mode shape of first bending x-axis	63
B.2	Mode shape of first bending z-axis	63
B.3	Mode shape of second bending x-axis	63
B.4	Mode shape of second bending z-axis	63
B.5	Mode shape of third bending x-axis	63
B.6	Mode shape of first torsion	63
B.7	Mode shape of third bending z-axis	64
B.8	Mode shape of fourth bending x-axis	64
C.1	Comparison between time domain solution using whirl forces exact solution for 2 blades	
	or symmetry approximation	65
C.2	Relative error between time domain solution using whirl forces exact solution for 2 blades	
	or symmetry approximation	65

List of Tables

4.1	Beam material properties
4.2	Beam parameters
4.3	Static results
4.4	Model and Ansys result comparison
6.1	Aluminum 7075-T6 properties
6.2	Beam parameters of Figure 6.1
6.3	Nacelle properties
6.4	Propeller properties
6.5	Blade geometry

1

Introduction

With the development of electric propulsion, new aircraft design possibilities are now feasible. Air transportation's contribution to the climate change, which is 2% of global CO_2 emissions [2], makes electric and hydrogen propulsion very attractive for the new aircraft generations. In this context, for short-distance transportation, a new concept called "air taxis" is being developed, which provides people with short flights on demand. One of the key features needed for air transport in cities is vertical take off and landing. This can be accomplished by electrically driven vehicles with the capabilities for Vertical Take-off/Landing aircraft (eVTOL) [3].

Different companies have been developing eVTOLs, such as Volocopter, Joby Aviation, Lilium and Airbus. Some of them are in concept development, while others are in the certification stage, such as Joby Aviation.

To improve the efficiency of electrically driven aircraft (propellers and electric motors), the wing aspect ratio can be increased, which reduces the induced drag, and the propellers can be distributed along the aircraft wings to maintain the landing and take-off performance [4]. But, due to the higher wing aspect ratios, higher wing flexibility is expected, and as a consequence, aeroelastic interactions arise between the structure and the aerodynamic forces.

The previously mentioned aeroelastic forces can produce instability problems in the analyzed system, which can be static or dynamic. In the case of wings, the main static aeroelastic instability is torsional divergence [5], while the main dynamic instability is flutter. Flutter can be described as self excited-vibrations that are produced by oscillatory aerodynamic loads that rise from the aeroelastic system [5]. For wings, the flutter phenomena is known as classical flutter, and for a motor nacelle with propellers, the oscillatory dynamic instability is called whirl flutter [6].

Whirl flutter was discovered in 1938 by Taylor and Browne [7] and it gained importance in 1960 due to fatal accidents caused by whirl flutter of a Lockheed L-188C Electra [8]. After the 60s, whirl flutter research continued to develop, considering that other aircraft types, like helicopters and tiltrotors, could suffer from it.

The currently developed whirl flutter models can be divided into two subcategories: analytical and numerical. The former model considers propeller aerodynamics in windmilling conditions, because the influence of thrust on whirl flutter forces is very small at high speeds [5] where whirl flutter is expected to occur in fixed-wing aircraft. On the other hand, numerical methods are needed for other aircraft configurations, such as tiltrotors. This type of aircraft has diverse flight conditions such as hover, transition, and forward flight, and therefore, relies upon complex multibody numerical methods, or CFD-based methods in combination with finite elements models for the assessment of the aeroelastic response of whirl flutter. This is computationally expensive, making it less suitable to implement in the preliminary phase of the design.

Now, with the "electric boom" in aviation, whirl flutter will have a big impact on the development of the new aircraft concepts. Propeller size and number can largely vary in these new designs, which will change the whirl flutter behavior of the aircraft. Therefore, it is desirable to assess whirl flutter in an early stage, so the design can consider whirl flutter restrictions when optimized and modified. To be able to include this instability in an early design stage or for concept optimization, the model needs to be fast and have low-computational costs.

2 1. Introduction

In this context, a new eVTOL concept has been studied, called multirotor aircraft. To improve the efficiency and assess the safety of this aircraft, whirl flutter should be analyzed. Multirotor aircraft do not operate just in the high speed region, but instead, they have a large variety of flight modes [9], relying on the propellers' thrust to achieve the vehicle lift and thrust. Therefore, to assess whirl flutter, the model should consider that propellers are working in high thrust conditions even at cruise speeds.

In general, there are two types of multirotor configurations: a default configuration with one propeller per tip and a counter-rotating configuration with two coaxial propellers per tip. This thesis aims to improve the understanding of the aeroelastic propeller-structure interaction in multirotor drones by modeling and predicting whirl mode flutter in thrusting conditions for a beam-propeller configuration, including counter-rotating propeller configuration. To accomplish this goal, a semi-analytical model, which can be applied in the preliminary stages of the VTOL design, is developed for a cantilever beam with a tip propeller, using a conventional propeller configuration or counter-rotating configuration. This research finalized with the stability analysis for whirl flutter of a five meters diameter octocopter.

1.1. Document outline

This thesis consists of eight chapters. The document introduction was already presented in . Afterward, a summary of the literature review of the whirl flutter phenomena and propeller aerodynamics is presented in , including the main research questions and objectives. Next, in , the propeller aerodynamics and whirl forces in thrusting conditions are derived for a conventional and a counter-rotating propeller configuration. In , the structural beam finite element model is presented. Subsequently, in the aeroelastic model is developed, the propeller-nacelle equations of motion are derived and coupled to the propeller aerodynamics and structural model. In , the whirl flutter analysis of the multirotor and results are presented. Finally, the main conclusions and findings of the thesis are shown in .

State of the art review

This chapter contains a summary of the research on whirl flutter phenomena, explaining the history of the development, mathematical description, importance, relevance of different parameters, and current state of the art. Then, different methods to determine the aerodynamics of propellers in thrust conditions are discussed, including counter-rotating propellers, with an emphasis on blade element momentum theory. Finally, the main research questions and objectives are presented.

2.1. Whirl Flutter

Whirl flutter is defined as a dynamic instability that can occur in flexibly mounted motor nacelle with propellers [1], which involves the coupling of the gyroscopic and aerodynamic forces of the propeller with the inertial, elastic and damping forces of the structure [10]. It was first introduced by Taylor and Brown in 1938 [7]. Then, in the 60s, the concept of whirl flutter was studied more exhaustively in aircraft by NASA [10], as this aeroelastic phenomenon gained importance due to two accidents of a Lockheed L-188 C Electra II [5].

In 1962 Houbolt and Reed [1, 11] proposed a simple mathematical model that describes the gyroscopic precession of a flexible propeller-nacelle system which can lead to whirl flutter instability in a relatively simple system, composed by a rigid propeller and a rigid power plant with two flexible degrees of freedom: pitch and yaw. Houbolt and Reed showed the influence of key parameters of whirl flutter and found that increasing the pitch and yaw stiffnesses increases the flutter speed. They also found that generally, structural damping has a stabilizing effect. In addition, they found that increasing the pivot location to propeller radius ratio (e/R), increases the stability boundary and decreases the damping sensibility.

Houbolt and Reed's model was compared with experimental results by Bland and Bennet [12]. They performed wind tunnel experiments with rigid propellers and flexible power plants, operating the propellers in windmilling conditions. Bland and Bennet [12] observed that theoretical whirl flutter speeds and frequencies were in agreement with experimental data, with the theoretical approach being more conservative (lower whirl flutter speeds) when theoretical aerodynamic stability forces were used. They also found that the theoretical stability forces had the same trend as the measured stability forces, but differed in magnitude in some cases.

In 1966, Reed presented a state of the art review of whirl flutter [13] for NASA. The reviewed mathematical model consists of a rigid propeller-nacelle structure with pitch and yaw degrees of freedom, similar to Houbolt and Reed [1], but also considered new degrees of freedom to represent flapping blades and flexible blades, based on the mathematical model proposed by Richardson [14]. Then, in 1977, Kvaternik and Kohn [15] presented an experimental parametric investigation of whirl flutter, a study motivated by the need for more data to assess the predictability of whirl flutter. This study considered a flexible power plant with pitch and yaw degrees of freedom and also considered flapping hinges and flexible blades. The results obtained by Kvaternik and Kohn [15] showed that the predicted whirl flutter frequencies and speed showed excellent agreement with the experiments and thus, whirl flutter could be predicted using linear stability analysis and two dimensional quasi-steady aerodynamics. It is important to mention that all the models and experiments previously mentioned consider the propellers

2. State of the art review

in windmilling conditions (no thrust generated), which can be applied in cases of forward flight, when the thrust of the propeller is low compared to the maximum thrust [13].

In 1989, the first numerical solver for whirl flutter was implemented by Rodden and Rose [16]. This preprocessor was developed to include the aerodynamic and gyroscopic forces of a propeller/nacelle system to MSC/NASTRAN, to assess whirl flutter analysis with the software. The implemented aerodynamic and gyroscopic forces were based on the model of Houbolt and Reed [1].

Later on, whirl flutter continued to develop. In 2005, Kunz [17] presented an analytical approach for whirl flutter stability analysis that unifies the models of propellers, prop-rotors, tiltrotors, and helicopter rotors. In 2015, an extensive review of the whirl flutter phenomena was done for turbo-propellers aircraft, including tiltrotor aircraft by Jiří [5], including the airworthiness regulations FAR/CS 23, FAR/CS 25. In 2020, Liu Xu [18] did an extensive parametric analysis using an analytical whirl flutter model of the X-57 Maxwell by NASA, which is a small experimental electric airplane with a large number of electric motors used to increase the overall lift produced by the wing [19].

2.1.1. Whirl flutter accidents

As mentioned before, the whirl flutter phenomenon gained importance due to the aircraft accidents that occurred in the 60s. Whirl flutter was the direct cause of the Lockheed L-188C Electra II fatal accidents in 1959 and 1960, which killed everyone on board [5]. It was found that the engine mounts were not able to damp the whirl mode vibrations of the aircraft because of a reduction of the overall stiffness and thus, after the accidents, they were reinforced and redesigned to withstand higher stresses [5].

The Beechcraft 1900C also suffered from an accident produced by whirl flutter in 1991 [20]. The accident occurred due to a damaged engine bed, caused by fatigue cracks and defects on the engine mount isolators, decreasing the whirl flutter speed envelops of the aircraft [5].

Also, the amphibious aircraft Grumman Turbo Mallard GF73T crashed because of whirl flutter in 2005, due to fatigue cracks damage [5].

The latest two mentioned accidents occurred during a time when whirl flutter was already studied and implemented in the design, but without considering parameters such as damage. Thus, it is important to address whirl flutter in new configurations (such as the multirotor that inspired this research) and to have a reliable model that can ensure the airworthiness of these configurations.

2.1.2. Whirl flutter model

The most elemental model to analyze whirl flutter consists of an idealized rigid power plant that is contained by an elastic spring-damper system in θ (pitch) and ψ (yaw) degrees of freedom, located behind a rigid propeller [13], as shown in Figure 2.1.

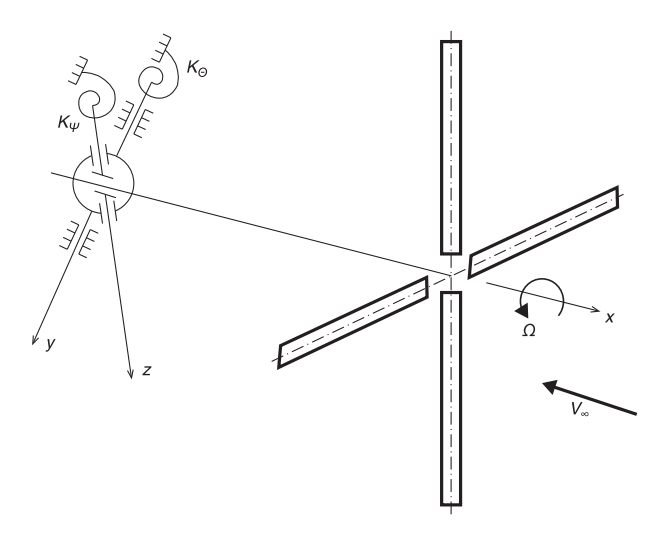


Figure 2.1: Idealized gyroscopic model [21].

With this simple model, ignoring aerodynamic forces and propeller rotation, two whirl modes can be distinguished: backward and forward [1]. The forward mode consists of the propeller precessing in the same direction of the propeller rotation and in the backward mode, on the contrary, the propeller

2.1. Whirl Flutter 5

precesses in the opposite direction to the blade rotation [13]. Comparing both modes, the backward mode has a lower frequency than the forward mode, they have a phase shift of 90° and with increasing propeller angular velocity, the frequency difference between the modes also increases [5]. The modes are shown in Figure 2.2.

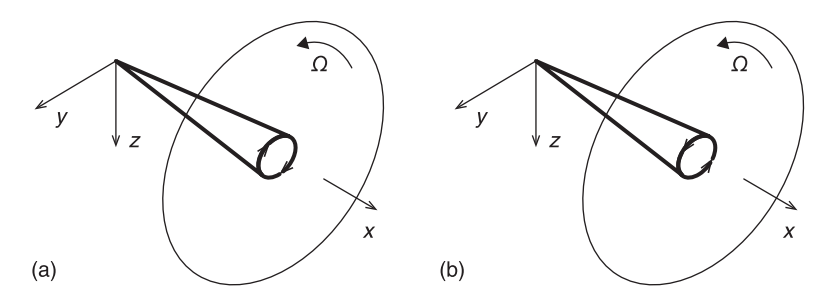


Figure 2.2: Backward mode (a) and forward mode (b) [21].

Conventional aircraft propellers (turbo-propellers) are generally considered rigid due to their high natural frequencies, hence only the backward mode is present [13]. On the other hand, for helicopter rotors and some tiltrotors, propellers are considered flexible [17] or to have flapping hinges, and therefore, the backward and forward modes can be observed [13].

The gyroscopic motion of the propeller produced by these shape modes are responsible for the whirl flutter instability, as they change the blade's angle of attack and thus, non-stationary aerodynamic forces are generated, which could potentially induce the flutter instability [5]. As in classical flutter, whirl flutter has a correspondent speed or flight condition in which flutter is reached. For lower speeds than the flutter speed, the gyroscopic oscillations are stable. For higher speeds than the flutter speed, the system is unstable, as shown in Figure 2.3.

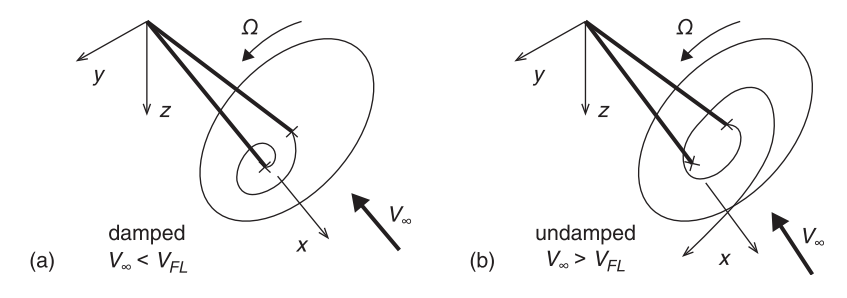


Figure 2.3: Stable (a) and unstable gyroscopic oscillation (b) [21].

Different methods have been developed through the years to study whirl flutter. These methods can be classified into two different categories: analytical and numerical methods.

Analytical methods have been developed first with rigid models for blades and wing, such as Houbolt and Reed [1] and later has been expanded to model flapping hinges and flexible blades, but still considering a rigid wing, such as the work of Kvaternik and Kohn [15] and Kunz [17]. The latter one has the advantage of presenting a unified model for studying whirl flutter for propeller-driven aircraft, tiltrotors and helicopters. A more advanced and recent model which includes wing flexibility is the MSc thesis presented by Liu Xu [18]. The methods mentioned previously use windmilling conditions for the propeller calculations, which means that there is no thrust generated by the propellers. For the aircraft configuration evaluated in these studies, thrust can be neglected, because the difference between windmilling and thrusting whirl aerodynamic forces in high speed flight condition is less than 5% [13]. This does not hold for low speeds flight conditions [13].

Numerical methods have been also developed to study whirl flutter. For the development of the X-57 Maxwell by NASA, two different numerical models were used to assess whirl flutter, CAMRAD II and Dymore [22]. CAMRAD II is an aeromechanical analysis of helicopters and rotorcraft that includes multibody dynamics, nonlinear finite elements, structural dynamics, and rotorcraft aerodynamics [23]. Dymore is a finite element based multibody dynamics code for the comprehensive modeling of flexible multibody systems [24]. The main differences between CAMRAD II and Dymore are the aerodynamics calculation and aeroelastic damping calculation for flutter analysis. Both softwares use lifting line theory

6 2. State of the art review

coupled with linear inflow model, but in the case of Dymore, the propeller aerodynamics can be also calculated externally and then coupled to the software[22]. In CAMRAD II, the damping is obtained directly through eigenvalue and eigenmode analysis [22], on the other hand, Dymore uses the Prony method to identify the damping based on the transient response [22].

There is also an additional package to MSC/NASTRAN for rigid propellers that uses the analytical model of Houbolt and Reed [1], developed by Rodden and Rose [16]. A deeper investigation of high fidelity numerical methods will not be included in this research as it is not considered as part of the thesis objective.

2.1.3. Whirl flutter aerodynamics

To account for whirl flutter and stability boundaries, it is necessary to consider the gyroscopic motion of the propeller and characterize the aerodynamics forces that appear due to the pitching and yawing motion. Without considering the aerodynamics, there is no divergent whirl instability, as the net energy input in the system due to gyroscopic motion is zero [1].

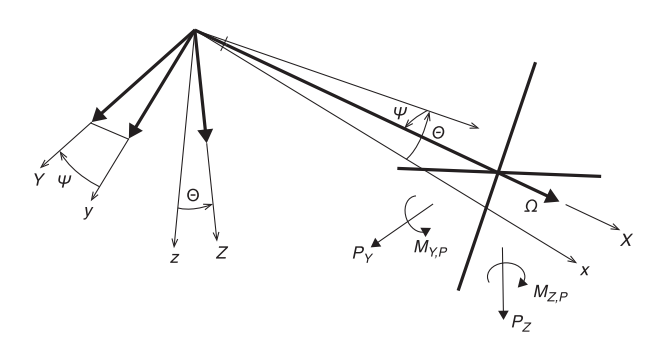


Figure 2.4: Whirl forces respect to gyroscopic system degrees of freedom (adapted from [5]).

As mentioned before, the pitching and yawing motion produce aerodynamic forces,which can be conveniently decomposed in terms of Py, My, Pz, and Mz as shown in Figure 2.4, to be later coupled to the system degrees of freedom θ (pitch) and ψ (yaw). As the pitching and yawing motion are symmetric, Py, My, Pz, and Mz can be explained from the pitching deflection, yawing velocity, and pitching angular velocity, which are analogous to the yawing deflection, pitching velocity, and yawing angular velocity.

The pitching deflection produces a induces a higher angle of attack in the left half of the propeller disk and a lower angle of attack in the right half of the propeller disk , and thus, higher thrust is produced in one half of the propeller disk with respect to the other, producing a moment Mz, as shown in Figure 2.5. Also, the pitching deflection induces a vertical component change on the thrust, from which the force Pz arises, shown as ΔH in Figure 2.5.

2.1. Whirl Flutter 7

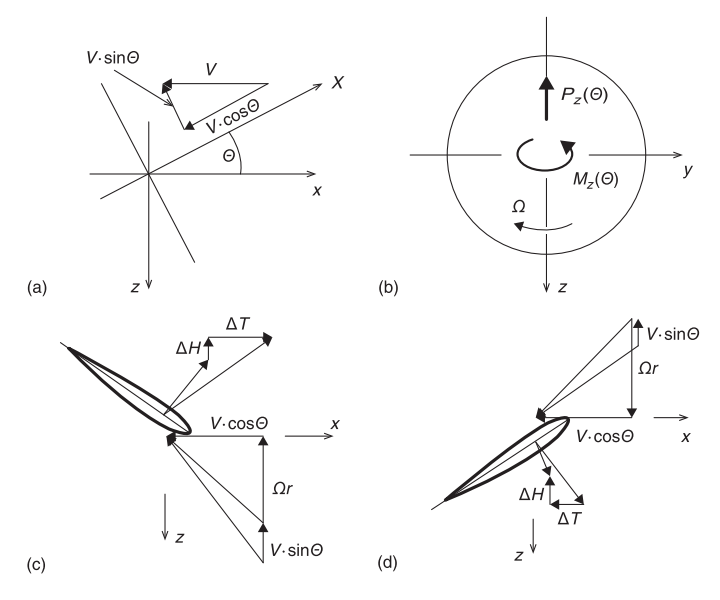


Figure 2.5: Aerodynamics forces arising from pitching deflection, (c) retreating blade at the left side of the propeller propeller disk and (d) advancing blade blade at the right side of the propeller propeller disk [5].

The yawing velocity increases the inflow velocity perceived by the blades of the right half of the propeller disk and decreases the inflow velocity perceived by the left half of the propeller disk, having a similar effect on the blade angle of attack as the pitching deflection, generating the force Pz and moment Mz, as shown in Figure 2.6.

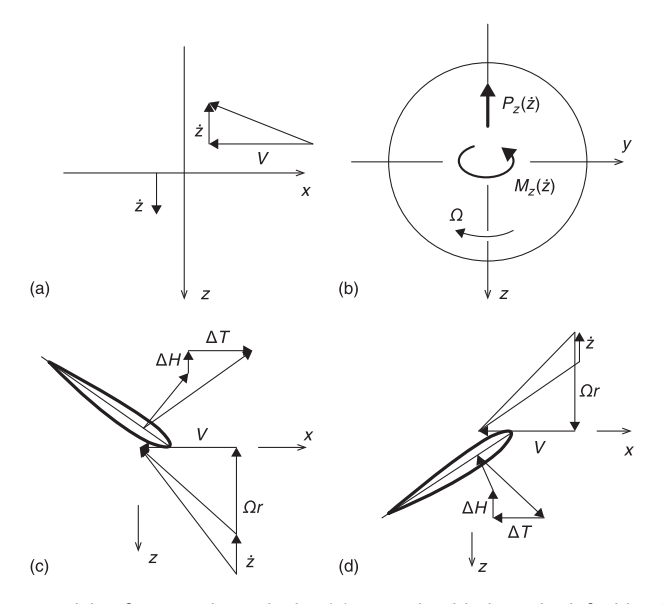


Figure 2.6: Aerodynamics forces arising from yawing velocity, (c) retreating blade at the left side of the propeller propeller disk and (d) advancing blade blade at the right side of the propeller propeller disk [5].

The pitching angular velocity increases the blades' perceived inflow velocity of the bottom half of the propeller disk and decreases the blades' perceived inflow velocity of the top half of the propeller disk. As a consequence, a moment, My, and a force, Py, arise, as shown in Figure 2.7.

8 2. State of the art review

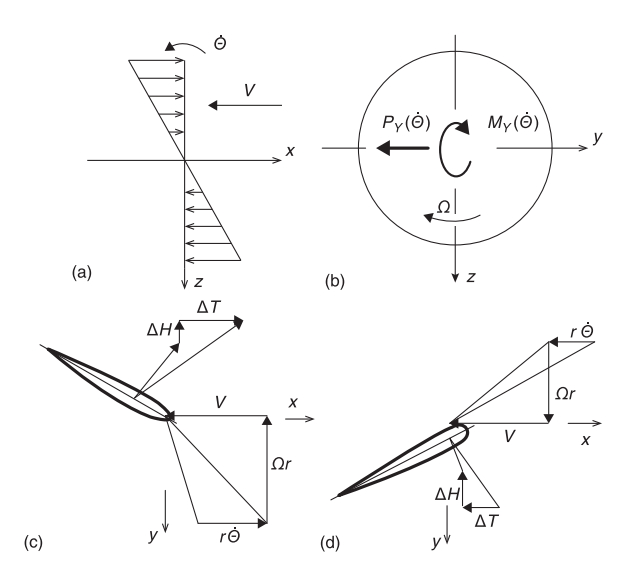


Figure 2.7: Aerodynamics forces arising from pitching angular velocity, (c) retreating blade at the top side propeller propeller disk and (d) advancing blade blade at the bottom side of the propeller propeller disk [5].

The first analytical model that describes the aerodynamic forces caused by the gyroscopic motion of the propeller (Py, Pz, My, Mz) was published by Ribner [25] and then Houbolt [1]. These models permitted the analytical assessment and prediction of whirl flutter [12, 13, 15].

Both models rely on similar assumptions and lead to comparable results [13]. The models use strip theory and assume quasi-steady aerodynamics and a small inflow angle[13]. The main difference between Houbolt's and Ribner's model is that Ribner's work lacks the simplicity of Houbolt's theory [13] as Ribner's model includes drag, uses trigonometric functions, and uses an inflow factor. As both lead to similar results, Houbolt's method has been generally preferred.

2.1.4. Influence of major parameters in whirl flutter

The most important structural and flight condition parameters that affect whirl flutter considering rigid blades and a rigid power plant restrained by elastic pitch and yaw degrees of freedom are: the stiffness of the power plant spring attachments (K_{θ}, K_{ψ}) , the stiffness ratio (K_{θ}/K_{ψ}) , the propeller advance ratio J [5], the structural damping and the propeller angular velocity (Ω) . These parameters have been analized by Bland and Reed [11], Houbolt and Reed [1], Sewall [26], Kvaternik and Kohn [15] and Cerdle [5].

The effect of the stiffness of the power plant is shown in Figure 2.8. It can be inferred that increasing the overall stiffness increases the whirl flutter velocity [5].

The effect of the stiffness ratio is shown in Figure 2.8. The most critical stiffness ratio is found for $K_{\theta}/K_{\psi}=1$ [1, 5], which means that for a constant advance ratio, K_{θ} and K_{ψ} required for the system to be stable are maximized. It is also important to notice the divergence of the system is driven by the minimum stiffness of both stiffnesses (K_{θ}, K_{ψ}) [1].

Figure 2.8 also shows that increasing the propeller advance ratio, J, increases the necessary stiffness for the system to be stable and therefore, this factor tends to destabilize the system [5].

The structural damping affects the instability boundary by having a stabilizing effect, as shown in Figure 2.9. Thus, it can lead to considerable underestimation of the whirl flutter speed, if it is not considered properly [5]. In Figure 2.9, it can also be seen that the further the pivot is located (ratio a/R), the less effect the damping has on the stability boundary. This behavior can be explained because increasing the pivot distance increases the aerodynamic damping, which has a stabilizing effect on the system [5]. It is also important to mention that increasing the structural damping decreases the required stiffness for system stability [1].

For high propeller angular velocity, Ω , and considering constant structural stiffness, the instability boundary is not significantly affected by Ω [5], as shown in Figure 2.10. This does not hold for low propeller angular velocity, because at this point, the instability boundary is primarily limited by static divergence [5].

2.1. Whirl Flutter 9

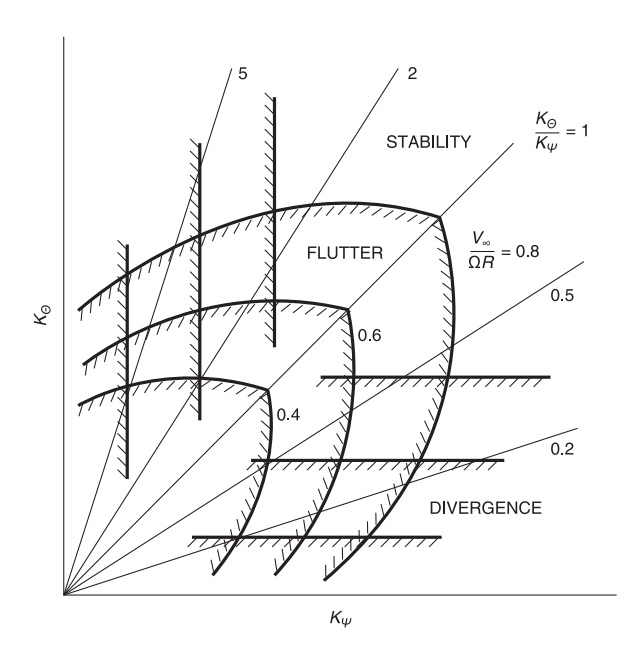


Figure 2.8: Whirl flutter boundary and divergence for different advance ratios [21].

2.1.5. Thrust effect

As indicated previously, windmilling conditions were used for the analytical evaluation of whirl flutter. Reed [13] mentioned that thrust has an insignificant effect on whirl flutter stability for conventional rigid propellers under high-speed flight conditions. For fixed wing aircraft, whirl flutter is expected to occur at high forward speeds and thus, thrust can be neglected in the analysis. This conclusion was also supported by the analytical work of Ravera [27] and Kvaternik [28], who stated that thrust has a negligible effect on the aerodynamic forces responsible for whirl flutter. It is important to outline that the previous statements are further supported with experimental results by Bennet and Reed [29].

There is an important difference between fixed wing and multirotor aircraft. Fixed wing aircraft encounter whirl flutter at high forward speed and, in this flight condition, the propellers are lightly loaded. On the other hand, for multirotor aircraft, all the lifting force is produced by the propellers and therefore, it is necessary to evaluate low-speed, high thrust conditions, such as hovering and forward flight, where thrust can cause larger changes in the whirl flutter aerodynamic forces [27]. Additionally, in hovering and forward flight, thrust changes the propeller trim conditions, affecting the stability boundaries [30].

In general, thrust has a stabilizing effect, when it is considered for a system with hinged blades and rigid pylon (without considering non-linearities) because it increases the damping of the system, as mentioned by Kvaternik [28]. When non-linearities are introduced, such as control stiffness non-linearity and free-play, thrust needs to be considered, as mentioned by Masarati [31] and Krüger [32].

2.1.6. Tiltrotor whirl flutter

Tiltrotor aircraft can change the inflow angle and loading condition of the propellers depending on the flight conditions, and thus, whirl flutter analysis should include the helicopter flight regime (inflow angle of 90°), transition flight regime, and forward flight regime [5]. Even though whirl flutter is expected in forward flight because of the high airspeed, it is necessary to evaluate the other regimes to be certain that there is no dynamic instability.

Studies of whirl flutter in tiltrotor aircraft have been developed since the 60s. Edenborough [33] developed an analytical model for forward flight and experimental full-scale model validation, confirming the possibility of stable configurations for VTOL tiltrotor aircraft. It is important to note that windmilling conditions were used for this study.

As tiltrotors provide thrust and lift in the helicopter and transition regime, with large propeller blades, it is necessary to account for the flexibility of the blades or flapping hinge blades, which introduce two extra vibration modes, blade flapping and lead-lag motion [18, 34].

Kvaternik [15, 28] did an extensive study in tiltrotor aircraft aeroelasticity including an analytical and experimental study (using flapping blades). Kvaternik demonstrated that due to the flapping hinges,

10 2. State of the art review

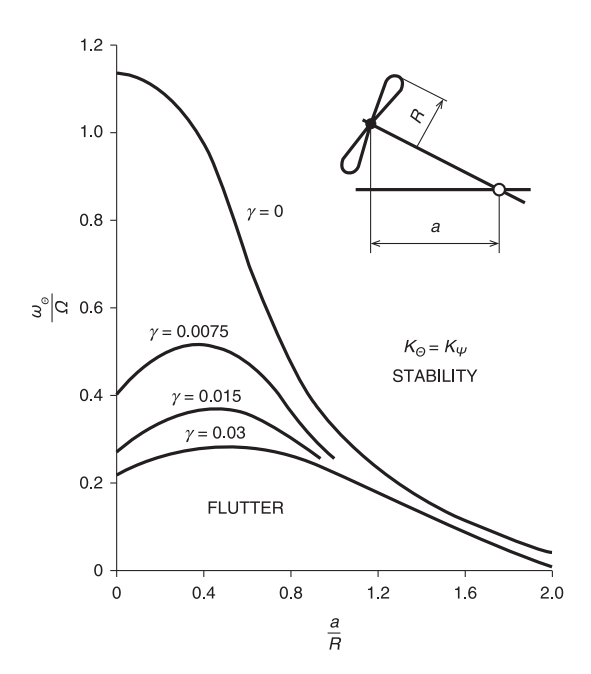


Figure 2.9: Influences of structural damping and propeller – pivot point distance on whirl flutter (γ is the system structural damping) [21].

tiltrotor aircraft can suffer from backward and forward whirl flutter.

As mentioned before, thrust has a stabilizing effect for whirl flutter boundary, with the assumption of rigid propellers [5]. The assumption of rigid propellers is sufficient for standard propellers, as the eigenfrequencies of conventional propellers are much higher than the engine/mount-structure vibration modes [5]. This characteristic makes the assumption suitable to be applied in the modeling of small aircraft, commuters, etc. On the other hand, as an example, in the case of large military transport aircraft, tiltrotors, and helicopters, flexible propellers need to be considered to assess whirl flutter.

In conclusion, tiltrotor whirl flutter is a highly complex phenomenon, which considers flexible proprotors and therefore, includes new degrees of freedom to account for the propeller blade flexibility and movement, which also leads to different modes and mechanisms of whirl flutter. Complicated equations model the tiltrotor dynamics, and they include the rotor swash plate motions. In tiltrotors, whirl flutter is one of the limiting factors [35] and thus, an extensive study of whirl flutter is necessary. Aerodynamics models using CFD are used to study tiltrotor flutter, and these models consider time-dependent aerodynamics forces. Generally, complex numerical methods have been intensively used to determine the whirl flutter boundaries [5]. Acree, Peyran, and Johnson [36] used the stability conditions for whirl flutter to optimize certain parameters of the rotor and the aircraft itself. It is important to mention that in tiltrotors, there is a strong interaction between the wing and the propeller, because the latter is placed in the wing tip.

In this thesis, for the analysis of multirotor aircraft, propellers are considered rigid, and therefore, there is no purpose of further investigation of tiltrotor whirl flutter, which considers flexible and flapping blades. In addition, the wing-propeller aerodynamics interactions of the evaluated multirotor is not important, as the multirotor body aerodynamic effect is assumed negligible, and there are no wings. Thus, the only aerodynamic effects considered are produced by the propellers.

2.2. Propeller aerodynamics

An important aspect that influences the study of whirl flutter is aerodynamics. As explained earlier, the multirotor propellers operate in high thrust conditions. For this reason, it is necessary to study a model that can predict the aerodynamic forces and moments that the propellers produce in this state. Two types of models can be distinguished for blade aerodynamics: high and low fidelity models [37].

High-fidelity models are based on computational fluid dynamics (CFD), which is available commercially in software such as ANSYS CFX, Fluent and OpenFoam. This type of model is computationally expensive [37], which makes high fidelity models not suitable for the preliminary design stages [38].

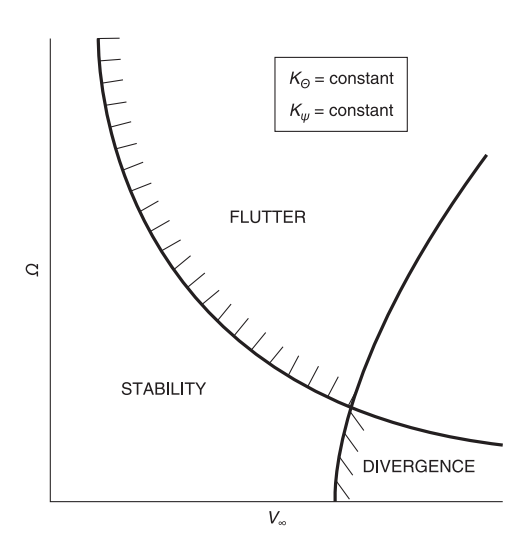


Figure 2.10: Whirl flutter boundary (stiffness remains constant) [21].

Low-fidelity models for thrusting conditions are based on blade element momentum theory (BEMT). This algorithm is fast and it can be used for the design and optimization of blades, as shown by Kummel [39]. The combination of low-computational cost, good accuracy, and the use of strip theory which can be coupled with Houbolt's model, makes low-fidelity models good candidates to be used for whirl flutter assessment in the design process.

2.2.1. Blade element momentum theory

BEMT consists of a combination of blade element theory and momentum theory [40].

Blade element theory was introduced by Froude [41] and it divides the propeller blade into sections, referred to as elements. The element theory assumes that the elements can be represented by the 2-D airfoil geometry and the respective local flow conditions, from which the blade element forces can be obtained. Then, by summing the different elements forces, the total forces can be obtained [42].

Momentum theory was first presented by Rankine [43] based on a disk actuator. Later, Froude [44] developed the correct dynamic interpretation, in which half of the acceleration takes part before the propeller and the other half after the propeller disk, using Bernoulli equations for the energy and momentum balance [45]. The momentum theory was further developed by Lanchester [46], Betz [47] and Joukowsky [48].

The combination of both theories into BEMT was introduced by Glauert [49] in 1926. BEMT considers steady aerodynamics with an inviscid, irrotational, and incompressible flow with uniform velocity and static pressure over every cross-section of the propeller disk and stream-tube [50, 51]. Since the annular elements shown in Figure 2.11 are independent of each other, there is no radial flow [52].

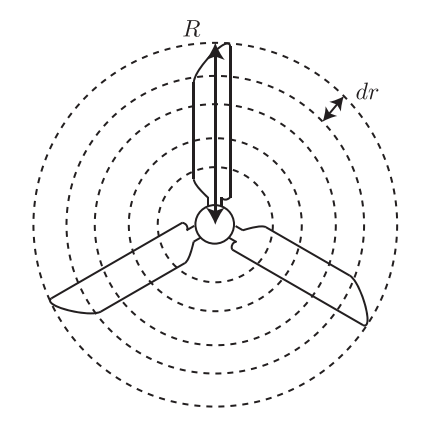


Figure 2.11: Discretization of rotor disk [53].

As explained earlier in this section, the element theory divides the propeller disk into independent

12 2. State of the art review

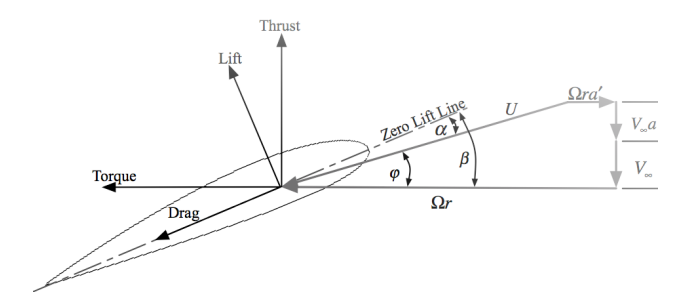


Figure 2.12: Blade element diagram [50].

differential annular elements, shown in Figure 2.11, and the aerodynamic forces of these elements can be calculated by the 2-D airfoil characteristics and local flow conditions, shown in Figure 2.12. Then, using momentum theory, the induced velocities in the different elements of the propeller can be calculated (axial and tangential). These induced velocities also affect the forces calculated by the element theory and thus, an iterative process that relates the element and momentum theory is needed to obtain the element forces [54]. After obtaining converged results, the different element forces can be added together to get the overall forces, the propeller thrust, and propeller torque.

Two different types of momentum equilibrium are considered through the propeller stream-tube: axial momentum and angular momentum (sometimes called tangential momentum) [50, 51]. The former is responsible for the thrust component of the force, the latter for the torque component of the force.

BEMT assumes an infinite number of blades in the propeller disk. In the case of finite blades, Prandtl showed that the circulation over the blade tends to zero on the tip [55], and thus, the lift produced by the tip tends to zero. Prandtl [56] developed a correction factor to include the tip losses and later, models based on the Prandtl factor were developed to provide more realistic loads in the blades tip of wind turbines [55, 57]. Examples of these models are Wilson and Lissaman [58] and de Vries [59].

Hub losses can also be included in a similar fashion as tip losses, using the Prandlt correction factor [50, 54].

Implementation of the improved BEMT algorithm shows good results compared to experimental results, as shown by Gud and Rosen [60] and Loureiro, et al. [37]. Additionally, use of the BEMT algorithm also shows good agreement with CFD results, even when considering flexible propeller blades [38]. Even though it is not a very complex method, BEMT is still widely used in the design of propellers and wind turbines, as the computational cost of this method is low and the aeroelastic implementation straightforward.

2.2.2. Counter rotating propellers BEMT

In general, the aerodynamics of counter-rotating propellers are more complicated to analyze than single rotor propellers. The wake of the upstream propeller significantly influences the performance of the propeller located downstream, and in some cases, unsteady aerodynamic effects arise. In the case of coaxial wind turbines, CFD simulations or Navier-Stokes numerical solvers, such as RANS, are usually used to analyze the system efficiency and forces [61–64].

For parametric and preliminary studies, counter-rotating propellers have been modeled using BEMT [64]. As shown by Siddappaji and Turner [65], some modifications can be included on the conventional BEMT to account for the downstream propeller.

The main assumptions and modifications of Siddappaji and Turner's model [65] are: the rear propeller is located at the fully developed wake of the front propeller and therefore, the axial and tangential induced velocities generated by the front propeller are considered as part of the inflow velocity of the rear propeller; the rear propeller does not affect the front propeller flow conditions; the rear propeller axial and tangential induction factors are introduced; and four new equations arise from the momentum and element theory of the rear propeller.

In the rear propeller, BEMT considers that the flow stream tube is fully developed [66, 67], which, in the case of wind turbines, can lead to underprediction of inflow velocity of the rear rotor [67], and overprediction in the case of thrusting propellers. It also considers that the wake of the front rotor only affects the rear rotor and the wake of the rear rotor does not affect the flow of the front rotor [66].

A more complex model is presented by Thiele, Obster and Hornung [68], which includes azimuthal

inflow and induced velocity components, specifically to model VTOL UAVs counter-rotating propellers. This model is in good accordance with measured data [68].

2.3. Research Questions and Objectives

This thesis aims to study the whirl flutter phenomenon and to expand the existing mathematical models into a new model that could be applied to flight vehicles without wings or the complex rotor system of helicopters. With the electric propulsion advancements, eVTOLs and "flying taxi" designs and prototypes are arising. To achieve safe and successful designs, thrusting conditions in the propellers need to be considered in the aeroelastic model, whereas the existing analytical models use windmilling conditions due to the nature of whirl flutter in airplanes.

The main goal of the thesis can be summarized by the following:

"To improve the understanding of the aeroelastic propeller-structure interaction in multirotor drones by modeling and predicting whirl mode flutter in thrusting conditions for a beam-propeller configuration, including counter-rotating propeller configurations, applied to a human size octocopter".

The main research question that needs to be solved with this thesis is:

"Which is the whirl flutter boundary for a multirotor configuration considering thrusting conditions?"

This question leads to different sub-questions, which are necessary to address the whole topic, as well as to support to support the main question:

- 1. How to describe the propeller aerodynamics for thrusting conditions?
 - Which is the most appropriate model to capture thrusting conditions in propellers?
 - How to capture the unsteady behavior of the gyroscopic motion due to whirl?
 - Which is the most appropriate model to capture thrusting conditions in counter-rotating propellers?
- 2. Which is the simplest model that can be considered to assess the whirl flutter boundary of the multirotor structure?
 - · Which aerodynamic and structural degrees of freedom need to be considered?
 - Is it possible to couple current propeller models that consider thrusting conditions with the structural model used to assess whirl flutter? How this can be done?
 - How does the counter-rotating propeller configuration influence the whirl flutter boundary?
- 3. Do any flight conditions exist that can lead to whirl flutter for the different configurations of the human size octocopter? If yes, which are these conditions and can they be reached during flight, considering the drone specifications given by Betronka SPA?

Propeller aerodynamics

In chapter 2, the literature review and objective of the thesis were presented. To achieve this objective, a mixed analytical-numerical model for the propeller aerodynamics in thrusting conditions is presented in this chapter. The model assesses two different configurations: one propeller and counter-rotating propellers.

First, the aerodynamics of a propeller considering thrust conditions are modeled and afterwards, coupled to a quasi-steady perturbation aerodynamic model that considers the effects of the gyroscopic movement of a propeller-pylon structure, to obtain the unsteady aerodynamic forces produced by the whirl motion, responsible for the whirl flutter instability.

3.1. Blade element momentum theory (BEMT)

To model the propeller aerodynamics in thrusting conditions, the BEMT model presented by Rwigema [50] is used and implemented in MATLAB. The main assumptions of BEMT are steady aerodynamics with an inviscid, irrotational, incompressible flow with uniform velocity and static pressure over every cross-section of the propeller disk and stream-tube. Additionally, the annular elements are independent from each other and the forces produced by the elements depend only in the 2-D blade geometry and local flow characteristics [50].

As explained in section 2.2, BEMT is comprised of two parts: the momentum theory and the element theory. The momentum theory considers axial and tangential momentum balance for every annular element of the propeller disk, while element theory considers the 2-D geometry of the element to calculate the thrust and torque produced by every element. This provides enough equations to calculate both induction factors and the thrust and torque of every element of the propeller.

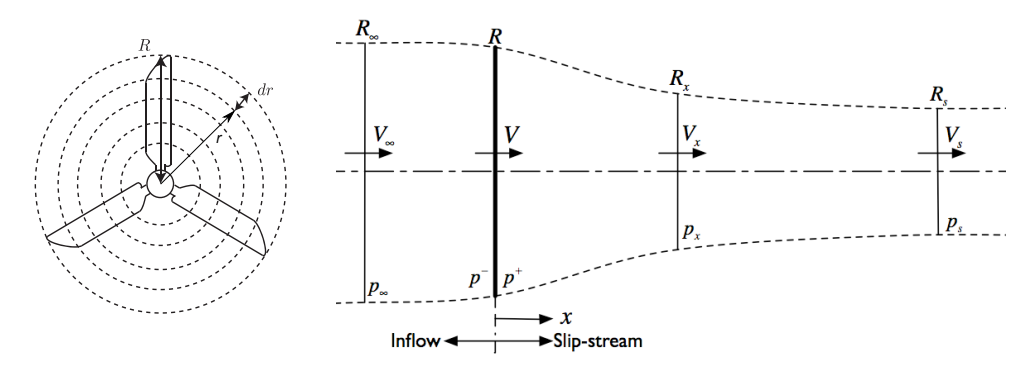


Figure 3.1: Right: Blade annular elements [53]. Left: propeller stream tube [50].

3.1.1. Momentum theory

First, the momentum conservation of an annular element of the propeller is derived. The mass conservation of the flow that passes through an annular element shown in Figure 3.1 can be expressed

as:

$$d\dot{m}_{\infty} = d\dot{m} = d\dot{m}_{\rm s} \tag{3.1}$$

Where $d\dot{m}_{\infty}$ represents the free stream mass flow, $d\dot{m}$ represents the mass flow at the propeller disk, and $d\dot{m}_{s}$ is the mass flow of the fully developed flow stream after the propeller.

The mass flow can also be written as:

$$d\dot{m} = \rho V dA \tag{3.2}$$

Where ρ is the flow density, V is the flow velocity at the propeller disk, and dA is the propeller annular element area. Using Equation 3.2 the mass conservation can be written as:

$$V_{\infty} dA_{\infty} = V dA = V_{\rm s} dA_{\rm s} \tag{3.3}$$

Where V_{∞} and dA_{∞} are the velocity and annular element area of the free stream flow, V and dA are the velocity and annular element area at the propeller plane, and V_{s} and dA_{s} are velocity and annular element area of the fully developed flow stream after the propeller, respectively.

Considering the axial momentum conservation, the thrust produced by an annular element is:

$$dT = d\dot{m} (V_S - V_\infty) = \rho V (V_S - V_\infty) dA$$
(3.4)

In addition, the propeller produces a discontinuous rise in pressure from p^- to p^+ , with a constant velocity V, which is the velocity at the propeller plane. Therefore, the thrust can be written as:

$$dT = (p^+ - p^-) dA (3.5)$$

As the flow is inviscid, the free stream pressure, p_{∞} , is equal to the pressure of the fully developed flow stream after the propeller, p_s . Therefore, applying Bernoulli's equation upstream and downstream the propeller plane:

$$p^{+} + \frac{1}{2}\rho V^{2} = p_{s} + \frac{1}{2}\rho V_{s}^{2}$$
 (3.6)

$$p^{-} + \frac{1}{2} \rho V^{2} = p_{\infty} + \frac{1}{2} \rho V_{\infty}^{2}$$
 (3.7)

$$p_{\infty} = p_{\rm s} \tag{3.8}$$

Subtracting Equation 3.7 on Equation 3.6, and then replacing on Equation 3.8:

$$p^{+} - p^{-} = \frac{1}{2} \rho \left(V_{s}^{2} - V_{\infty}^{2} \right) \tag{3.9}$$

Combining Equation 3.5, Equation 3.9 and Equation 3.4, the velocity at the propeller rotor can be obtained:

$$V = \frac{V_{\infty} + V_s}{2} \tag{3.10}$$

Furthermore, defining the axial induction factor a, which can be interpreted as a measure of the propeller effect on the flow axial velocity, V and V_s can be rewritten as:

$$V = V_{\infty} (1 + a)$$

 $V_{\rm S} = V_{\infty} (1 + 2a)$ (3.11)

Additionally, the area of an annular element is:

$$dA = 2\pi r \, dr \tag{3.12}$$

Then, the thrust produced by an annular element can be written as:

$$dT = 4\pi r \rho V_{\infty}^{2} (1+a) a dr$$
 (3.13)

In a similar fashion, a tangential induction factor, a' (sometimes called angular induction factor), is defined. As the upstream flow only has an axial velocity component, ω_{∞} is zero, and therefore, analogous to Equation 3.11 :

$$\omega_{\infty} = 0$$

$$\omega_{S} = a' \Omega$$

$$\omega_{S} = 2a' \Omega$$
(3.14)

Where Ω is the propeller angular speed.

In addition, the angular momentum conservation is:

$$Q = \frac{dL}{dt} = \frac{dI\,\omega}{dt} = \dot{m}\,\omega\,r^2 \tag{3.15}$$

Using Equation 3.14 and Equation 3.15, the torque produced by an annular element can be calculated as:

$$dQ = d\dot{m} \, 2a' \, \Omega \, r^2 dQ = 4\pi \, r^3 \, \rho \, V_{\infty} \, \Omega \, (1+a) \, a' \, dr$$
 (3.16)

3.1.2. Blade element theory

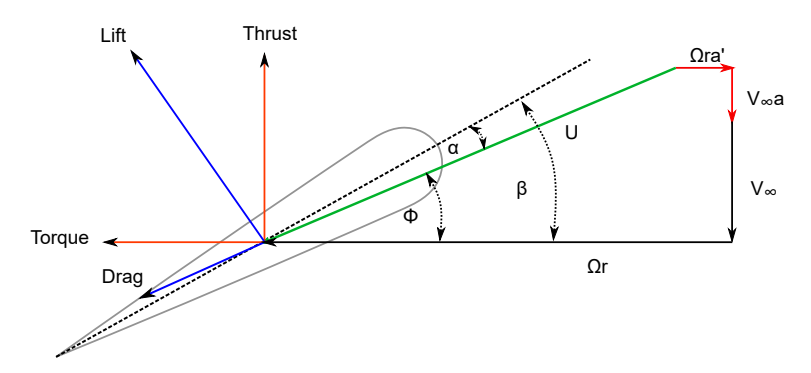


Figure 3.2: Blade element diagram.

Momentum theory provides two equations with four different unknown variables: dT, dQ, a and a'. Thus, two new equations are needed to solve the system of equations. These new equations are provided by the blade element theory, in which the forces produced by the annular elements are calculated using the 2-D airfoil geometry and local flow conditions of the element, shown in Figure 3.2.

To obtain the forces produced by an element, the local velocity U and the local angle of attack α need to be determined. U and α depend on the local inflow angle ϕ , which can be obtained from Figure 3.2 and expressed as:

$$\tan \phi = \frac{V_{\infty} (1+a)}{\Omega r (1-a')} \tag{3.17}$$

In addition, the local total velocity U and local angle of attack α can be obtained using the following relations:

$$U = \frac{V_{\infty} (1+a)}{\sin \phi}$$

$$\alpha = \beta - \phi$$
(3.18)

Where β is the geometric twist angle of the annular element. From the the 2-D airfoil geometry, the lift C_L and drag C_D coefficients can be obtained as a function of α . Then, the thrust and torque can be calculated:

$$dT = \frac{1}{2} B \rho U^{2} (C_{L}(\alpha) \cos \phi - C_{D}(\alpha) \sin \phi c) dr$$

$$dQ = \frac{1}{2} B \rho U^{2} (C_{L}(\alpha) \sin \phi + C_{D}(\alpha) \cos \phi c r) dr$$
(3.19)

Where B is the number of blades, c is the element chord length, and dr is the element width.

3.1.3. Correction factors

As mentioned in section 2.2, considering a finite number of blades in a propeller, the circulation at the blades' tips tends to zero. To account for the tip losses, Prandlt developed a correction factor [56] which can be implemented on the BEMT model as in the case of Rwigema [50]. The tip loss correction factor is:

$$F_{tip} = \frac{2}{\pi} \cos^{-1}(e^{-f_{tip}})$$

$$f_{tip} = \frac{B}{2} \frac{R_{tip} - r}{r \sin \phi}$$
(3.20)

Where R_{tip} is the propeller tip radius and B is number of blades. In a similar fashion, Rwigema [50] implemented the hub loss correction factor:

$$F_{hub} = \frac{2}{\pi} \cos^{-1}(e^{-f_{hub}})$$

$$f_{hub} = \frac{B}{2} \frac{r - R_{hub}}{r \sin \phi}$$
(3.21)

Where R_{hub} is the hub radius. The total correction factor is obtained by multiplying the tip and loss correction factor:

$$F = F_{tip} F_{hub} (3.22)$$

Then, the tip and hub losses can be included in the momentum balance by including the total correction factor in Equation 3.13 and Equation 3.16:

$$dT = 4\pi F r \rho V_{\infty}^{2} (1+a) a dr dQ = 4\pi F r^{3} \rho V_{\infty} (1+a) \Omega a' dr$$
(3.23)

3.1.4. Extrapolation of lift and drag coefficients for an airfoil

In general, the lift coefficient, \mathcal{C}_L , and drag coefficient, \mathcal{C}_D , are not available for the whole range of angles of attack (-180° to 180°). For angles above or lower than the ones provided by the airfoil \mathcal{C}_L and \mathcal{C}_D diagrams, the flat plate theory assumption in post-stall lift and drag is used [69]:

$$C_L = 2\sin\alpha\cos\alpha$$

$$C_D = 2\sin^2\alpha$$
(3.24)

This will permit the evaluation of the thrust and torque forces generated by the propeller in the whole range of angles of attack, which is a function of the induction factors, flow conditions, and blade geometry, guaranteeing the convergence of the BEMT code.

3.1.5. Final equations

Finally, the system of equations for every element is presented:

$$dT = \frac{1}{2} B \rho U^{2} (C_{L}(\alpha) \cos \phi - C_{D}(\alpha) \sin \phi) c dr$$

$$dQ = \frac{1}{2} B \rho U^{2} (C_{L}(\alpha) \sin \phi + C_{D}(\alpha) \cos \phi) c r dr$$

$$dT = 4\pi F r \rho V_{\infty}^{2} (1 + \alpha) a dr$$

$$dQ = 4\pi F r^{3} \rho V_{\infty} (1 + \alpha) \Omega a' dr$$

$$(3.25)$$

This system of equations can be solved numerically to obtain a and a', and then dT and dQ. Due to the non-linear behavior of these equations, brute-force method was used. It consisted of minimizing a residue R, composed by the absolute value of the differences of dT from element theory and momentum theory and dQ from the element and momentum theory, as a function of a and a':

$$R(a, a') = |dT^{el} - dT^{mom}| + |dQ^{el} - dQ^{mom}|$$

$$[a, a'] = min\{R(a, a')\}$$
(3.26)

With dT^{el} , dT^{mom} the thrust of an annular element obtained through element and momentum theory respectively, and dQ^{el} , dQ^{mom} the torque of an annular element obtained through element and momentum theory respectively.

After dT and dQ is obtained for every annular element i of the propeller , the overall thrust and torque of a propeller with n elements is:

$$T = \sum_{i=1}^{n} dT(i)$$

$$Q = \sum_{i=1}^{n} dQ(i)$$
(3.27)

3.1.6. Validation of BEMT

In order to validate the BEMT code implemented in MATLAB, NASA Technical Report 594 [70] was used, which consists of a extensive experimental wind tunnel study of six full-scale propellers in the normal and high-speed flight range [70]. The main experimental results show by NASA report [70] are the thrust coefficient C_T , the power coefficient C_P and the efficiency η against the propeller advance ratio J, which can be defined as:

$$J = \frac{V}{nD} \tag{3.28}$$

Where V is the free stream velocity, n is the propeller angular velocity in revolutions per second (RPS), and D is the propeller diameter.

To validate the BEMT code, the C_t and C_p experimental results of the three bladed propeller C were compared against the BEMT results. The propeller geometry characteristics were obtained from the report and a 18 elements discretization with an element width of 10% of the propeller radius was used for the BEMT code. Three different geometrical twist angles of propeller C were compared : 25°, 30°, and 35° at 0.75R, with R the blade radius. The flow conditions used were: air density $\rho = 1.22 \ kg/m^3$ and air viscosity 1.81E-5 kg/(ms). The propeller airfoil corresponded to a CLARK-Y airfoil. The lift C_L and drag C_D coefficients for a Reynold's number of Re = 50000 were used [71], shown in Figure 3.3 and Figure 3.4 respectively.

As shown in Figure 3.5 and Figure 3.6, the BEMT model shows good agreement with the experimental results for the linear part of \mathcal{C}_T and \mathcal{C}_P , sightly underpredicting \mathcal{C}_T and \mathcal{C}_P . On the other hand, the non-linear behavior at low advance ratio of \mathcal{C}_T and \mathcal{C}_P differs between the experiments and the model. As the airfoil coefficients were obtained for static conditions, at low advance ratio, some elements in the propeller operate in stall conditions due to high inflow angles and thus, a boundary-layer separation from the airfoil occurs. But in a propeller, this boundary-layer separation is delayed by the Coriolis effect, due to the flow angular speed induced by the propeller [72]. BEMT does not capture this boundary-layer effect and tends to under predict \mathcal{C}_T and \mathcal{C}_P for low advance ratios.

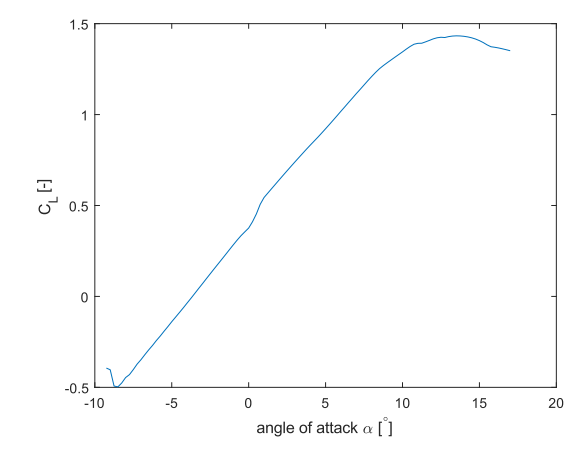


Figure 3.3: Lift coefficient C_L of CLARK-Y [71]

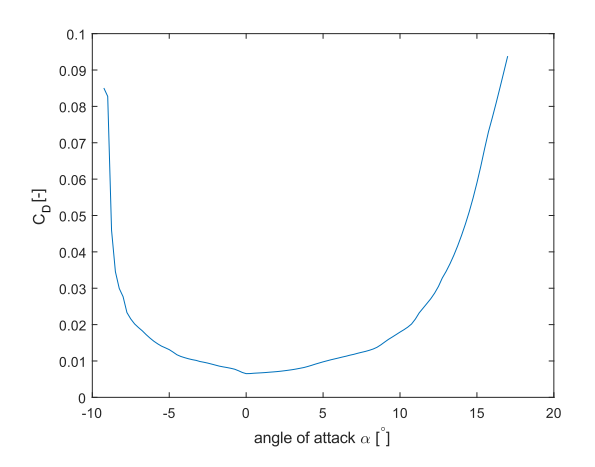


Figure 3.4: Drag coefficient C_D of CLARK-Y [71]

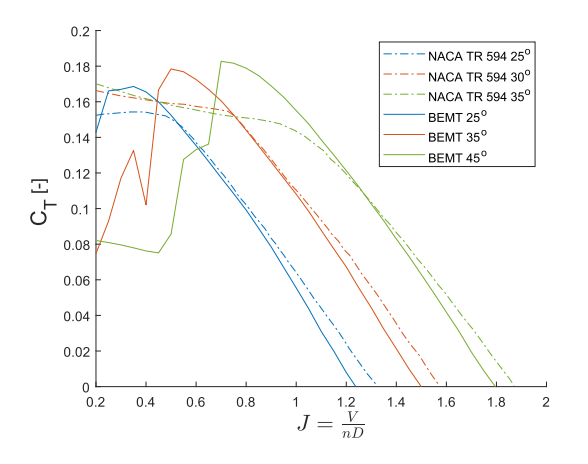


Figure 3.5: Thrust coefficient for propeller C [70]

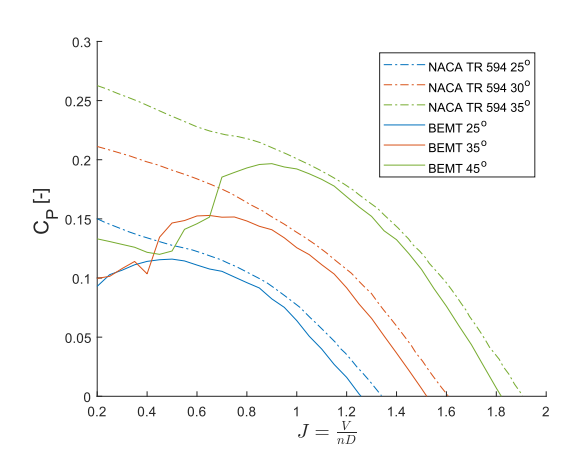


Figure 3.6: Power coefficient for propeller C [70]

3.1.7. Extension of BEMT to counter-rotating propellers

The extension of BEMT to include counter-rotating propeller configuration is based in the BEMT model developed by Siddapaji and Turner [65]. The model proposed by Siddapaji and Turner [65] consists of a modification of Rwigema BEMT model [50] to account for the downstream propeller of the counter-rotating configuration. Apart from the BEMT inherent assumptions, two new assumptions are introduced: the rear propeller is situated in the fully developed stream of the front propeller, and only the front propeller wake affects the inflow of the rear propeller, without the rear propeller affecting the front propeller flow conditions.

A schematic model of the counter-rotating BEMT is shown in Figure 3.7. In this model, four induction factors are introduced: the front propeller axial a_f and tangential a_f' induction factors , and the rear propeller axial a_r and tangential a_r' induction factors respectively. Then, the velocities of Figure 3.7 can be defined in terms of the induction factors:

$$V_{2} = V_{\infty} (1 + a_{f}) V_{2} = V_{3}$$

$$V_{4} = V_{\infty} (1 + 2a_{f}) V'_{4} = V_{\infty} (1 + 2a_{f}x)$$

$$V_{5} = V'_{4} (1 + a_{r}) V_{5} = V_{6}$$

$$V_{7} = V_{4} (1 + 2a_{r})$$
(3.29)

Where V_{∞} is the free-stream inflow velocity.

As the rear propeller does not affect the front propeller, the momentum theory and element theory applied to the front propeller lead to the same result of section 3.1:

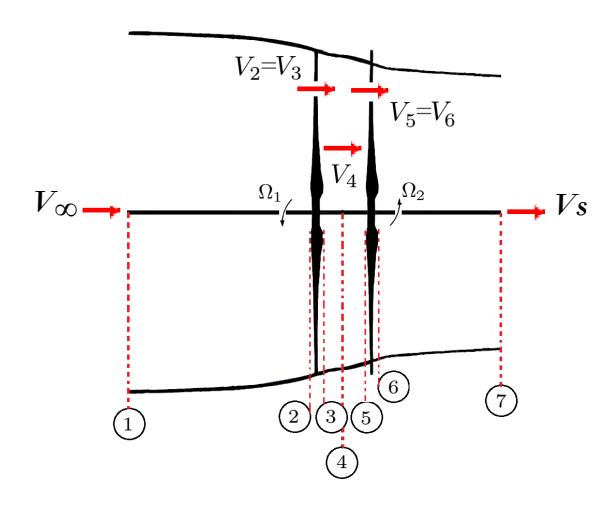


Figure 3.7: counter-rotating propeller model (adapted from [65]).

$$\tan \phi_f = \frac{V_{\infty} (1 + a_f)}{\Omega_f r (1 - a_f')}$$

$$U_f = \frac{V_{\infty} (1 + a_f)}{\sin \phi_f}$$
(3.30)

$$dT_f = \frac{1}{2} B \rho U_f^2 \left(C_L(\alpha_f) \cos \phi_f - C_D(\alpha_f) \sin \phi_f \right) c dr$$

$$dQ_f = \frac{1}{2} B \rho U_f^2 \left(C_L(\alpha_f) \sin \phi_f + C_D(\alpha_f) \cos \phi_f \right) c r dr$$

$$dT_f = 4\pi F_f r \rho V_\infty^2 \left(1 + a_f \right) a_f dr$$

$$dQ_f = 4\pi F_f r^3 \rho V_\infty \left(1 + a_f \right) \Omega_f a_f' dr$$

$$(3.31)$$

On the other hand, the rear propeller inflow is affected by the front propeller wake. Due to mass conservation and the assumption of incompressible flow, the acceleration of the flow produced by the front propeller generates a wake contraction effect. To account for this effect on the rear propeller inflow characteristics, Leishman and Ananthan [73] developed a correction factor a, which corrects the inflow velocity in the rear propeller of coaxial rotors. The correction factor a developed in this thesis is based in a and it can be derived from mass conservation:

$$d\dot{m}_3 = d\dot{m}_4 \rho A_3 V_3 = \rho A_4 V_4$$
 (3.32)

$$x = \frac{A_4}{A_3} = \frac{V_3}{V_4} = \frac{1 + a_f}{1 + 2a_f}$$

$$x \approx \frac{1 + a_f^{0.75R}}{1 + 2a_f^{0.75R}}$$
(3.33)

Where $a_f^{0.75R}$ is the front propeller axial induction factor of the element located at the three-quarter propeller radius. Using the correction factor x, the adjusted inflow velocity in the rear propeller V_4' can be obtained:

$$V_4' = V_\infty (1 + 2a_f x)$$
 (3.29 revisited)

Also, the front propeller induces an angular velocity in the wake. Therefore, the inflow in the rear propeller, which is located in the fully developed wake, has an angular velocity ω_4' , equal to the front propeller wake angular velocity ω_4 :

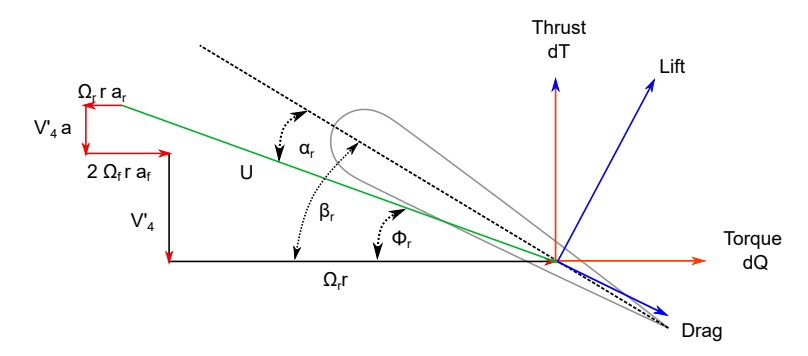


Figure 3.8: Blade element diagram for a counter-rotating propeller.

$$\omega_4 = \omega_4' = 2 \Omega_f \alpha_f' \tag{3.34}$$

Now, having the inflow characteristics for the rear propeller, shown in Figure 3.8, the local inflow angle ϕ_r and local inflow velocity U_r of the rear propeller can be calculated:

$$\tan \phi_r = \frac{V_4' (1 + a_r)}{2 r \Omega_f a_f' + r \Omega_r (1 - a_r')}$$

$$U_r = \frac{V_4' (1 + a_r)}{\sin \phi_r}$$
(3.35)

Using the blade momentum theory explained in subsection 3.1.1, the thrust and torque of an annular element can be obtained:

$$dT_r = 4\pi F_r r \rho V_4'^2 (1 + a_r) a_f dr$$

$$dQ_r = 4\pi F_r r^3 \rho V_4' (1 + a_r) (\Omega_f a_f' + \Omega_r a_r') dr$$
(3.36)

Additionally, using the blade element theory explained in subsection 3.1.2,the thrust and torque of an element can be written as:

$$dT_r = \frac{1}{2} B \rho U_r^2 \left(C_L(\alpha_r) \cos \phi_r - C_D(\alpha_r) \sin \phi_r \right) c dr$$

$$dQ_r = \frac{1}{2} B \rho U_r^2 \left(C_L(\alpha_r) \sin \phi_r + C_D(\alpha_r) \cos \phi_r \right) c r dr$$
(3.37)

Then, a total of eight equations are obtained, four for the front propeller and four for the rear propeller. To solve the system of equations, first it is solved separately for the front propeller, using the same numerical approach as subsection 3.1.5:

$$R_f(a_f, a_f') = |dT_f^{el} - dT_f^{mom}| + |dQ_f^{el} - dQ_f^{mom}|$$

$$[a_f, a_f'] = min\{R_f(a_f, a_f')\}$$
(3.38)

Afterward, using the results of the front propeller, the inflow conditions of the rear propeller can be obtained. with the inflow conditions defined, the rear propeller thrust and torque equations can be solved in the same manner as in subsection 3.1.5:

$$R_r(a_r, a_r') = |dT_r^{el} - dT_r^{mom}| + |dQ_r^{el} - dQ_r^{mom}|$$

$$[a_r, a_r'] = min\{R_r(a_r, a_r')\}$$
(3.39)

Using the BEMT aerodynamic results for the fixed propeller, next the aerodynamics produced by the propeller gyroscopic motion will be derived.

3.2. Whirl flutter aerodynamics

As mentioned in section 2.1, whirl flutter is produced by the interaction between the propeller aerodynamics and the structure of the nacelle. The gyroscopic motion of the propeller, sometimes called whirl motion, causes unsteady aerodynamics which could lead to whirl flutter. The unsteady aerodynamic forces of the propeller can be represented by the forces P_y , P_z and the moments M_y , M_z , shown in Figure 3.9.

To obtain these forces and moment, various analytical models have been developed. It has been shown that the analytical models are able to predict the whirl flutter speeds, but with conservative results [12]. It is important to point out that the analytical models already developed use windmilling conditions to obtain the propeller aerodynamic forces.

For this thesis, a linear perturbation analysis is used to derive the whirl forces, as was done by Houbolt and Reed [1], but introducing some modifications to include thrust conditions. Houbolt-Reed's model and BEMT are based on strip theory, which allows the coupling of BEMT with Houbolt-Reed's model to obtain the aerodynamic whirl forces, including the thrust conditions. Additionally, Houbolt-Reed's model is a reliable model to calculate whirl flutter boundaries, as it has been extensively used in the literature and validated against experimental results [12], which makes it a perfect candidate for the semi-analytical model generated in this thesis.

The model from which the whirl forces are obtained is shown in Figure 2.1 and Figure 3.9. It consists of a rigid propeller attached to a rigid truss with flexible pitch (θ) and yaw (ψ) degrees of freedom.

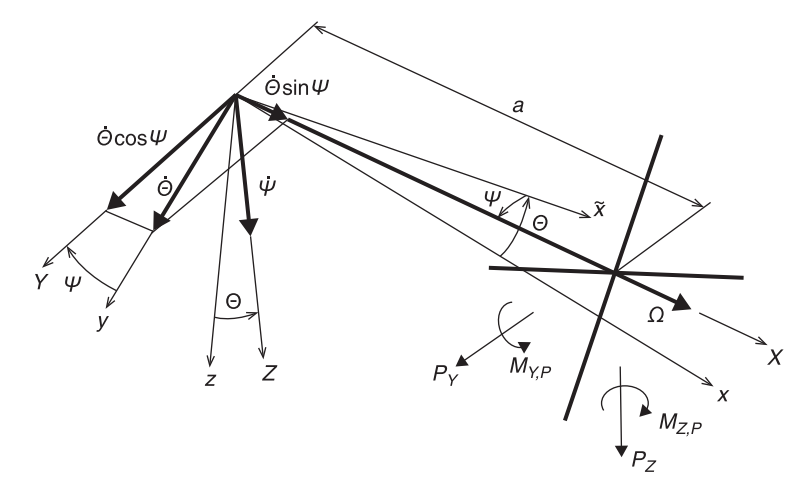


Figure 3.9: Whirl forces of the gyroscopic system [5].

3.2.1. Perturbation quantities

As already mentioned, a linear perturbation analysis will be used to derive the whirl forces generated by the gyroscopic motion. Three perturbation quantities arise from the gyroscopic motion produced by the gyroscopic motion of θ and ψ . The perturbation quantities shown in Figure 3.10 are composed by a velocity \dot{s} in the same plane as the propeller disk, a velocity \dot{w} perpendicular to the propeller disk, and a geometric change of the angle of attack α_1 [1].

As the perturbation quantities depend on radial position, it is necessary to define them for an arbitrary point P located in one of the blades and positioned at a distance r from the propeller center. Considering the coordinate system and model of Figure 3.11 and Figure 3.12, and using small angle approximation, the coordinates of point P can be expressed as:

$$y = y_1 + r\cos(\Omega t)$$

$$z = z_1 + r\sin(\Omega t)$$

$$x = -\psi r\cos(\Omega t) - \theta r\sin(\Omega t)$$
(3.40)

$$y_1 = e_{\psi}\psi$$

$$z_1 = e_{\theta}\theta \tag{3.41}$$

With e_{ψ} , e_{θ} the distances from the degree of freedom pivot location and Ω the propeller angular speed.

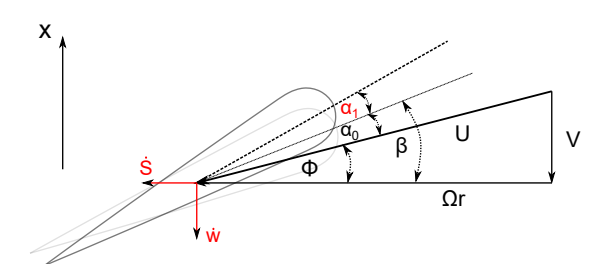


Figure 3.10: Perturbation quantities due to whirl motion.

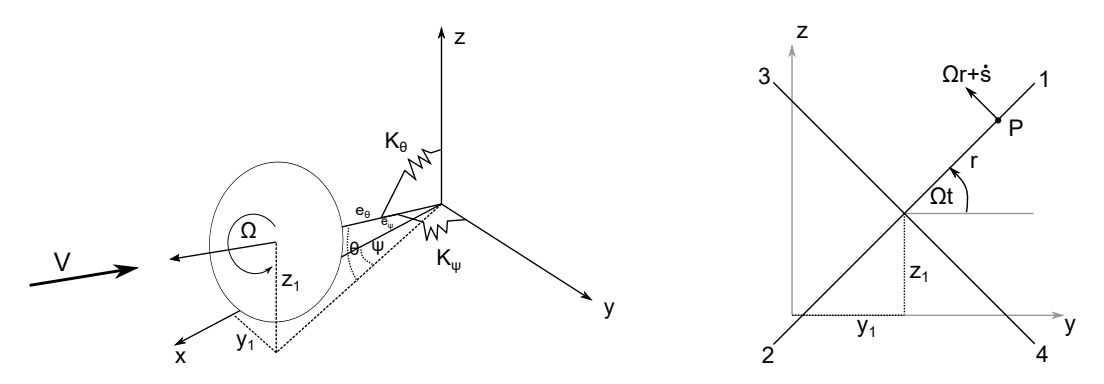


Figure 3.11: Model used to get the aerodynamic forces. Figure 3.12: Front view of the propeller model with four blades.

Then, the perturbation quantities \dot{s} , \dot{w} and α_1 can be defined as:

$$\dot{s} = \dot{z}_1 \cos(\Omega t) - \dot{y}_1 \sin(\Omega t)$$

$$\dot{w} = \dot{x} = \Omega \psi r \sin(\Omega t) - r \dot{\theta} \sin(\Omega t) - \Omega r \theta \cos(\Omega t) - \dot{\psi} r \cos(\Omega t)$$

$$\alpha_1 = \psi \sin(\Omega t) - \theta \cos(\Omega t)$$
(3.42)

With the perturbation quantities defined for an arbitrary point P, the propeller unsteady forces can be derived using strip theory for an element located at P.

3.2.2. Propeller unsteady forces using strip theory

Using strip theory, the blade can be divided in sections from which the lift and drag can be calculated using the 2-D geometry and local flow characteristics. To include the thrust effects, BEMT is coupled with the perturbation model. The coupling consists of including the induced velocities calculated by BEMT in the calculation of the propeller unsteady forces. Considering the naming convention of Figure 3.10, the velocities already include the induced velocities calculated by BEMT. Therefore:

$$V = V_{\infty}(1+a)$$

$$\Omega = \Omega_{propeller}(1-a')$$

$$U = \sqrt{V^2 + (\Omega r)^2}$$
(3.43)

Where a,a' are the radial and tangential induction factors respectively, and r is the radial position of the element.

To get the unsteady forces, it is necessary to first calculate the perturbed lift and drag. The lift and drag will depend directly on the angle of attack and inflow velocity. The perturbation velocities \dot{s} and \dot{w} generate a normal component and a parallel component to the local inflow velocity U.

The normal component to U for an element is:

$$-\dot{w}\frac{\Omega r}{U} + \dot{s}\frac{V}{U} \tag{3.44}$$

The parallel component to U is:

$$\dot{w}\frac{V}{U} + \dot{s}\frac{\Omega r}{U} \tag{3.45}$$

The perturbed inflow velocity U_p can be calculated as:

$$U_{p} = U + \Delta U$$

$$\Delta U = \frac{V \dot{w}}{U} + \frac{\Omega r \dot{s}}{U}$$

$$U_{p} = \frac{U^{2} + V \dot{w} + \Omega r \dot{s}}{U}$$
(3.46)

Then, the first order approximation for the perturbed angle of attack can be calculated. Considering the normal components due to \dot{s} and \dot{w} , the perturbed angle of attack can be written as:

$$\alpha = \alpha_0 + \Delta \alpha$$

$$\Delta \alpha = \alpha_1 + \frac{V \dot{s}}{U^2} - \frac{\Omega r \dot{w}}{U^2}$$

$$\alpha = \alpha_0 + \alpha_1 + \frac{V \dot{s}}{U^2} - \frac{\Omega r \dot{w}}{U^2}$$
(3.47)

Where α_0 is the steady state angle of attack. Consequently, the perturbed lift for a section can be expressed as:

$$dL = \frac{1}{2} \rho c U_p^2 C_L(\alpha) dr$$
 (3.48)

Where ρ is the flow density, c is the element blade chord, C_L is the lift coefficient of the airfoil, and dr is the element width. Additionally, U_p^2 can be written as:

$$U_p^2 = 2V\dot{w} + U^2 + 2\Omega r\dot{s} + \frac{V^2\dot{w}^2}{U^2} + \frac{\Omega^2 r^2\dot{s}^2}{U^2} + \frac{2\Omega V r\dot{s}\dot{w}}{U^2}$$

Ignoring higher-order terms:

$$U_n^2 \approx U^2 + 2V\dot{w} + 2\Omega r\dot{s} \tag{3.49}$$

As the lift coefficient C_L is a function of α , a linear approximation can be used to represent C_L [28] to get the lift of a section without implicit dependence on α :

$$C_L(\alpha) \approx a_0 + a_1 \alpha \tag{3.50}$$

Where a_0 and a_1 are the adjusted coefficients of the linear approximation.

Replacing in Equation 3.48:

$$dL = \frac{1}{2} \rho c \left(U^2 + 2 V \dot{w} + 2 \Omega r \dot{s} \right) \left(a_0 + a_1 \alpha_0 + a_1 \left(\alpha_1 + \frac{V \dot{s}}{U^2} - \frac{\Omega r \dot{w}}{U^2} \right) \right) dr$$
 (3.51)

Ignoring higher-order terms:

$$dL \approx \frac{1}{2} \rho c U^2 dr \left[a_0 + a_1 (\alpha_0 + \alpha_1) \right] + \frac{1}{2} \rho c dr \left[2 V a_0 + 2 V a_1 \alpha_0 - \Omega a_1 r \right] \dot{w}$$

$$+ \frac{1}{2} \rho c dr \left[V a_1 + 2 \Omega a_0 r + 2 \Omega a_1 \alpha_0 r \right] \dot{s} \quad (3.52)$$

Replacing Equation 3.42 in Equation 3.52, the section lift can be written as:

$$dL = L_{steady} + L_s \sin(\Omega t) + L_c \cos(\Omega t)$$
(3.53)

Where L_{steady} , L_s and L_c are:

$$L_{steady} = \frac{1}{2}\rho c U^{2}(a_{0} + a_{1}\alpha_{0})dr$$

$$L_{s} = C_{L,\psi}\left(\psi - \frac{\dot{y_{1}}}{V}\right) + C_{L,\dot{\theta}}\dot{\theta}$$

$$L_{c} = C_{L,\theta}\left(\theta - \frac{\dot{z_{1}}}{V}\right) + C_{L,\dot{\psi}}\dot{\psi}$$
(3.54)

Where $C_{L,\psi}$, $C_{L,\theta}$ and $C_{L,\dot{\theta}}$ are:

$$\begin{split} C_{L,\psi} &= \frac{1}{2} \rho \, c \, V \, (V a_1 + 2 \Omega r a_0 + 2 \Omega r a_1 \alpha_0) dr \\ C_{L,\theta} &= -\frac{1}{2} \rho \, c \, V \, (V a_1 + 2 \Omega r a_0 + 2 \Omega r a_1 \alpha_0) \, dr \\ C_{L,\psi} &= -\frac{1}{2} \rho \, c (2 V a_0 + 2 V a_1 \alpha_0 - \Omega r a_1) \, dr \\ C_{L,\dot{\theta}} &= -\frac{1}{2} \rho \, c \, (2 V a_0 + 2 V a_1 \alpha_0 - \Omega r a_1) \, dr \end{split} \tag{3.55}$$

The drag of a section can be calculated in the same way as the lift:

$$dD = \frac{1}{2} \rho c U_p^2 C_D(\alpha) dr$$
 (3.56)

Where ρ is the flow density, c is the element blade chord, C_D is the drag coefficient of the airfoil, and dr is the element width.

In the case of the drag coefficient, a quadratic approximation is used for the drag coefficient [28] to get the drag of a section without implicit dependence on α :

$$C_D(\alpha) \approx d_0 + d_1 \alpha + d_2 \alpha^2 \tag{3.57}$$

Where d_0 , d_1 and d_2 are the adjusted coefficients of the quadratic approximation. Replacing in Equation 3.56:

$$dD = \frac{1}{2} \rho c \left(U^2 + 2 V \dot{w} + 2 \Omega r \dot{s} \right)$$

$$\left(d_0 + \alpha_0 d_1 + {\alpha_0}^2 d_2 + d_1 \left(\alpha_1 + \frac{V \dot{s}}{U^2} - \frac{\Omega r \dot{w}}{U^2} \right) + \alpha_0 d_2 \left(\alpha_1 + \frac{V \dot{s}}{U^2} - \frac{\Omega r \dot{w}}{U^2} \right) \right) dr \quad (3.58)$$

Ignoring higher-order terms:

$$dD \approx \frac{1}{2}\rho c U^{2} dr \left[\sigma_{1} + (d_{1} + \alpha_{0} d_{2})\right] \alpha_{1} + \frac{1}{2}\rho c dr \left[2\Omega r \sigma_{1} + V d_{1} + V \alpha_{0} d_{2}\right] \dot{s}$$

$$+ \frac{1}{2}\rho c dr \left[2V \sigma_{1} - \Omega r d_{1} + \Omega r \alpha_{0} d_{2}\right] \dot{w} \quad (3.59)$$

$$\sigma_{1} = d_{2} \alpha_{0}^{2} + d_{1} \alpha_{0} + d_{0}$$

Replacing Equation 3.42 in Equation 3.59:

$$dD = D_{steady} + D_s \sin(\Omega t) + D_c \cos(\Omega t)$$
(3.60)

Where D_{steady} , D_s and D_c are:

$$D_{steady} = \frac{1}{2} \rho c U^{2} (d_{0} + d_{1}\alpha_{0} + d_{2}\alpha_{0}^{2}) dr$$

$$D_{s} = C_{D,\psi} \left(\psi - \frac{\dot{y_{1}}}{V} \right) + C_{D,\dot{\theta}} \dot{\theta}$$

$$D_{c} = C_{D,\theta} \left(\theta - \frac{\dot{z_{1}}}{V} \right) + C_{D,\dot{\psi}} \dot{\psi}$$
(3.61)

Where $C_{D,\psi}$, $C_{D,\theta}$, $C_{D,\dot{\psi}}$ and $C_{D,\dot{\theta}}$ are:

$$C_{D,\psi} = \frac{1}{2} \rho c V \left(V(d_1 + \alpha_0 d_2) + 2\Omega r(d_0 + \alpha_0 d_1 + \alpha_0^2 d_2) \right) dr$$

$$C_{D,\theta} = -\frac{1}{2} \rho c V \left(V(d_1 + \alpha_0 d_2) + 2\Omega r(d_0 + \alpha_0 d_1 + \alpha_0^2 d_2) \right) dr$$

$$C_{D,\psi} = -\frac{1}{2} \rho c \left(2V(d_0 + \alpha_0 d_1 + \alpha_0^2 d_2) - \Omega r(d_1 + \alpha_0 d_2) \right) dr$$

$$C_{D,\theta} = -\frac{1}{2} \rho c \left(2V(d_0 + \alpha_0 d_1 + \alpha_0^2 d_2) - \Omega r(d_1 + \alpha_0 d_2) \right) dr$$

$$(3.62)$$

Afterward, the thrust and torque of a blade element can be calculated as:

$$dT = dL \cos(\phi) - dD \sin(\phi)$$

$$dO = r (dL \sin(\phi) + dD \cos(\phi))$$
(3.63)

In Figure 3.10, it can be seen that $\sin(\phi)$ and $\cos(\phi)$ can be expressed as:

$$\sin(\phi) = \frac{V}{U} \quad \cos(\phi) = \frac{\Omega r}{U} \tag{3.64}$$

Combining Equation 3.64 with Equation 3.63, the blade element thrust and torque can be written as:

$$dT = dL \frac{\Omega r}{U} - dD \frac{V}{U}$$

$$dQ = r \left(dL \frac{V}{U} + dD \frac{\Omega r}{U} \right)$$
(3.65)

Replacing Equation 3.53 and Equation 3.60 in Equation 3.65, the blade element thrust and torque can be be also expressed as:

$$dT = L_{steady} \frac{\Omega r}{U} - D_{steady} \frac{V}{U} + \left(L_s \frac{\Omega r}{U} - D_s \frac{V}{U} \right) \sin(\Omega t) + \left(L_c \frac{\Omega r}{U} - D_c \frac{V}{U} \right) \cos(\Omega t)$$

$$dQ = r \left[L_{steady} \frac{V}{U} + D_{steady} \frac{\Omega r}{U} + \left(L_s \frac{V}{U} + D_s \frac{\Omega r}{U} \right) \sin(\Omega t) + \left(L_c \frac{V}{U} + D_c \frac{\Omega r}{U} \right) \cos(\Omega t) \right]$$
(3.66)

As shown in Figure 3.13, in a propeller with two blades, one blade has a rotational angle of Ωt and the second $\Omega t + \pi$ (blade 2 in Figure 3.13). Also, in Figure 3.13, it can be deduced that the forces P_y and P_z are produced by the torque component of the blades. On the other hand, M_y and M_z are produced by the blades thrust component. Considering a 2-blade propeller, the unsteady aerodynamic forces for a blade element can be calculated as:

$$dP_{y} = \frac{1}{r} (dQ(\Omega t) - dQ(\Omega t + \pi)) \sin(\Omega t)$$

$$dP_{z} = -\frac{1}{r} (dQ(\Omega t) - dQ(\Omega t + \pi)) \cos(\Omega t)$$

$$dM_{y} = -r(dT(\Omega t) - dT(\Omega t + \pi)) \sin(\Omega t)$$

$$dM_{y} = -r(dT(\Omega t) - dT(\Omega t + \pi)) \cos(\Omega t)$$
(3.67)

Where dT and dQ are the element thrust and torque respectively. Replacing Equation 3.66, Equation 3.54, and Equation 3.61 in Equation 3.67, and using the coordinate system of Figure 3.9:

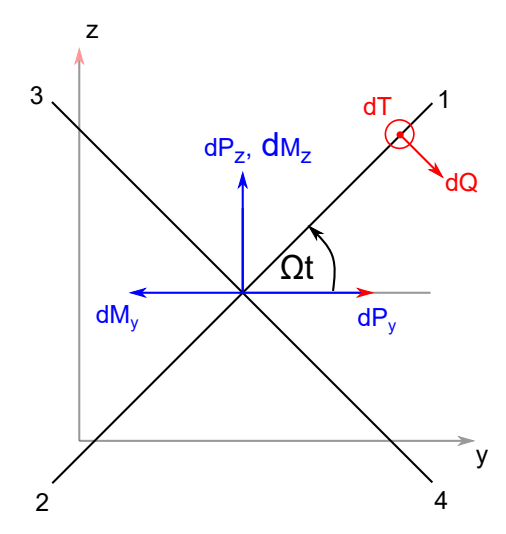


Figure 3.13: Whirl forces of the propeller related to blade thrust and torque

$$dP_{y} = \frac{2\sin(\Omega t)}{U} \left[A\overline{\psi} + B\dot{\overline{\psi}} + C\overline{\theta} + D\dot{\overline{\theta}} \right]$$

$$dP_{z} = -\frac{2\cos(\Omega t)}{U} \left[A\overline{\psi} + B\dot{\overline{\psi}} + C\overline{\theta} + D\dot{\overline{\theta}} \right]$$

$$dM_{y} = -\frac{2r\sin(\Omega t)}{U} \left[E\overline{\psi} + H\dot{\overline{\theta}} + F\dot{\overline{\psi}} + G\overline{\theta} \right]$$

$$dM_{z} = \frac{2r\cos(\Omega t)}{U} \left[E\overline{\psi} + H\dot{\overline{\theta}} + F\dot{\overline{\psi}} + G\overline{\theta} \right]$$

$$A = \sin(\Omega t) \left[C_{L,\psi}V + C_{D,\psi}\Omega r \right] \quad B = \cos(\Omega t) \left[C_{L,\psi}V + C_{D,\psi}\Omega r \right]$$

$$C = \cos(\Omega t) \left[C_{L,\theta}V + C_{D,\theta}\Omega r \right] \quad D = \sin(\Omega t) \left[C_{L,\theta}V + C_{D,\theta}\Omega r \right]$$

$$E = \sin(\Omega t) \left[C_{D,\psi}V - C_{L,\psi}\Omega r \right] \quad F = \cos(\Omega t) \left[C_{D,\psi}V - C_{L,\psi}\Omega r \right]$$

$$G = \cos(\Omega t) \left[C_{D,\theta}V - C_{L,\theta}\Omega r \right] \quad H = \sin(\Omega t) \left[C_{D,\theta}V - C_{L,\theta}\Omega r \right]$$

Equation 3.68 is written using aerodynamic effective angles and ignoring second time derivatives:

$$\overline{\psi} = \theta - \frac{\dot{y}}{V}$$

$$\overline{\theta} = \theta - \frac{\dot{z}}{V}$$
(3.69)

It can be seen that in Equation 3.68, the unsteady forces explicitly depend on Ωt , which is a representation of the position of the blade at a time t. This time dependence adds complexity to the stability analysis because eigenvalue analysis cannot be directly used. Therefore, it is convenient to have an expression that does not depend on the position of the blades so the stability analysis can be done using eigenanalysis. The condition for the forces to be independent of blade position is called rotational symmetry of the propeller rotor, and it can be derived from a four-bladed propeller and applied to propellers with three or more blades [28].

Considering a four-bladed propeller, shown in Figure 3.12, the thrust and torque of the blades can be calculated depending on the propeller rotational angle:

Blade 1 :
$$dT_1$$
, dQ_1 : Ωt
Blade 2 : dT_2 , dQ_2 : $\Omega t + \pi$
Blade 3 : dT_3 , dQ_3 : $\Omega t + \frac{\pi}{2}$ (3.70)
Blade 4 : dT_4 , dQ_4 : $\Omega t + \frac{3\pi}{2}$

Then, the unsteady aerodynamic forces for a four bladed propeller can be written as:

$$dP_{y} = \frac{1}{r} \left((dQ_{1} - dQ_{2}) \sin(\Omega t) + (dQ_{3} - dQ_{4}) \cos(\Omega t) \right)$$

$$dP_{z} = \frac{1}{r} \left(-(dQ_{1} - dQ_{2}) \cos(\Omega t) + (dQ_{3} - dQ_{4}) \sin(\Omega t) \right)$$

$$dM_{y} = r \left(-(dT_{1} - dT_{2}) \sin(\Omega t) - (dT_{3} - dT_{4}) \cos(\Omega t) \right)$$

$$dM_{z} = r \left(-(dT_{1} - dT_{2}) \cos(\Omega t) + (dT_{3} - dT_{4}) \sin(\Omega t) \right)$$
(3.71)

Replacing Equation 3.66, Equation 3.54, and Equation 3.61 in Equation 3.71 and using the coordinate system of Figure 3.9, the unsteady forces are:

$$dP_{y} = \frac{2}{U} \left[(C_{L,\psi}V + C_{D,\psi}\Omega r)\overline{\psi} - (C_{L,\dot{\theta}}V + C_{D,\dot{\theta}}\Omega r)\dot{\overline{\theta}} \right]$$

$$dP_{z} = -\frac{2}{U} \left[(C_{L,\dot{\psi}}V + C_{D,\dot{\psi}}\Omega r)\dot{\overline{\psi}} - (C_{L,\theta}V + C_{D,\theta}\Omega r)\overline{\theta} \right]$$

$$dM_{y} = \frac{2r}{U} \left[(C_{L,\psi}\Omega r - C_{D,\psi}V)\overline{\psi} - (C_{L,\dot{\theta}}\Omega r - C_{D,\dot{\theta}}V)\dot{\overline{\theta}} \right]$$

$$dM_{z} = -\frac{2r}{U} \left[(C_{L,\dot{\psi}}\Omega r - C_{D,\dot{\psi}}V)\dot{\overline{\psi}} - (C_{L,\theta}\Omega r - C_{D,\theta}V)\overline{\theta} \right]$$
(3.72)

As mentioned earlier, the rotational symmetry condition can be applied for propellers with three or more blades [28]. Then, Equation 3.72 can be adjusted for different number of blades:

$$dP_{y} = \frac{B}{4} \frac{2}{U} \left[(C_{L,\psi}V + C_{D,\psi}\Omega r)\overline{\psi} - (C_{L,\dot{\theta}}V + C_{D,\dot{\theta}}\Omega r)\dot{\overline{\theta}} \right]$$

$$dP_{z} = -\frac{B}{4} \frac{2}{U} \left[(C_{L,\dot{\psi}}V + C_{D,\dot{\psi}}\Omega r)\dot{\overline{\psi}} - (C_{L,\theta}V + C_{D,\theta}\Omega r)\overline{\theta} \right]$$

$$dM_{y} = \frac{B}{4} \frac{2r}{U} \left[(C_{L,\psi}\Omega r - C_{D,\psi}V)\overline{\psi} - (C_{L,\dot{\theta}}\Omega r - C_{D,\dot{\theta}}V)\dot{\overline{\theta}} \right]$$

$$dM_{z} = -\frac{B}{4} \frac{2r}{U} \left[(C_{L,\dot{\psi}}\Omega r - C_{D,\dot{\psi}}V)\dot{\overline{\psi}} - (C_{L,\theta}\Omega r - C_{D,\theta}V)\overline{\theta} \right]$$

$$(3.73)$$

With B blades. Finally, the total forces for a propeller divided in 'n' sections can be obtained:

$$P_{y} = \sum_{i}^{n} dP_{y} = C_{1}\overline{\psi} + C_{2}\dot{\overline{\theta}} \qquad P_{z} = \sum_{i}^{n} dP_{z} = C_{3}\dot{\overline{\psi}} + C_{4}\overline{\theta}$$

$$M_{y} = \sum_{i}^{n} dM_{y} = C_{5}\overline{\psi} + C_{6}\dot{\overline{\theta}} \qquad M_{z} = \sum_{i}^{n} dM_{z} = C_{7}\dot{\overline{\psi}} + C_{8}\overline{\theta}$$

$$(3.74)$$

As shown in Appendix C, Equation 3.68 and Equation 3.73 lead to nearly identical results for the analyzed 2-bladed propeller in this thesis. Then, Equation 3.73 will be used for the aeroelastic model because it does not explicitly depend on time and therefore, it can be directly used for stability analysis using eigenanalysis.

3.2.3. Unsteady forces extension for counter-rotating propellers

In this section, the unsteady aerodynamic forces are extended for counter-rotating propellers, using the rotational symmetry approximation derived in subsection 3.2.2.

To obtain P_y , P_z , M_y and M_z for counter-rotating propellers, the unsteady forces are evaluated separately for the two propellers. One propeller is spinning counterclockwise, for which the forces were already derived in subsection 3.2.2. But the second propeller is spinning clockwise, for which the forces are derived in this section.

The velocities of the rear propeller are also obtained from the BEMT model:

$$V = V_4'(1 + a_r)$$

$$\Omega = \Omega_{propeller}(1 - a_r' + 2a_f')$$

$$U = \sqrt{V^2 + (\Omega r)^2}$$
(3.75)

For a propeller rotating clockwise, the coordinates of the center of the propeller remain the same as in the counterclockwise configuration, described by Equation 3.41. But the coordinates of the arbitrary point P changes to:

$$y = y_1 + r\cos(\Omega t)$$

$$z = z_1 - r\sin(\Omega t)$$

$$x = -\psi r\cos(\Omega t) + \theta r\sin(\Omega t)$$
(3.76)

Also, due to the clockwise configuration the perturbation quantities change to:

$$\dot{s} = -\dot{z}_1 \cos(\Omega t) - \dot{y}_1 \sin(\Omega t)$$

$$\dot{w} = \dot{x} = r \dot{\theta} \sin(\Omega t) - \dot{\psi} r \cos(\Omega t) + \Omega r \theta \cos(\Omega t) + \Omega \psi r \sin(\Omega t)$$

$$\alpha_1 = \theta \cos(\Omega t) + \psi \sin(\Omega t)$$
(3.77)

With the perturbation quantities defined, the process to obtain the unsteady forces is exactly the same as in subsection 3.2.2. The resultant forces are:

$$dP_{y} = \frac{B}{4} \frac{2}{U} \left[(C_{L,\psi}V + C_{D,\psi}\Omega r)\overline{\psi} + (C_{L,\dot{\theta}}V + C_{D,\dot{\theta}}\Omega r)\dot{\overline{\theta}} \right]$$

$$dP_{z} = \frac{B}{4} \frac{2}{U} \left[(C_{L,\dot{\psi}}V + C_{D,\dot{\psi}}\Omega r)\dot{\overline{\psi}} + (C_{L,\theta}V + C_{D,\theta}\Omega r)\overline{\theta} \right]$$

$$dM_{y} = -\frac{B}{4} \frac{2r}{U} \left[(C_{L,\psi}\Omega r - C_{D,\psi}V)\overline{\psi} + (C_{L,\dot{\theta}}\Omega r - C_{D,\dot{\theta}}V)\dot{\overline{\theta}} \right]$$

$$dM_{z} = -\frac{B}{4} \frac{2r}{U} \left[(C_{L,\dot{\psi}}\Omega r - C_{D,\dot{\psi}}V)\dot{\overline{\psi}} + (C_{L,\theta}\Omega r - C_{D,\theta}V)\overline{\theta} \right]$$
(3.78)

Finally, exactly the same as the whirl forces for a counterclockwise propeller, Equation 3.74, is used to get the total forces for a propeller divided in n' sections.

3.2.4. Comparison with previous models and experiments

To validate the model, Bland and Bennet's [12] experiments and measurements were used. Bland and Bennet measured the static aerodynamic stability derivatives of the propeller in windmilling condition for different propeller pitch angles β . Then Bland and Bennet compared the measured derivatives to the theoretical stability derivatives, calculated using Houbolt and Reed's model[1] and Ribner's model [25] .

Houbolt and Reed's model include the oscillatory wake effects due to the propeller gyroscopic motion [1]. The oscillatory wake induces a lag on the lift compared to the quasi-steady theory, which has a significant impact on the stability derivatives. Houbolt and Reed's model include the wake effects using Theodorsen function, a function that models the wake effects of an oscillatory wing.

The Theodorsen function assumes straight wake, a supposition that can be considered valid in the case of the wake of a propeller in fixed-wing aircraft. This is because whirl flutter is encountered at high forward speeds, where the propellers have high advance ratios and therefore, the wake close to the blades can be considered straight. On the contrary, in a multirotor, the propeller advance ratios are smaller than for a fixed-wing aircraft and therefore, the wake close to the propeller blades needs to be considered helical, which means the Theodorsen function is not applicable. For these reasons, the oscillatory wake effects were neglected and proposed to be analyzed in future work.

The propeller unsteady forces, obtained in Equation 3.74, can be also expressed using the aerodynamic stability derivatives of Bland and Bennet [12] as:

$$P_{y} = \frac{1}{2}\rho V^{2}S\left(C_{y,\psi}\overline{\psi} + C_{y,\theta}\overline{\theta} + C_{y,r}\frac{\dot{\overline{\psi}}R}{V} + C_{y,q}\frac{\dot{\overline{\theta}}R}{V}\right)$$

$$P_{z} = \frac{1}{2}\rho V^{2}S\left(C_{z,\psi}\overline{\psi} + C_{z,\theta}\overline{\theta} + C_{z,r}\frac{\dot{\overline{\psi}}R}{V} + C_{z,q}\frac{\dot{\overline{\theta}}R}{V}\right)$$

$$M_{y} = \rho V^{2}SR\left(C_{m,\psi}\overline{\psi} + C_{m,\theta}\overline{\theta} + C_{m,r}\frac{\dot{\overline{\psi}}R}{V} + C_{m,q}\frac{\dot{\overline{\theta}}R}{V}\right)$$

$$M_{z} = \rho V^{2}SR\left(C_{n,\psi}\overline{\psi} + C_{n,\theta}\overline{\theta} + C_{n,r}\frac{\dot{\overline{\psi}}R}{V} + C_{n,q}\frac{\dot{\overline{\theta}}R}{V}\right)$$

$$M_{z} = \rho V^{2}SR\left(C_{n,\psi}\overline{\psi} + C_{n,\theta}\overline{\theta} + C_{n,r}\frac{\dot{\overline{\psi}}R}{V} + C_{n,q}\frac{\dot{\overline{\theta}}R}{V}\right)$$

Due to the symmetry of the gyroscopic motion, some propeller aerodynamic derivatives are identical when drag is neglected:

$$C_{y,\psi} = -C_{z,\theta} C_{y,\theta} = C_{z,\psi} C_{y,r} = -C_{z,q} C_{y,q} = C_{z,r} C_{m,\psi} = -C_{n,\theta} C_{m,\theta} = C_{n,\psi} C_{m,r} = -C_{n,q} C_{m,q} = C_{n,r}$$
(3.80)

Where ρ is the free stream flow density, V is the free stream flow velocity, R is the propeller radius, and $S = \pi R^2$ is the propeller area.

As previously mentioned, the model proposed for the forces in Equation 3.74 did not consider oscillatory wake effects, leading to eight aerodynamic derivatives, instead of the sixteen presented in Equation 3.79. The terms shown in Equation 3.74 can be expressed in terms of some of the stability derivatives, shown in Equation 3.79, when drag is neglected and windmilling conditions are considered:

$$C_{1} = \frac{1}{2}\rho V^{2}SC_{y,\psi} \qquad C_{2} = \frac{1}{2}\rho V^{2}S\frac{R}{V}C_{y,q}$$

$$C_{3} = \frac{1}{2}\rho V^{2}S\frac{R}{V}C_{z,r} \quad C_{4} = \frac{1}{2}\rho V^{2}SC_{z,\theta}$$

$$C_{5} = \rho V^{2}SRC_{m,\psi} \qquad C_{6} = \rho V^{2}SR\frac{R}{V}C_{m,q}$$

$$C_{7} = \rho V^{2}SR\frac{R}{V}C_{n,q} \quad C_{8} = \rho V^{2}SRC_{n,\theta}$$

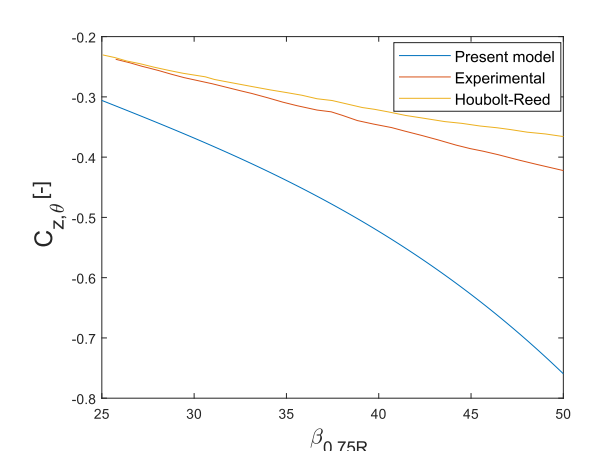
$$(3.81)$$

Considering the results available from Bland and Bennet [12], only $C_{z,\theta}$, $C_{m,\psi}$, and $C_{m,q}$ can be compared.

The results for $C_{z,\theta}$, $C_{m,\psi}$, and $C_{m,q}$ are shown in Figure 3.14, Figure 3.15, and Figure 3.16 respectively. Experimental results for $C_{m,q}$ were not available. The geometry and propeller parameters were obtained from Bland and Bennet report[12], windmilling conditions were considered, propeller angular velocity $\Omega=1800$ RPM, $\rho=1.22$ $[kg/m^3]$, drag was ignored, and the theoretical lift coefficient $C_L=2\pi\alpha$ was adjusted by the compressibility and finite-length correction factor:

$$C_L = 2\pi \frac{A_r}{2 + A_r \sqrt{1 - M_r^2}} \alpha \tag{3.82}$$

Where A_r is the blade aspect ratio and M_r is the Mach number at each section. It can be concluded that $C_{z,\theta}$ and $C_{m,q}$ tend to follow the same trend as the values obtained by Bland and Bennet [12], but with higher values. The higher values can be explained by the omission of the unsteady oscillatory wake effects. Accounting for the oscillatory wake and thus, for the phase lag effect, would reduce the aerodynamic derivatives as the lift is not instantaneous anymore. This will also lead to new aerodynamic derivatives shown in Equation 3.79. For the model presented in this thesis, $C_{m,\psi}$ was not able to capture the trend of the experimental value, but this discrepancy might also arise from the lift lag effect.



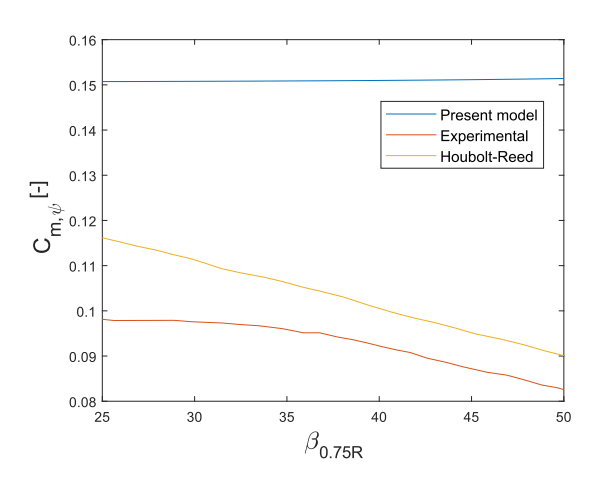


Figure 3.14: Comparison for aerodynamic derivative $C_{z,\theta}$

Figure 3.15: Comparison for aerodynamic derivative $\mathcal{C}_{m,\psi}$

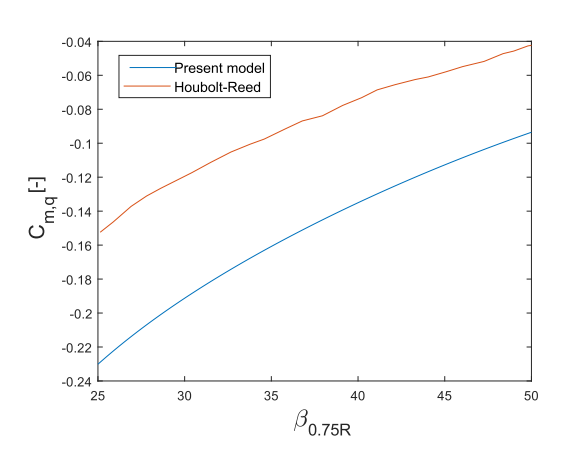


Figure 3.16: Comparison for aerodynamic derivative $C_{m,q}$

Structural model

To model the multirotor beam structure, the finite element method was chosen, as it has been widely used in the literature and because it can be easily coupled in the aeroelastic models [74].

More specifically, as the objective of this thesis is to generate a semi-analytical model to assess whirl flutter with low computational costs, finite elements with high number of degrees of freedom are avoided and a Euler-Bernoulli beam model is preferred. Additionally, beam models have been widely used to assess flutter in wings [74] and whirl flutter [75], which makes them a perfect candidate to model the multirotor beam structure.

For a finite element model, the structural equation of motion can be written as:

$$M\ddot{q} + C\dot{q} + K\dot{q} = F \tag{4.1}$$

Where M is the mass matrix, C is the mass matrix, K is the stiffness matrix, and F is the external nodal forces.

A beam finite element code was developed in MATLAB to be used in the stability analysis of the multirotor, which will be explained in the next section.

4.1. Beam model

The beam model is based on the space frame model of Katsikadelis [76] and Rao [77]. It considers a frame element with 6 degrees of freedom per node. Three axial DOF's u, v, w, one torsional DOF θ , and two bending DOF's ϕ, ψ were considered, as shown in Figure 4.1. It is important to mention that the element has a constant cross section and the material used is assumed to be isotropic.

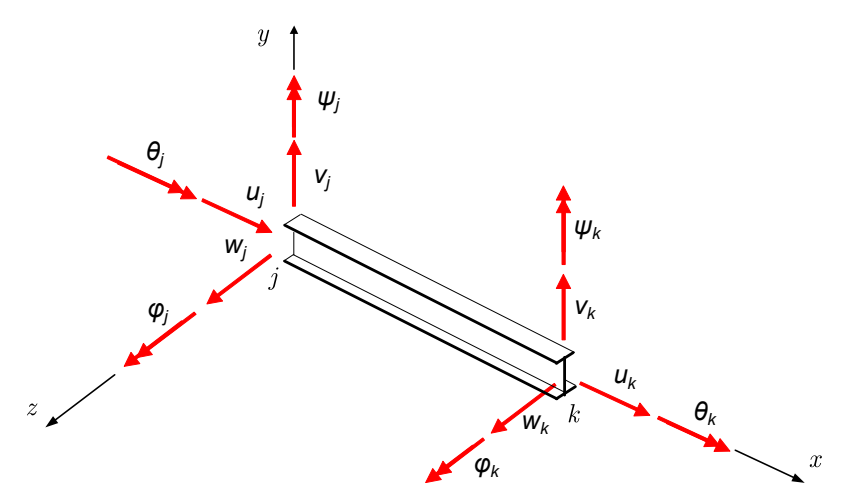


Figure 4.1: Frame element degrees of freedom (modified from [76])

The element vector of degrees of freedom, shown in Figure 4.1, is:

34 4. Structural model

$$q = \begin{bmatrix} u_j & v_j & w_j & \theta_j & \phi_j & \psi_j & u_k & v_k & w_k & \theta_k & \phi_k & \psi_k \end{bmatrix}^T$$
(4.2)

According to the space frame model derived by Katsikadelis [76], the element stiffness matrix and consistent mass matrix can be written as:

$$k_e^l = \begin{bmatrix} k_{jj} & k_{jk} \\ k_{kj} & k_{kk} \end{bmatrix} \tag{4.3}$$

$$k_{jj} = \frac{E}{L^{3}} \begin{bmatrix} L^{2}A & 0 & 0 & 0 & 0 & 0 \\ 0 & 12I_{z} & 0 & 0 & 0 & 6LI_{z} \\ 0 & 0 & 12I_{y} & 0 & -6LI_{y} & 0 \\ 0 & 0 & 0 & \frac{GJ}{E}L^{2} & 0 & 0 \\ 0 & 0 & -6LI_{y} & 0 & 4L^{2}I_{y} & 0 \\ 0 & 6LI_{z} & 0 & 0 & 0 & 4L^{2}I_{z} \end{bmatrix}$$
(4.4)

$$k_{kj} = (k_{jk})^T = \frac{E}{L^3} \begin{bmatrix} -L^2 A & 0 & 0 & 0 & 0 & 0 \\ 0 & -12I_z & 0 & 0 & 0 & -6LI_z \\ 0 & 0 & -12I_y & 0 & 6LI_y & 0 \\ 0 & 0 & 0 & -\frac{GJ}{E}L^2 & 0 & 0 \\ 0 & 0 & -6LI_y & 0 & 2L^2I_y & 0 \\ 0 & 6LI_z & 0 & 0 & 0 & 2L^2I_z \end{bmatrix}$$
(4.5)

$$k_{kk} = \frac{E}{L^3} \begin{bmatrix} L^2 A & 0 & 0 & 0 & 0 & 0 \\ 0 & 12I_z & 0 & 0 & 0 & -6LI_z \\ 0 & 0 & 12I_y & 0 & 6LI_y & 0 \\ 0 & 0 & 0 & \frac{G_I}{E}L^2 & 0 & 0 \\ 0 & 0 & 6LI_y & 0 & 4L^2I_y & 0 \\ 0 & -6LI_z & 0 & 0 & 0 & 4L^2I_z \end{bmatrix}$$

$$(4.6)$$

$$m_e^l = \begin{bmatrix} m_{jj} & m_{jk} \\ m_{kj} & m_{kk} \end{bmatrix} \tag{4.7}$$

$$m_{jj} = \frac{\rho AL}{420} \begin{bmatrix} 140 & 0 & 0 & 0 & 0 & 0\\ 0 & 156 & 0 & 0 & 0 & 22L\\ 0 & 0 & 156 & 0 & -22L & 0\\ 0 & 0 & 0 & 140r_g^2 & 0 & 0\\ 0 & 0 & -22L & 0 & 4L^2 & 0\\ 0 & 22L & 0 & 0 & 0 & 4L^2 \end{bmatrix}$$
(4.8)

$$m_{kj} = (m_{jk})^T = \frac{\rho AL}{420} \begin{bmatrix} 70 & 0 & 0 & 0 & 0 & 0 & 0 \\ 0 & 54 & 0 & 0 & 0 & 13L \\ 0 & 0 & 54 & 0 & -13L & 0 \\ 0 & 0 & 0 & 70r_g^2 & 0 & 0 \\ 0 & 0 & 13L & 0 & -3L^2 & 0 \\ 0 & -13L & 0 & 0 & 0 & -3L^2 \end{bmatrix}$$
(4.9)

$$m_{kk} = \frac{\rho AL}{420} \begin{bmatrix} 140 & 0 & 0 & 0 & 0 & 0 \\ 0 & 156 & 0 & 0 & 0 & -22L \\ 0 & 0 & 156 & 0 & 22L & 0 \\ 0 & 0 & 0 & 140r_g^2 & 0 & 0 \\ 0 & 0 & 22L & 0 & 4L^2 & 0 \\ 0 & -22L & 0 & 0 & 0 & 4L^2 \end{bmatrix}$$
 (4.10)

Where L is the element length, A is the area of the cross section of the element, I_y is the cross sectional moment of inertia around y axis, I_z is the cross sectional moment of inertia around z axis, J is the polar moment of inertia, $r_g = \sqrt{\frac{I_y + I_z}{A}}$ is the radius of gyration, ρ is the material density, E is the Young's modulus, and G is the shear modulus.

4.1. Beam model 35

To get the global stiffness and mass matrix, the rotation matrix for every element needs to be calculated, and then the element matrices can be transformed into global coordinates. The method shown in Rao [77] is used. The rotation matrix for the frame element can be expressed as:

$$k_e^g = R^T k_e^l R$$

$$m_e^g = R^T m_e^l R$$
(4.11)

$$R = \begin{bmatrix} \lambda & 0 & 0 & 0 \\ 0 & \lambda & 0 & 0 \\ 0 & 0 & \lambda & 0 \\ 0 & 0 & 0 & \lambda \end{bmatrix}$$
 (4.12)

$$\lambda = \lambda_1 \lambda_2 \tag{4.13}$$

$$\lambda_{1} = \frac{1}{d_{x}} \begin{bmatrix} l_{0x}d_{x} & m_{0x}d_{x} & n_{0x}d_{x} \\ -l_{0x}m_{0x} & d_{x}^{2} & -m_{0x}n_{0x} \\ -n_{0x} & 0 & l_{0x} \end{bmatrix}$$
(4.14)

$$l_{0x} = \frac{X_k - X_j}{L}$$

$$m_{0x} = \frac{Y_k - Y_j}{L}$$

$$n_{0x} = \frac{Z_k - Z_j}{L}$$

$$d_x = \sqrt{l_{0x}^2 + n_{0x}^2}$$
(4.15)

$$\lambda_2 = \begin{bmatrix} 1 & 0 & 0 \\ 0 & \cos \alpha & \sin \alpha \\ 0 & -\sin \alpha & \cos \alpha \end{bmatrix} \tag{4.16}$$

Where X_k , Y_k , and Z_k are the global coordinates of node k, X_i , Y_i , and Z_i are the global coordinates of node j, and α is the angle of rotation of the beam cross section with respect to the default position. Then the global stiffness matrix for a beam of 'n' elements can be assembled as:

$$K = \begin{bmatrix} k_e^g(1,j) & 0 & 0 & 0 & 0\\ 0 & \ddots & 0 & 0 & 0\\ 0 & 0 & k_e^g(i,k) + k_e^g(i+1,j) & 0 & 0\\ 0 & 0 & 0 & \ddots & 0\\ 0 & 0 & 0 & 0 & k_e^g(n,k) \end{bmatrix}$$
(4.17)

$$K = \begin{bmatrix} k_e^g(1,j) & 0 & 0 & 0 & 0 \\ 0 & \ddots & 0 & 0 & 0 & 0 \\ 0 & 0 & k_e^g(i,k) + k_e^g(i+1,j) & 0 & 0 \\ 0 & 0 & 0 & \ddots & 0 \\ 0 & 0 & 0 & 0 & k_e^g(n,k) \end{bmatrix}$$

$$M = \begin{bmatrix} m_e^g(1,j) & 0 & 0 & 0 & 0 \\ 0 & \ddots & 0 & 0 & 0 & 0 \\ 0 & \ddots & 0 & 0 & 0 & 0 \\ 0 & 0 & m_e^g(i,k) + m_e^g(i+1,j) & 0 & 0 \\ 0 & 0 & 0 & 0 & m_e^g(n,k) \end{bmatrix}$$

$$(4.17)$$

Where $k_e^g(i,j)$ and $m_e^g(i,j)$ are the stiffness and mass matrix of the node j of the element i respectively.

4.1.1. Damping

The structural damping of Equation 4.1 can be modelled using Rayleigh damping. Rayleigh damping consists of a linear combination of the structural mass and the stiffness matrix to model the structure internal damping. Rayleigh damping equation is:

$$C = \mu M + \lambda K \tag{4.19}$$

Where μ is the mass proportionality term and λ is the stiffness proportionality term. μ increases the damping in the lower frequency modes and rigid body modes, while λ increases the damping of the high frequency modes.

36 4. Structural model

4.1.2. Validation

To validate the beam model implemented in MATLAB, the cantilever beam model shown in Figure 4.2 was first compared with the analytic solution for the tip deflection. Then the first eight natural frequencies of the finite element model were compared against Ansys. The parameters of the cantilever beam model used are listed in Table 4.1 and Table 4.2.

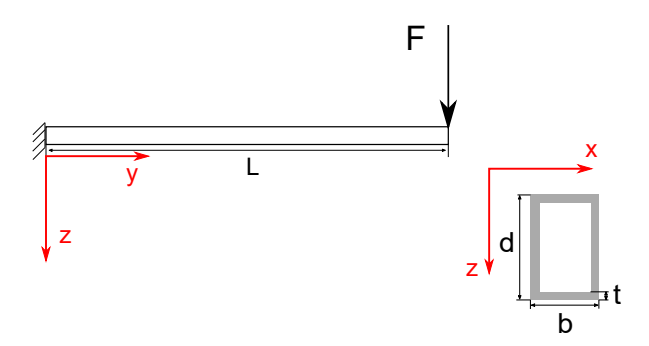


Figure 4.2: Clamped beam model for validation of finite element code

Table 4.1: Beam material properties

Properties	Value
ρ [kg/m ³]	2800
E [MPa]	70
ν [-]	0.325

Table 4.2: Beam parameters

Parameter	Value
<i>L</i> [mm]	1073.8
<i>b</i> [mm]	25.4
<i>d</i> [mm]	50.8
t [mm]	1.57
F [N/m]	100

Tip deflection validation

The tip deflection was compared between the finite element model and the analytic solution shown in Equation 4.20.

$$\delta_{tip} = \frac{FL^3}{3EI} \quad \theta_{tip} = \frac{FL^2}{2EI} \tag{4.20}$$

Where δ_{tip} is the tip deflection, θ_{tip} is the slope of the tip, F is a point load located at the tip, E is the elastic modulus, and E is the moment of inertia. In this case:

$$I = \frac{bd^3}{12} - \frac{(b-2t)(d-2t)^3}{12} = 7.6876 \cdot 10^{-8} \ [m^4]$$

As shown in Table 4.3, the tip deflection and slope angle calculated by the finite element model are the same as the analytical model.

Table 4.3: Static results

Model	δ_{tip} [mm]	θ_{tip} [rad]
Analytical	7.7	0.0107
Finite element	7.7	0.0107

Frequency validation

First, a convergence study for the first eight modes of natural frequencies was performed, with the results shown in Appendix A. It can be concluded that 15 elements is enough for the model to be considered converged.

Second, to validate the finite element model, the natural frequencies of the first eight modes for 15 elements were compared to a modal analysis using Ansys with 1712 solid elements and 3240 nodes.

4.1. Beam model 37

The mode shapes are presented in Appendix B. It can be inferred from the frequency results shown in Table 4.4 that the model has good agreement with the results shown by Ansys modal analysis and therefore, the model is validated.

Table 4.4: Model and Ansys result comparison

Mode	Model freq. [Hz]	Ansys freq. [Hz]	Error [%]
First bending x-axis	25.61	25.66	0.18
First bending z-axis	44.35	44.32	0.07
Second bending x-axis	160.50	158.53	1.24
Second bending z-axis	277.96	272.52	2.00
Third bending x-axis	449.40	434.03	3.54
First torsion	544.04	558.98	2.67
Third bending z-axis	778.32	741.54	4.96
Fourth bending x-axis	880.69	822.58	7.06

Aeroelastic model

In this chapter, the aeroelastic model using thrust condition is developed. The aerodynamic equations shown in chapter 3 and the equations of chapter 4 are coupled to get the aeroelastic model.

A scheme of the aeroelastic analysis is presented in Figure 5.1. This scheme contains an overview from the flight condition and geometry inputs to the stability results. It can be summarized in five steps:

The first step consists of the definition of the inputs of the system. In this step, the blade geometry (including the number of sections of the annular discretization), the airfoil \mathcal{C}_L and \mathcal{C}_D , the free stream flow conditions, and the propeller angular velocity need to be defined. If it is a counter-rotating system, the angular velocities of the front and rear propellers are assumed to be equal. Additionally, the beam geometry and material properties are defined for the finite element model, and the propeller inertia and nacelle properties are defined to be included in the system dynamic equations.

In the second step, the BEMT functions evaluate the conditions previously defined for the propeller. This allows the determination of the propeller axial induction factor, the tangential induction factor, and the angle of attack for every section of the discretized propeller. In the case of a counter-rotating propeller system, the solution contains the same results as the conventional or default system, but for two propellers: front and rear.

In the third step, the induction factors and angles of attack previously calculated with BEMT are used to calculate the non-steady whirl forces of the propeller. Additionally, the structural beam finite element model is defined using the beam geometry and material properties, and the system dynamic equations are calculated by using the propeller inertia properties, the propeller angular velocity, and nacelle properties.

In the fourth step, all the system equations are represented in matrix form. Therefore, the aeroelastic system is defined with respect to the different degrees of freedom to be solved afterward. Then, the whirl forces, the structural finite element model, and the system dynamic equations matrices are rearranged into a state-space representation matrix, which will allow a straightforward stability analysis.

The fifth and final step consists of the stability analysis via eigenvalue and eigenmode analysis. In this step, the eigenvalues and eigenmodes are extracted from the state-space matrix. Then, the damping coefficients and frequencies of the eigenmodes are calculated.

If a damping coefficient is negative, the system is unstable, and if all damping coefficients are positive, the system is stable. If there is a damping coefficient equal to zero while all other damping coefficients are positive, the system is critically stable.

40 5. Aeroelastic model

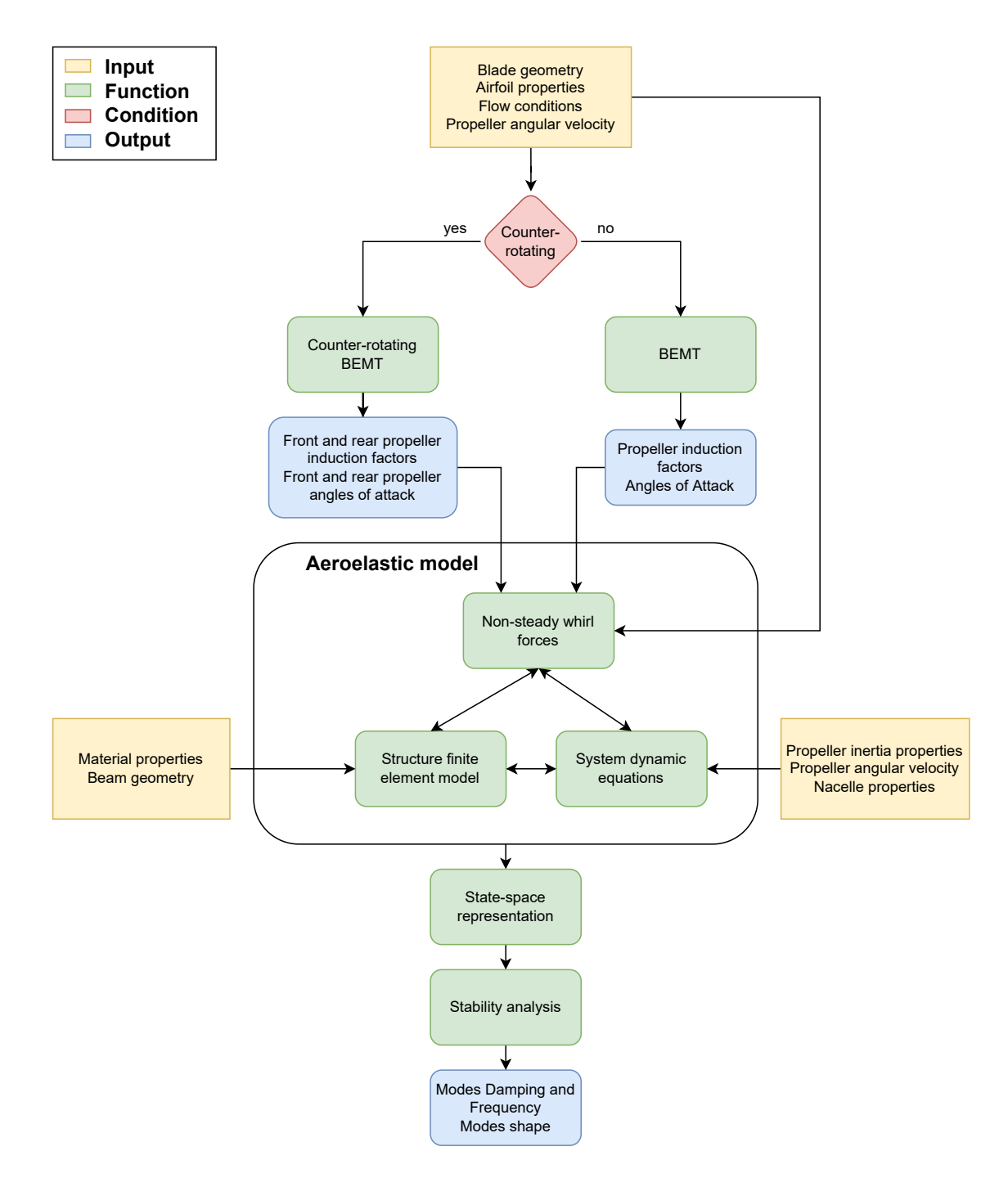


Figure 5.1: Diagram of the aeroelastic model.

The aeroelastic model developed in this section is shown in Figure 5.2. It consist of a cantilever beam model attached to a propeller-nacelle structure with two elastic degrees of freedom (θ, ψ) . The unsteady forces and moments M_y, P_y, M_z, P_z are the same as in Figure 3.9, with the axis X', Y', Z' of Figure 5.2 corresponding to the coordinate system of Figure 3.9. A more detailed view of the degrees of freedom of the propeller node is shown in Figure 5.3.

5.1. Equations of motion

The beam will be modeled as a cantilever beam with a clamped end (n_1) and the other end attached to a propeller-nacelle (n_2) . The structural beam equations were already derived in chapter 4, but as

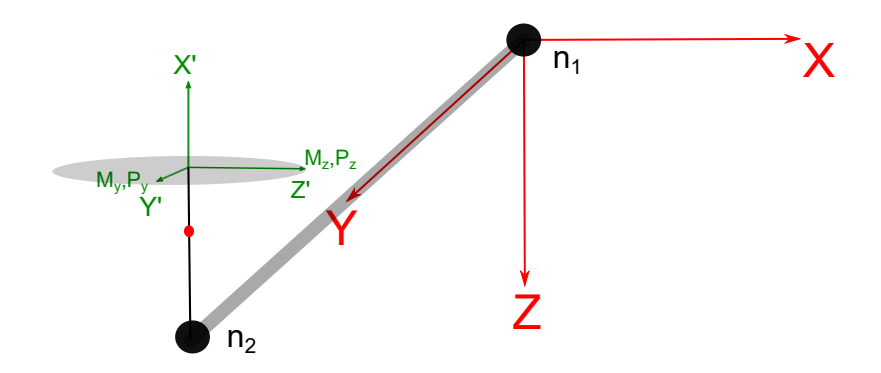


Figure 5.2: Propeller-beam system model.

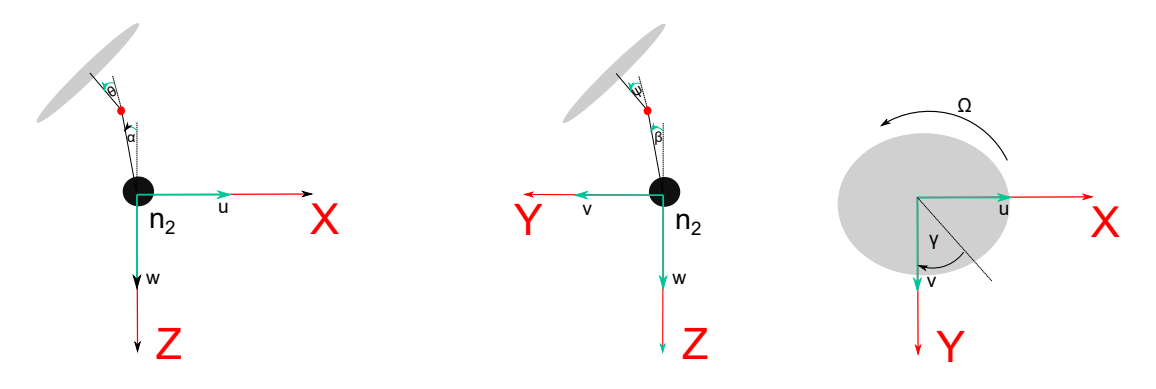


Figure 5.3: Propeller-beam system degrees of freedom.

a propeller and nacelle are added to the system, it is needed to derive the propeller-nacelle dynamic equations.

In this section, the propeller-nacelle dynamic equations are derived and then the structural dynamic equations of the beam are added. A variational calculus approach was used to derive the propeller-nacelle equations. The Euler-Lagrange equation including damping was applied for the different degrees of freedom of the system, which can be written as:

$$L = T - U$$

$$\frac{d}{dt} \left(\frac{\partial L}{\partial \dot{q}_i} \right) - \frac{\partial L}{\partial q_i} + \frac{\partial D}{\partial \dot{q}_i} = Q_i$$
(5.1)

Where T is the kinetic energy, U is the potential energy, D is the dissipation (non-conservative) energy, Q_i is the non-conservative external forces applied to the degree of freedom, and q_i is the degree of freedom.

5.1.1. Kinetic energy

The kinetic energy can be divided in two: kinetic energy of the non-rotating system and the kinetic energy of the rotating propeller. The non-rotating system is constituted by the nacelle structure and non-rotating propeller. Thus, the kinetic energy can be written as:

$$T = T_n + T_r \tag{5.2}$$

Where T_n is the kinetic energy of the non-rotating system and T_r is the kinetic energy of the rotating propeller.

42 5. Aeroelastic model

The non-rotating kinetic energy is:

$$T_n = \frac{1}{2} \int \left(\dot{u}_p^2 + \dot{v}_p^2 + \dot{w}_p^2 \right) dz \tag{5.3}$$

For a point P located at the center of the propeller the displacement u_p, v_p, w_p , considering the degrees of freedom and coordinate system of Figure 5.3, can be written as:

$$u_{p} = u + z\alpha - \theta(l_{\theta} - z)$$

$$v_{p} = v - z\beta + \psi(l_{\psi} - z)$$

$$w_{p} = w$$
(5.4)

And the velocities \dot{u}_p , \dot{v}_p , \dot{w}_p :

$$\dot{u}_{p} = \dot{u} + z\dot{\alpha} - \dot{\theta}(l_{\theta} - z)$$

$$\dot{v}_{p} = \dot{v} - z\dot{\beta} + \dot{\psi}(l_{\psi} - z)$$

$$\dot{w}_{p} = \dot{w}$$
(5.5)

Then, the non-rotating energy can be expressed as:

$$T_{n} = \frac{S_{\alpha} \dot{\alpha}^{2}}{2} + S_{\alpha,\theta} \dot{\alpha}\dot{\theta} + S_{u,\alpha} \dot{\alpha}\dot{u} \frac{S_{\beta} \dot{\beta}^{2}}{2} + S_{\beta,\psi} \dot{\beta}\dot{\psi} - S_{v,\beta} \dot{\beta}\dot{v} + \frac{S_{\psi} \dot{\psi}^{2}}{2} - S_{v,\psi} \dot{\psi}\dot{v} + \frac{S_{\theta} \dot{\theta}^{2}}{2} + S_{u,\theta} \dot{\theta}\dot{u} + \frac{M_{p} \dot{u}^{2}}{2} + \frac{M_{p} \dot{v}^{2}}{2} + \frac{M_{p} \dot{w}^{2}}{2}$$
 (5.6)

Where S_i are the inertia terms and M is the mass of the nacelle:

$$S_{\alpha} = S_{\beta} = \int z^{2}m(z)dz \qquad S_{\theta} = \int (z - l_{\theta})^{2}m(z)dz \qquad S_{\psi} = \int (z - l_{\psi})^{2}m(z)dz$$

$$S_{\alpha,\theta} = \int z(z - l_{\theta})m(z)dz \qquad S_{\beta,\psi} = \int z(z - l_{\psi})m(z)dz \qquad S_{u,\alpha} = S_{v,\beta} = \int zm(z)dz$$

$$S_{v,\psi} = \int (z - l_{\psi})m(z)dz \qquad S_{u,\theta} = \int (z - l_{\theta})m(z)dz \qquad M_{p} = \int m(z)dz$$

Where l_{θ} , l_{ψ} is the distance from node n_2 to the elastic center of the nacelle and m(z) the mass per unit length. In the case of the default configuration, these distances are negative due to the Z axis convention used in Figure 5.2.

For the rotating kinetic energy, the global propeller angular velocity, ω_t , is calculated which has a Z-axis direction, considering the coordinate system of Figure 5.2. As the nacelle is rotating due to the degrees of freedom of Figure 5.3, the kinematics of the degrees of freedom propagate towards the propeller, and thus, the effects of the propagated velocities are needed to be taken into account for ω_t . To get ω_t , the link velocity propagation equation shown in Craig [78] is used:

$${}^{i+1}\omega_{i+1} = {}^{i+1}R^i\omega_i + {}^{i}\dot{\theta}_{i+1}{}^{i+1}Z_{i+1} \tag{5.7}$$

Where i+1 is the new frame system, i is the previous frame system, ω_i is the angular velocity of the previous frame, $_i^{l+1}R$ is the rotation matrix from i to i+1, $^i\dot{\theta}_{i+1}$ is the angular velocity in the new frame, and Z_{i+1} is the direction of the angular velocity, $^i\dot{\theta}_{i+1}$, in the new frame system [78].

Using Equation 5.7, and starting from a frame located in n_2 with no angular velocity and finalizing at a frame P located in the center of the propeller, the angular velocity ω_t is derived:

$$\omega_1 = \begin{pmatrix} 0 \\ \dot{\alpha} \\ 0 \end{pmatrix} \tag{5.8}$$

$$\omega_2 = R_y(\alpha)^T \omega_1 + \dot{\beta} R_y(\alpha)^T \begin{pmatrix} 1 \\ 0 \\ 0 \end{pmatrix} = \begin{pmatrix} \dot{\beta} \\ \dot{\alpha} \\ \alpha \dot{\beta} \end{pmatrix}$$
 (5.9)

$$\omega_{3} = R_{y}(\alpha)^{T} R_{x}(\beta)^{T} R_{y}(\alpha) \omega_{2} + \dot{\beta} \begin{pmatrix} 0 \\ 1 \\ 0 \end{pmatrix} = \begin{pmatrix} \dot{\beta} (\alpha^{2} + 1) + \alpha \dot{\alpha} \beta \\ \dot{\alpha} + \dot{\theta} \\ \alpha \dot{\beta} (\alpha^{2} + 1) - \dot{\alpha} \beta \end{pmatrix}$$
(5.10)

$$\omega_{4} = R_{y}(\theta)^{T} \omega_{3} + \dot{\psi} \begin{pmatrix} 1 \\ 0 \\ 0 \end{pmatrix} = \begin{pmatrix} \dot{\psi} + \theta \left(\dot{\alpha} \beta - \alpha \dot{\beta} \left(\alpha^{2} + 1 \right) \right) + \dot{\beta} \left(\alpha^{2} + 1 \right) + \alpha \dot{\alpha} \beta \\ \dot{\alpha} + \dot{\theta} \\ \theta \left(\dot{\beta} \left(\alpha^{2} + 1 \right) + \alpha \dot{\alpha} \beta \right) - \dot{\alpha} \beta + \alpha \dot{\beta} \left(\alpha^{2} + 1 \right) \end{pmatrix}$$
(5.11)

$$\omega_{5} = R_{x}(\psi)^{T} - \Omega \begin{pmatrix} 0 \\ 0 \\ 1 \end{pmatrix} = \begin{pmatrix} \dot{\beta} + \dot{\psi} + \alpha^{2} \dot{\beta} + \alpha \dot{\alpha} \beta - \alpha \dot{\beta} \theta + \dot{\alpha} \beta \theta - \alpha^{3} \dot{\beta} \theta \\ \dot{\alpha} + \dot{\theta} + \alpha \dot{\beta} \psi - \dot{\alpha} \beta \psi + \dot{\beta} \psi \theta + \alpha^{3} \dot{\beta} \psi + \alpha^{2} \dot{\beta} \psi \theta + \alpha \dot{\alpha} \beta \psi \theta \\ \alpha \dot{\beta} - \Omega - \dot{\alpha} \beta - \dot{\alpha} \psi + \dot{\beta} \theta - \psi \dot{\theta} + \alpha^{3} \dot{\beta} + \alpha^{2} \dot{\beta} \theta + \alpha \dot{\alpha} \beta \theta \end{pmatrix}$$
(5.12)

Where R_x and R_y are the rotation matrix for the x and y axis respectively and Ω is the propeller angular velocity. Then, the total propeller angular velocity in the direction of the propeller rotation (Z-axis):

$$\omega_t = \Omega - \alpha \,\dot{\beta} + \dot{\alpha} \,\beta + \dot{\alpha} \,\psi - \dot{\beta} \,\theta + \psi \,\dot{\theta} - \alpha^3 \,\dot{\beta} - \alpha^2 \,\dot{\beta} \,\theta - \alpha \,\dot{\alpha} \,\beta \,\theta \tag{5.13}$$

Then, the rotating kinetic energy can be expressed as:

$$T_r = \frac{1}{2} S_{\Omega} \omega_t^2 \tag{5.14}$$

Where S_{Ω} is the propeller mass moment of inertia in the propeller rotation axis. Ignoring high-order terms:

$$T_r = \frac{1}{2} S_{\Omega} \left(\Omega^2 + (2\beta + 2\psi) \Omega \dot{\alpha} + (-2\alpha - 2\theta) \Omega \dot{\beta} + (2\psi) \Omega \dot{\theta} \right)$$
 (5.15)

5.1.2. Potential energy

The potential energy of the propeller-nacelle system is:

$$U = \frac{K_{\psi} \,\psi^2}{2} + \frac{K_{\theta} \,\theta^2}{2} \tag{5.16}$$

Where K_{ψ} and K_{θ} are the elastic spring constants.

5.1.3. Dissipation energy

The dissipation energy of the propeller-nacelle system considering hysteretic structural damping, which considers that the force is proportional to the velocity of the movement and inverse to the frequency of the movement, can be written as:

$$D = \frac{K_{\psi} g_{\psi} \dot{\psi}^2}{2 \omega} + \frac{K_{\theta} g_{\theta} \dot{\theta}^2}{2 \omega}$$
 (5.17)

Where ω is the vibration frequency and g_{ψ} and g_{θ} are the damping coefficients.

5.1.4. Final equations

Finally, using the Euler-Lagrange equation (Equation 5.1), the equations of motion are:

$$\begin{aligned}
\cdots + S_{u,\alpha} \ddot{\alpha} + M_p \ddot{u} + S_{u,\theta} \ddot{\theta} &= F_u \\
\cdots + M_p \ddot{v} - S_{v,\beta} \ddot{\beta} - S_{v,\psi} \ddot{\psi} &= F_v \\
\cdots + M_p \ddot{w} &= F_w \\
\cdots + S_{\beta} \ddot{\beta} + S_{\beta,\psi} \ddot{\psi} - S_{v,\beta} \ddot{v} - 2 \Omega S_{\Omega} \dot{\alpha} - \Omega S_{\Omega} \dot{\theta} &= F_{\beta} \\
\cdots + S_{\alpha} \ddot{\alpha} + S_{\alpha,\theta} \ddot{\theta} + S_{u,\alpha} \ddot{u} + 2 \Omega S_{\Omega} \dot{\beta} + \Omega S_{\Omega} \dot{\psi} &= F_{\alpha}
\end{aligned} (5.18)$$

$$S_{\alpha,\theta} \ddot{\alpha} + K_{\theta} \theta + S_{\theta} \ddot{\theta} + S_{u,\theta} \ddot{u} + \Omega S_{\Omega} \dot{\beta} + \Omega S_{\Omega} \dot{\psi} + \frac{K_{\theta} g_{\theta} \dot{\theta}}{\omega} &= F_{\theta} \\
S_{\beta,\psi} \ddot{\beta} + K_{\psi} \psi + S_{\psi} \ddot{\psi} - S_{v,\psi} \ddot{v} - \Omega S_{\Omega} \dot{\alpha} - \Omega S_{\Omega} \dot{\theta} + \frac{K_{\psi} g_{\psi} \dot{\psi}}{\omega} &= F_{\psi}
\end{aligned}$$

44 5. Aeroelastic model

Where \dots represents the beam structure's contributions to the equation of motion, which were derived in chapter 4 and F_i is the force correspondent to the degrees of freedom located where the propeller-nacelle system is attached.

5.1.5. Nodal forces

The forces of the different equations of Equation 5.18 can be obtained from Figure 5.2, in which M_y, P_y, M_z and P_z correspond to the forces derived in chapter 3. Considering $e_\beta, e_\alpha, e_\theta, e_\psi$, the distances from the center of the propeller to the pivot point of the degrees of freedom which are positive in the default configuration, the forces can be written as:

$$F_{u} = P_{z}$$
 $F_{v} = P_{y}$ $F_{w} = 0$
 $F_{\beta} = M_{z} + e_{\beta}P_{y}$ $F_{\alpha} = M_{y} - e_{\alpha}P_{z}$ $F_{\gamma} = 0$
 $F_{\theta} = M_{y} - e_{\theta}P_{z}$ $F_{\psi} = M_{z} + e_{\psi}P_{y}$ (5.19)

5.2. Matrix form

Equation 5.18 can be represented in matrix form to be later used in the state-pace representation, which correspond to the node n_2 . For other nodes of the beam finite element representation, the matrix form consists of the structural matrices derived in chapter 4. It is important to note that two new degrees of freedom ψ , θ were previously introduced for the nacelle, and thus, two new equations arise. The equation of motion can be expressed as:

$$\cdots + M_{ss}\ddot{q}_s + D_{ss}\dot{q}_s + M_{sp}\ddot{q}_p + D_{sp}\dot{q}_p = F_s$$

$$M_{ps}\ddot{q}_s + D_{ps}\dot{q}_s + K_{ps}q_s + M_{pp}\ddot{q}_p + D_{pp}\dot{q}_p + K_{pp}q_p = F_p$$
(5.20)

Where:

$$q_{s} = \begin{bmatrix} u_{n_{2}} & v_{n_{2}} & w_{n_{2}} & \beta \left(\theta_{n_{2}}\right) & \alpha \left(\phi_{n_{2}}\right) & \gamma \left(\psi_{n_{2}}\right) \end{bmatrix}^{T}$$

$$q_{p} = \begin{bmatrix} \theta & \psi \end{bmatrix}^{T}$$

To define the forces F_s and F_p of Equation 5.20, it is necessary to define the effective angles on which this forces will depend, as shown in Equation 3.73. For the system presented in Figure 5.2:

$$\overline{\theta} = \theta + \alpha - \frac{e_{\theta}\dot{\theta}}{V} - \frac{e_{\alpha}\dot{\alpha}}{V} + \frac{\dot{u}}{V}$$

$$\overline{\psi} = \psi + \beta - \frac{e_{\psi}\dot{\psi}}{V} - \frac{e_{\beta}\dot{\beta}}{V} - \frac{\dot{v}}{V}$$
(5.21)

Ignoring the second time derivatives, assumption previously validated by Kvaternik and Kohn [15] to predict whirl flutter, the derivatives of the angles can be written as:

$$\dot{\overline{\theta}} = \dot{\theta} + \dot{\alpha}
\dot{\overline{\psi}} = \dot{\psi} + \dot{\beta}$$
(5.22)

Afterward, using Equation 3.74, the aeroelastic forces of Equation 5.19 can be written in matrix form as:

$$F_{s} = D_{fss}\dot{q}_{s} + K_{fss}q_{s} + D_{fsp}\dot{q}_{p} + K_{fsp}q_{p}$$

$$F_{p} = D_{fps}\dot{q}_{s} + K_{fps}q_{s} + D_{fpp}\dot{q}_{p} + K_{fpp}q_{p}$$
(5.23)

5.3. State-space representation

To perform a stability analysis of the beam propeller system, a convenient form called state-space representation can be used. State-space representation facilitates the stability analysis by doing eigenanalysis on the linear space-state matrix. The space-state matrix can transform a linear system of second-order differential equations into a linear system of first-order differential equations. The space-state representation with a space-state matrix A is :

$$\dot{x} = Ax$$

$$x = \begin{bmatrix} x_1 & x_2 \end{bmatrix}^T$$

$$x_1 = \dot{x}_2$$

$$A = \begin{bmatrix} M & 0 \\ 0 & I \end{bmatrix}^{-1} \begin{bmatrix} -D & -K \\ I & 0 \end{bmatrix}$$
(5.24)

Where x_2 corresponds to the system degrees of freedom, M is the aeroelastic system mass matrix, D is the aeroelastic damping matrix, K is the aeroelastic stiffness matrix, and D is the identity matrix. For the aeroelastic model previously presented, the equivalent state-space matrix is:

46 5. Aeroelastic model

$$x_{2} = \begin{bmatrix} u_{1} & v_{1} & w_{1} & \theta_{1} & \phi_{1} & \psi_{1} & \dots & u_{n_{2}} & v_{n_{2}} & w_{n_{2}} & \theta_{n_{2}} & \psi_{n_{2}} \end{bmatrix}$$

$$M = \dots + M_{ss} + M_{sp} + M_{ps} + M_{pp}$$

$$D = \dots + D_{ss} + D_{sp} + D_{ps} + D_{pp} - (D_{fss} + D_{fsp} + D_{fps} + D_{fpp})$$

$$K = \dots + K_{ps} + K_{pp} - (K_{fss} + K_{fsp} + K_{fps} + K_{fpp})$$

$$(5.25)$$

5.3.1. Counter-rotating configuration

In the case of a counter-rotating configuration, the aeroelastic system consist of the equations previously developed, but also adding the counter-rotating propeller equations of motion and forces. Therefore:

$$EOM: F_d + F_c = EOM_d + EOM_c (5.26)$$

Where EOM are the equations of motion (Equation 5.18), F is the aerodynamic whirl forces and d, c are the default (front propeller) and counter-rotating propeller (rear propeller) respectively.

For the rear propeller, rotating clockwise, the equation of motion changes because of the geometry and angular velocity direction. These changes can be summarized by the following:

- $\Omega = -\Omega$ because the propeller is rotating clockwise.
- l_{θ} , l_{η} , are positive in pusher configuration.
- e_{β} , e_{α} , e_{θ} , e_{ψ} are negative in pusher configuration.

5.4. Stability analysis

To analyze the stability of the aeroelastic system, an eigenanalysis is performed in the state-space matrix A. The eigenanalysis consists of the inspection of the eigenvalues and eigenmodes of the matrix. For a matrix A with dimensions NxN, N eigenvalues can be found with the corresponding eigenmode. As A is the space-state representation of an aeroelastic system, it can be expected that the eigenvalues and eigenmodes are complex numbers, due to the aeroelastic damping. To find the eigenvalues and eigenmodes, the following equations need to be solved:

$$Av_i = \lambda_i v_i \tag{5.27}$$

Where A is the state-space matrix, λ_i is the eigenvalue, I the identity matrix, and v_i are the eigenmodes. There are two important parameters that can be extracted from the eigenvalues that will give insight on the stability of the system eigenmodes: the damping coefficient and the frequency. The damping coefficient, sometimes called damping ratio, can be defined as:

$$\zeta_i = \frac{-\Re(\lambda_i)}{|\lambda_i|} \tag{5.28}$$

Where $\Re(\lambda_i)$ is the real part of the eigenvalue, and $|\lambda_i|$ is the norm of the complex number. If the eigenvalue is real, the frequency is zero. In the case of a complex eigenvalue, the frequency can be obtained as:

$$\omega_i = |\lambda_i| \tag{5.29}$$

Then, the stability analysis can be performed. The stability criteria are:

$$\begin{aligned} \zeta_i &> 0 \text{ Stable} \\ \zeta_i &= 0 \text{ Critically Stable} \\ \zeta_i &< 0 \text{ Unstable} \end{aligned} \tag{5.30}$$

If an eigenmode is unstable and the eigenvalue is a real number, then divergence occurs. However, if the an eigenmode is unstable and the eigenvalue is a complex number, then flutter occurs.

It is important to add that the eigenvalue solvers do not guarantee order of the solutions. Thus, to track the eigenvalues for different flight conditions, the Modal Assurance Criterion (MAC) can be used.

5.4.1. Mode tracking

To track the aeroelastic modes, the Modal Assurance Criterion is a statistical tool that permits the comparison between vectors by giving a number between 0 and 1, in which 1 means that the vectors are identical, while 0 means that the vectors are orthogonal and therefore, not related. The MAC equation for the two vectors v_1 and v_2 is:

$$MAC(v_1, v_2) = \frac{|v_1^T v_2^*|^2}{|v_1^T v_1^*| |v_2^T v_2^*|}$$
(5.31)

With v_i^* the vector complex conjugate.



Analysis and results

6.1. Octocopter Parameters

An octocopter designed and manufactured by Betronka SPA was analyzed for aeroelastic stability. The model developed in the previous chapters consists of a clamped beam model with a propeller attached to the tip, as shown in Figure 6.1 for the default configuration or Figure 6.2 in the case of counter-rotating propellers.

Additionally, Betronka SPA provided the dimensions of the octocopter frame used for the whirl flutter analysis, shown in Figure 6.3, the frame material properties and geometry listed on Table 6.1 and Table 6.2, the motor nacelle mass and height listed on Table 6.3, the propeller characteristics tabulated on Table 6.4, the blade geometry tabulated on Table 6.5, the blade CAD model, and the blade lift coefficient \mathcal{C}_L and blade drag coefficient \mathcal{C}_D , shown in Figure 6.4 and Figure 6.5.

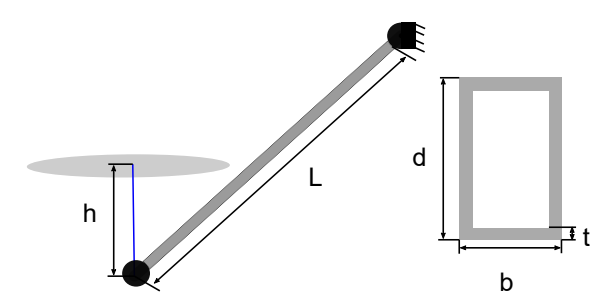


Figure 6.1: Simplified model geometry.

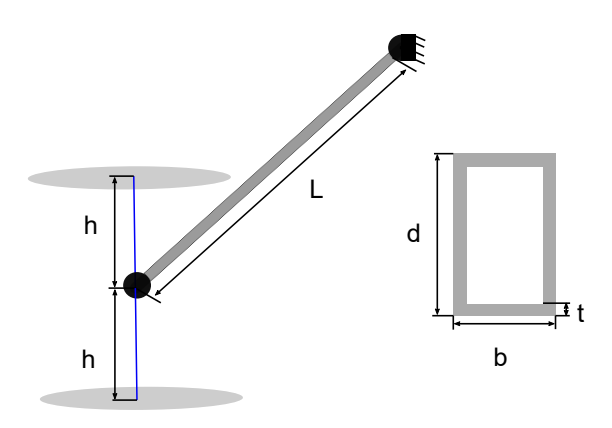


Figure 6.2: Simplified model geometry for the counter-rotating configuration.

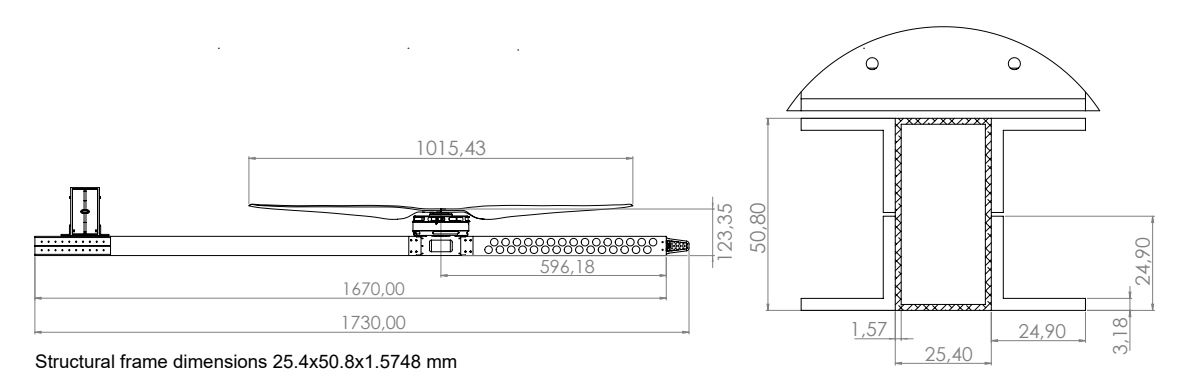


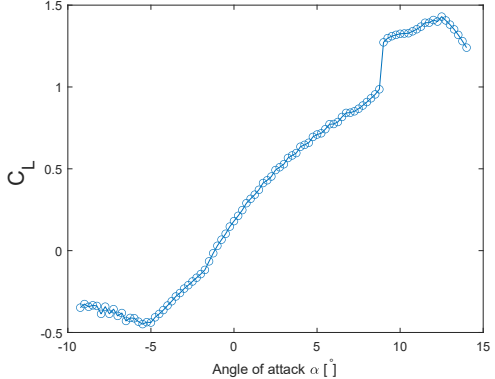
Figure 6.3: Octocopter beam geometry.

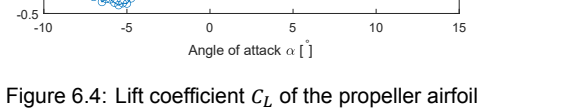
Table 6.1: Aluminum 7075-T6 properties

Properties	Value
ρ [kg/m ³]	2800
E [MPa]	70
ν [-]	0.325

Table 6.2: Beam parameters of Figure 6.1

Parameter	Value
L [mm]	1073.8
<i>b</i> [mm]	25.4
<i>d</i> [mm]	50.8
t [mm]	1.57
Number of elements	15





0.11 0.11 0.09 0.08 0.07 0.06 0.05 0.04 0.03 -10 -5 0 5 10 1ε Angle of attack α[]

Figure 6.5: Drag coefficient C_D of the propeller airfoil

The following assumptions were made for the multirotor stability analysis:

- · The beam material is considered isotropic.
- The nacelle is comprised of a propeller shaft and motor. These components are considered to be rigid in comparison to the beam, and thus, the nacelle degrees of freedom θ , ψ are neglected for this analysis.
- The nacelle moments of inertia are calculated as a solid cylinder of constant density. Then, the moment of inertia are:

$$S_{\alpha} = S_{\beta} = S_{\alpha,\beta} = \frac{mh^2}{3}$$
 $S_{u,\alpha} = S_{v,\beta} = -\frac{mh}{2}$

Where m is the mass and h is the height of the cylinder.

 The propellers are considered rigid, an assumption made due to the smaller dimensions of the propeller compared to fixed-wing aircraft propellers, which are also considered rigid in the whirl flutter studies, as mentioned in chapter 2.

Table 6.3: Nacelle properties

Parameter	Value
<i>M</i> [kg]	1.5
S_{α} [kg m ²]	0.0048
$S_{u,\alpha}$ [kg m]	-0.07345
h [mm]	97.95

Table 6.4: Propeller properties

Parameter	Value
Number of Blades	2
<i>M</i> [kg]	0.3
S_{Ω} [kg m ²]	0.0306
R_{hub} [mm]	72
R_{tip} [mm]	479
Max thrust [N]	340
Max Ω [RPM]	5000

Table 6.5: Blade geometry

r/R_{tip}	Chord length	Geometric angle
[-]	c [mm]	β [°]
0.17	7.34	20.57
0.21	8.41	21.40
0.26	9.16	19.87
0.30	9.58	17.58
0.34	9.75	16.03
0.38	9.73	14.94
0.43	9.56	13.80
0.47	9.33	12.82
0.51	9.08	12.01
0.55	8.77	11.29
0.60	8.43	10.71
0.64	8.02	9.98
0.68	7.57	9.55
0.73	7.10	8.94
0.77	6.63	8.38
0.81	6.15	8.15
0.85	5.67	7.96
0.90	5.17	7.52
0.94	4.62	7.14
0.98	3.75	6.90

- The propeller is considered to work only in thrusting and windmilling conditions.
- There is no aerodynamic interaction between adjacent propellers as BEMT and the perturbation model for the whirl forces do not account for the aerodynamic interactions between the adjacent propellers. The study of this interaction is out of the scope of this thesis.
- The aerodynamic interference between propellers and the beam structure is not considered, as the BEMT and the perturbation model do not account for the interference of the beam structure on the propeller aerodynamics.
- An air density $\rho = 1.22 \text{ kg/m}^3$ and viscosity $\mu = 1.81E 5 \text{ kg/m} \text{ s}$ were used.
- As all the structures have material damping. The results are shown for a beam with Rayleigh damping (Equation 4.19) with $\mu=0$ and $\lambda=0.0005$. These low values were adopted to be conservative and only affect the structural modes with high frequencies.

6.1.1. Propeller conditions for the multirotor designed flight conditions

The BEMT model and the whirl forces model used assume that the free stream flow has a perpendicular direction to the propeller plane of rotation. Therefore, just two variables are independent: the magnitude of the free stream flow velocity and the propeller angular velocity.

As previously mentioned, only thrust and windmilling conditions are going to be evaluated. For this reason, it is necessary to evaluate the combination of flow velocities and propeller angular velocities

that correspond to thrust or windmilling conditions. A way to know that the propeller is operating in thrust conditions is by using BEMT to get the thrust coefficient C_T . When $C_T > 0$, the propeller is operating in thrust conditions and for $C_T = 0$, the propeller is operating in windmilling conditions.

For a specific propeller, C_T is a function of the advance ratio J and the flow properties. Therefore, the advance ratio will be used to determine the propeller thrust conditions. The C_T diagram against advance ratio J for the propeller used in the octocopter is presented in Figure 6.6. For advance ratios lower than approximately 0.38, the propeller is working in thrusting conditions, and with J=0.38, the propeller can be considered to be working in windmilling conditions.

Additionally, as listed on Table 6.4, the propeller maximum thrust is 340 N, which occurs at the maximum propeller angular speed of 5000 RPM, and the thrust coefficient can be written as:

$$C_T = \frac{T}{\rho n^2 D^4} \tag{6.1}$$

Where T is the propeller thrust, ρ is the flow density, n is the propeller angular speed, and D is the propeller diameter. Then, using Equation 6.1 the maximum propeller thrust of 340 N is obtained for $C_T = 0.047$, which corresponds with J = 0.12. As the propeller cannot produce more thrust than 340 N, for this study the minimum advance ratio is limited to J = 0.12.

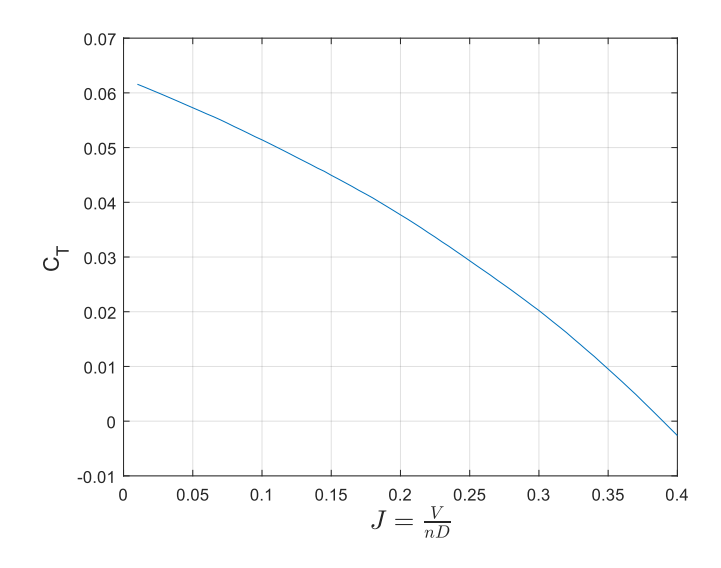


Figure 6.6: Thrust coefficient C_T against propeller advance ratio J

Finally, the propeller conditions for the multirotor flight conditions can be summarized as a propeller angular speed, Ω , between 0-5000 RPM and an advance ratio, J, between 0.12-0.38. Using the advance ratio equation (Equation 3.28), the inflow velocity for the for the multirotor flight conditions can be calculated.

6.2. Results and discussion

6.2.1. Whirl flutter analysis for the multirotor flight conditions

In this section, the results of the whirl flutter analysis for the multirotor flight conditions previously introduced are presented. These conditions consist of advance ratios, *J*, between 0.12-0.38 and propeller angular speeds lower or equal to 5000 RPM.

All the aeroelastic modes were analyzed for whirl flutter. The stability analysis explained in section 5.4 shows that all the aeroelastic modes had a positive damping coefficient for the designed flight conditions, and it can be concluded that the multirotor designed by Betronka SPA does not suffer from whirl flutter. The modes with the lowest damping coefficient are shown next for further analysis.

The damping and frequency diagrams for the first lowest damping mode, which is the x-axis first bending mode of the conventional configuration are shown in Figure 6.7 and Figure 6.8, and for the counter- rotating configuration are shown in Figure 6.9 and Figure 6.10. The damping and frequency

diagrams for the second lowest damping mode, which is the z-axis first bending mode of the conventional configuration are shown in Figure 6.11 and Figure 6.12, and Figure 6.13 and Figure 6.14 for the counter-rotating configuration.

From Figure 6.7, Figure 6.9, Figure 6.11, and Figure 6.13, it can be inferred that the inflow velocity does not significantly change the damping coefficient for a constant angular velocity. Therefore, the thrust conditions, considering the octocopter flight conditions, do not have a big impact on the system stability. This behavior is similar to the case of fixed-wing aircraft with lightly loaded propellers, where thrust is negligible [5].

By comparing the default configuration frequencies, shown in Figure 6.8 and Figure 6.12, to the counter-rotating configuration frequencies, shown in Figure 6.10 and Figure 6.14, it can be seen that both bending modes of the counter-rotating configuration have lower frequencies compared to the default configuration, which could be explained by the increase of the moment of inertia because of the addition of a motor, shaft and propeller.

To improve the understanding of the whirl flutter phenomena in the multirotor, the next sections analyze conditions outside the designed flight conditions.

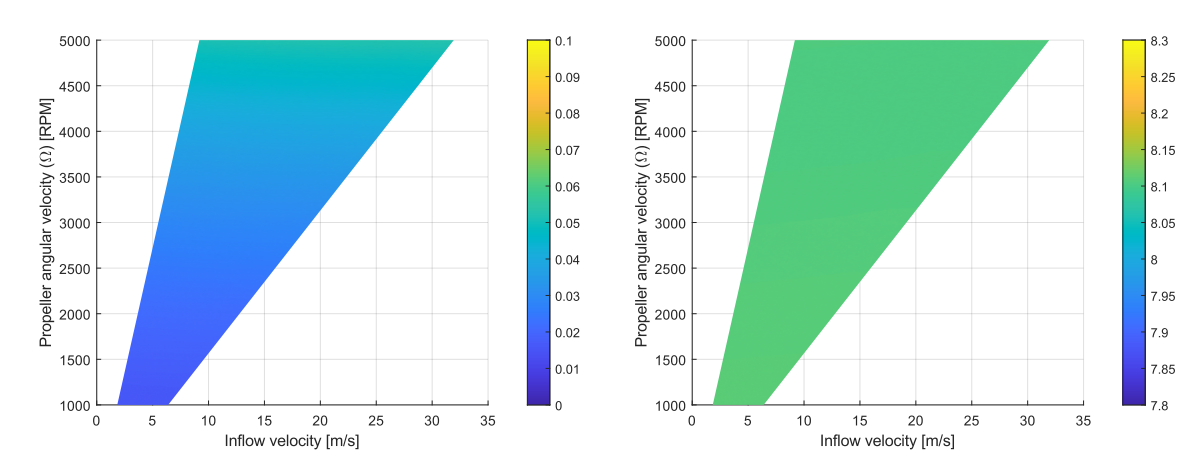


Figure 6.7: First bending x-axis damping coefficient for default propeller configuration

Figure 6.8: First bending x-axis frequency for the default propeller configuration

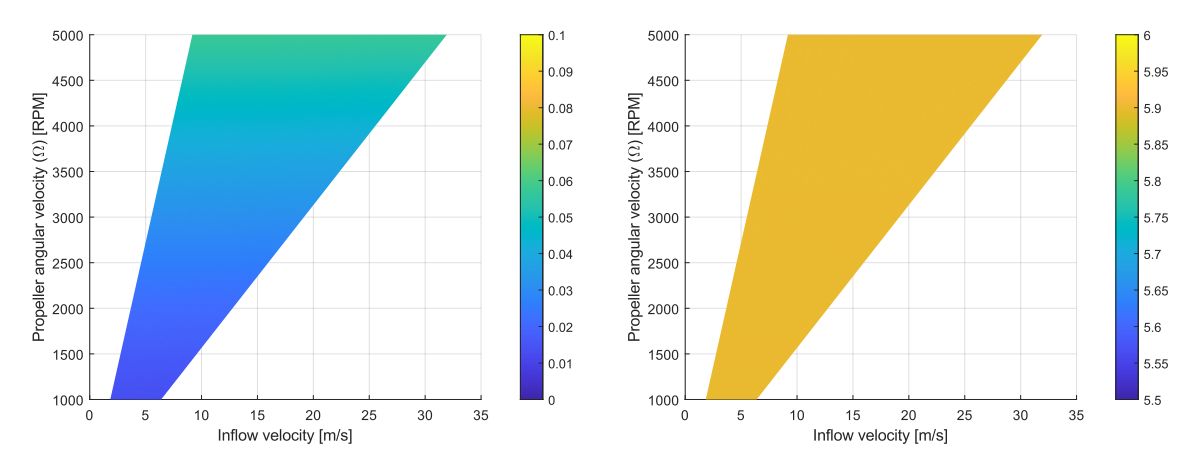


Figure 6.9: First bending x-axis damping coefficient for the counter-rotating propeller configuration

Figure 6.10: First bending x-axis mode frequency for the counter-rotating propeller configuration

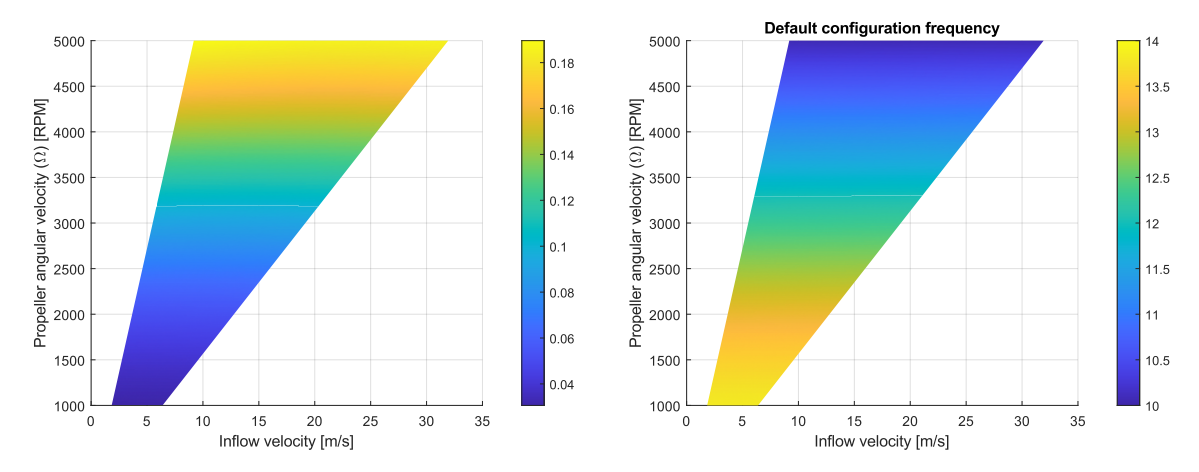


Figure 6.11: First bending z-axis mode damping coefficient for the default propeller configuration

Figure 6.12: First bending z-axis frequency for the default propeller configuration

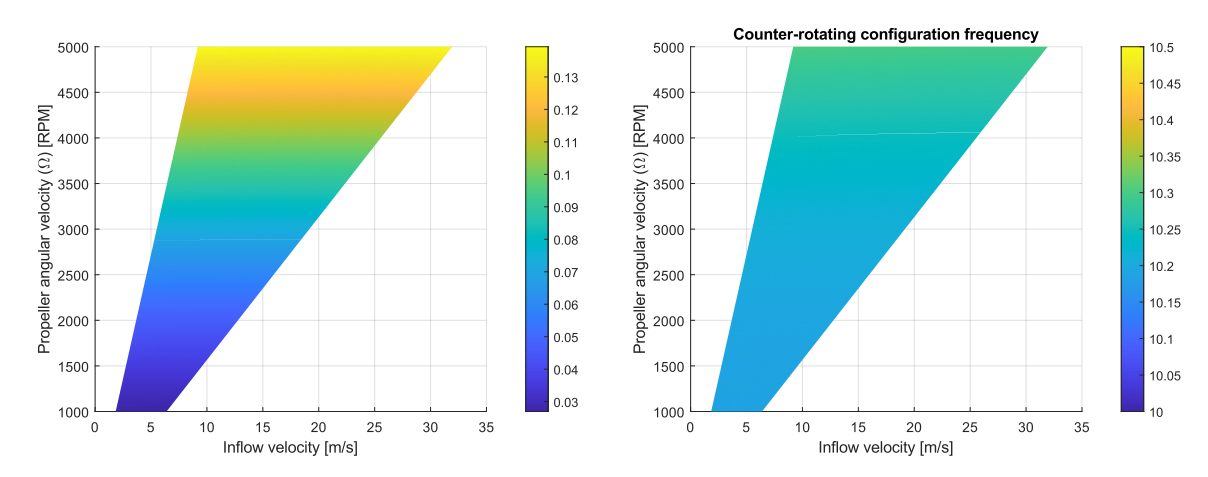


Figure 6.13: First bending z-axis damping coefficient for the counter-rotating propeller configuration

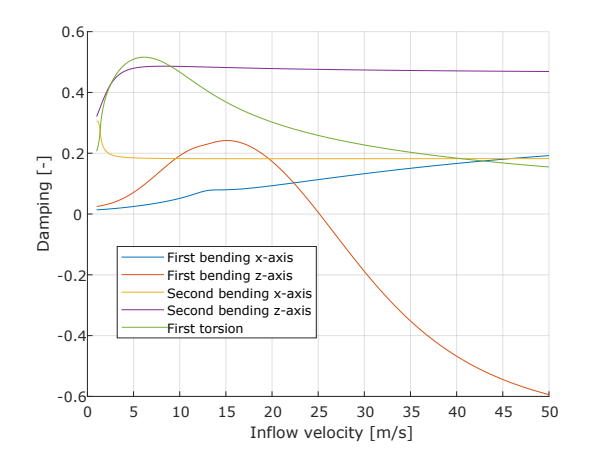
Figure 6.14: First bending z-axis frequency for the counter-rotating propeller configuration

6.2.2. Modal analysis with respect to the inflow velocity

To better understand the stability analysis, it is necessary to evaluate whirl flutter in a wider range of velocities, without the octocopter flight condition restrictions. By increasing the range of studied velocities, whirl flutter can be encountered by the system, and trends can be shown for the stability analysis.

The results shown in Figure 6.15 and Figure 6.16 correspond to the damping and frequency diagram for five modes with J=0.12 for a default configuration. The five modes correspond to the x-axis first bending, z-axis first bending, x-axis second bending, z-axis second bending, and first torsion. The only mode that can be unstable is the first bending of the z-axis, which will reach flutter at a inflow velocity of $25\ m/s$. At the flutter speed, this aeroelastic mode is mainly comprised of z- axis first bending and y-axis first bending, as shown in Figure 6.17. The frequency of this mode is the lowest of the of the system at the flutter speed at around 5 Hz.

It is important to mention that when the frequencies of the first bending modes cross in Figure 6.16, a small interaction occurs between the modes, which can be seen in Figure 6.15. This interaction disappears again when the frequencies of the mode start to distance from each other.



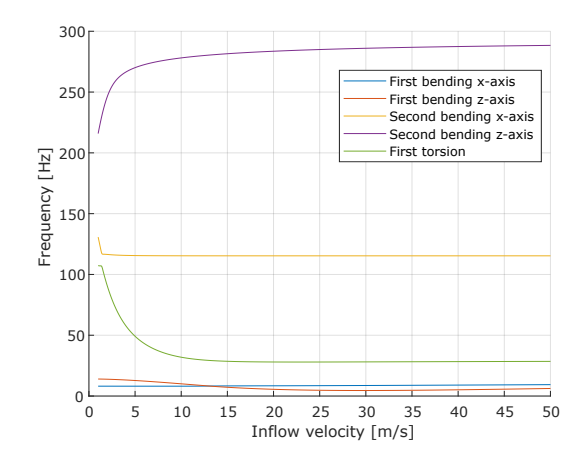


Figure 6.15: Damping coefficient for constant advance ratio J = 0.12 and variable inflow velocity for a default propeller configuration

Figure 6.16: Frequency for constant advance ratio J=0.12 and variable inflow velocity for a default propeller configuration

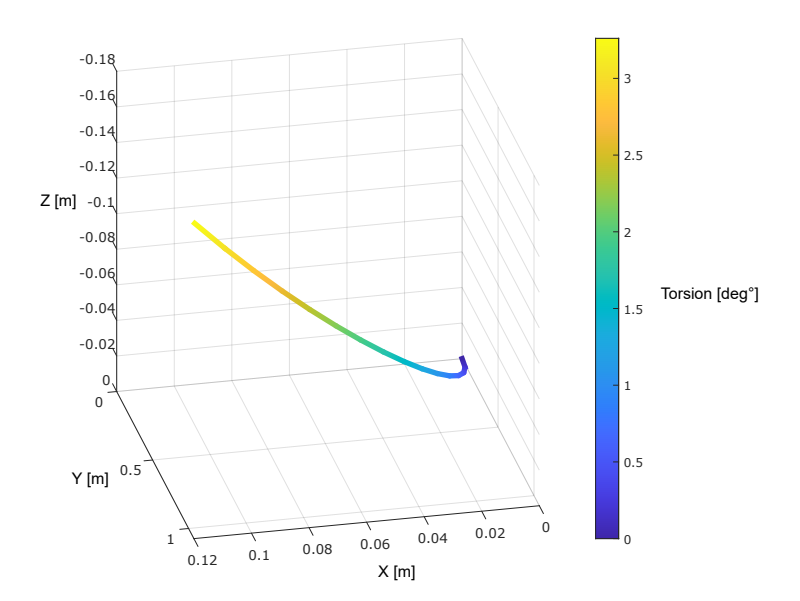
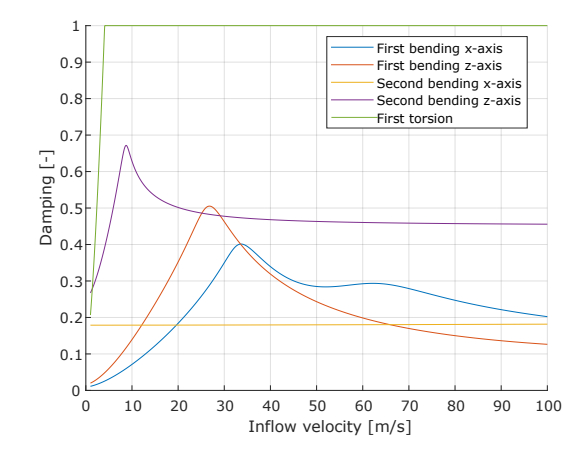


Figure 6.17: Mode shape of the unstable mode at the flutter speed.

In the case of the counter-rotating configuration, the damping and frequency diagram are shown in Figure 6.18 and Figure 6.19. These diagrams show the following modes: the x-axis first bending, z-axis first bending, x-axis second bending, z-axis second bending, and first torsion. As shown Figure 6.18, the counter-rotating configuration is more stable and did not suffer from flutter for velocities below $100\ m/s$. Also, it can be concluded from Figure 6.18 and Figure 6.19, that the torsion mode is overdamped, and therefore, the eigenvalue is a real negative number. Also, it can be seen in Figure 6.19 that in the counter-rotating configuration, the z-axis bending mode always has a higher frequency than the x-axis first bending mode, which is not the case for the default configuration.



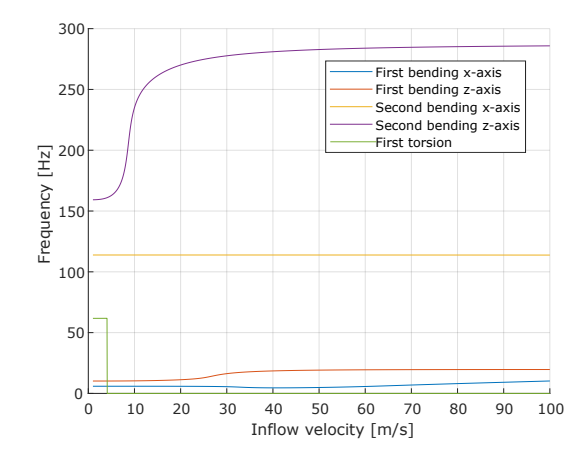


Figure 6.18: Damping coefficient for constant advance ratio J = 0.12 and variable inflow velocity for a counter-rotating propeller configuration

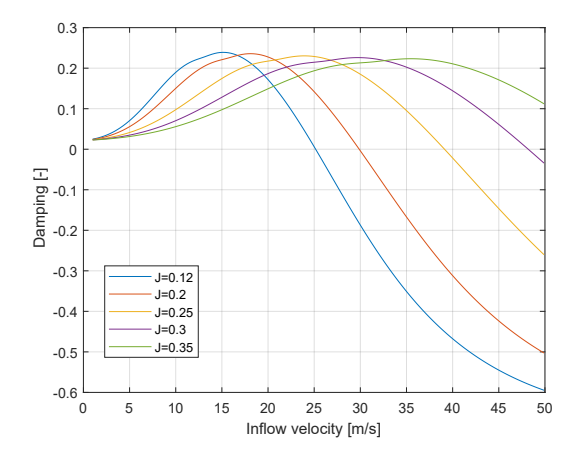
Figure 6.19: Frequency for constant advance ratio J = 0.12 and variable inflow velocity for a counter-rotating propeller configuration

6.2.3. Influence of different advance ratios considering variable inflow velocity

To understand the influence of the thrusting conditions on the stability analysis, advance ratios from high thrust conditions (J=0.12) to low thrust conditions (J=0.35) were assessed. The only mode that can reach whirl flutter is the z-axis first bending mode, therefore, in this section only the z-axis first bending mode will be analyzed.

The damping and frequency for different advance ratios of the z-axis first bending mode for the default configuration are shown in Figure 6.20 and Figure 6.21, and for the counter-rotating configuration are shown in Figure 6.22 and Figure 6.23. From Figs. 6.20–6.23 it can be inferred that increasing the thrust of the propeller decreases the damping of the z-axis first bending mode for a particular inflow velocity, decreasing the stability of the system for both configurations. For the default configuration, the whirl flutter speed can vary from $25\ m/s$, corresponding to high thrust conditions with J=0.12, to flutter speeds above $50\ m/s$, for propeller flow conditions close to windmilling with J=0.35. It can also be deducted that the counter-rotating configuration is always more stable than the default configuration, which can be attributed to the opposition between the whirl moments of the clockwise propeller and the counterclockwise propeller.

It is important to add that the studied multirotor uses fixed-pitch propellers. Therefore, by comparing different advance ratios for a variable inflow velocity, the angular speed of the propeller will also be proportional to the inflow velocity, as it can be inferred from Equation 3.28. This means that for a particular inflow velocity, increasing the advance ratio will decrease the propeller angular velocity. Then, the significant increase in whirl flutter speed for decreasing thrust condition, shown in Figure 6.20 and Figure 6.22, is highly influenced by the propeller angular speed Ω and not necessarily by the thrust condition itself. This statement is supported by the fact that the unsteady aerodynamic forces produced by the propeller gyroscopic motion, derived in subsection 3.2.2, depend directly on Ω .



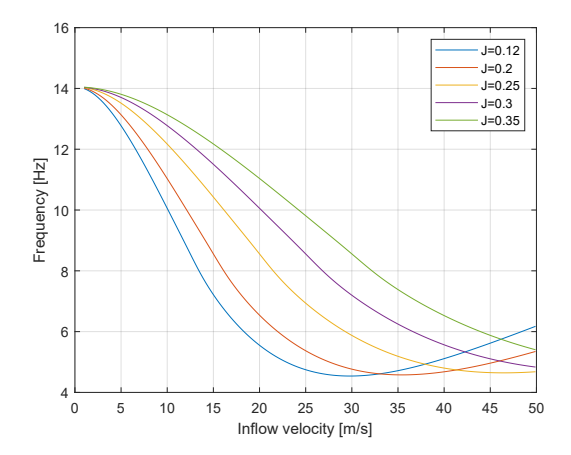
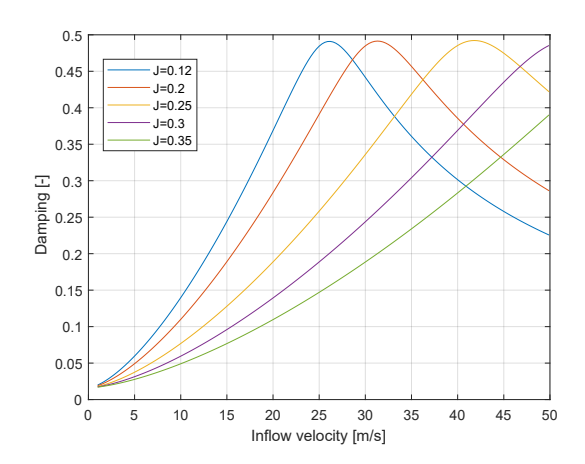
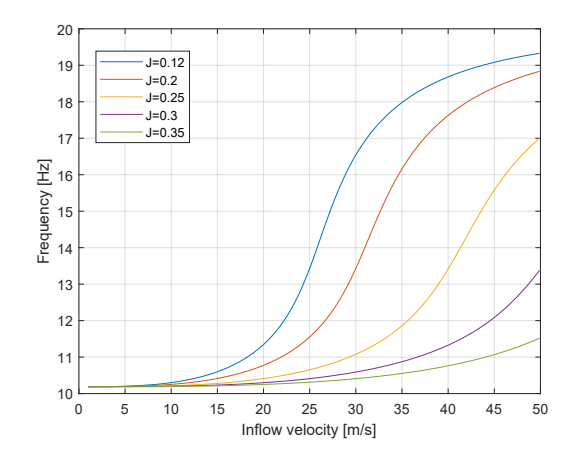


Figure 6.20: First bending z-axis mode damping coefficient for Figure 6.21: First bending z-axis mode frequency for different different advance ratios J and variable inflow velocity a default advance ratios J and variable inflow velocity a default propeller propeller configuration configuration





different advance ratios J and variable inflow velocity for a counter-rotating propeller configuration

Figure 6.22: First bending z-axis mode damping coefficient for Figure 6.23: First bending z-axis mode frequency for different advance ratios J and variable inflow velocity for a counter-rotating propeller configuration

6.2.4. Influence of different advance ratios considering variable propeller angular velocity

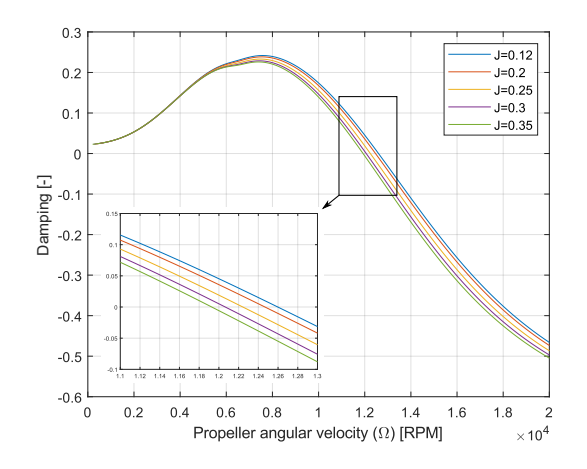
Another way of showing the thrust influence on the system stability is to analyze the damping and frequency of the aeroelastic modes for different constant advance ratios I, while varying the propeller angular velocity. By using constant advance ratios and variable propeller angular speed, the thrust condition of the propeller will remain constant, and it can give a better understanding about the influence of the thrust conditions on the system. The analysis will focus on the z-axis first bending mode as is the only mode that was found unstable on the evaluated conditions.

It can be inferred from Figs. 6.24–6.27 that the z-axis first bending mode damping coefficient and frequency of the default and counter-rotating configuration is highly dependent on the angular velocity of the propeller.

Figure 6.24 shows that for a default configuration, the advance ratio increases the damping of the z-axis first bending mode for a particular propeller angular speed. Therefore, the thrust conditions have a stabilizing effect on the system, which also translates to an increase of the whirl flutter speed. For the default configuration, the high thrust conditions increase the propeller angular velocity of the whirl flutter boundary by approximately 4% in comparison to the low thrust conditions.

It can be concluded that for a default configuration, using windmilling conditions leads to conservative whirl flutter boundaries. On the contrary, for the counter-rotating configuration, thrust has a negligible destabilizing effect, as can be seen in Figure 6.26, even considering high thrust conditions.

With respect to the flutter frequencies, as shown in Figure 6.25, in the case of the default configuration, thrust conditions tend to decrease the first bending z-axis mode flutter frequency. On the other hand, Figure 6.27 shows that for a counter-rotating configuration, thrust conditions have a negligible effect on the first bending z-axis mode frequency.



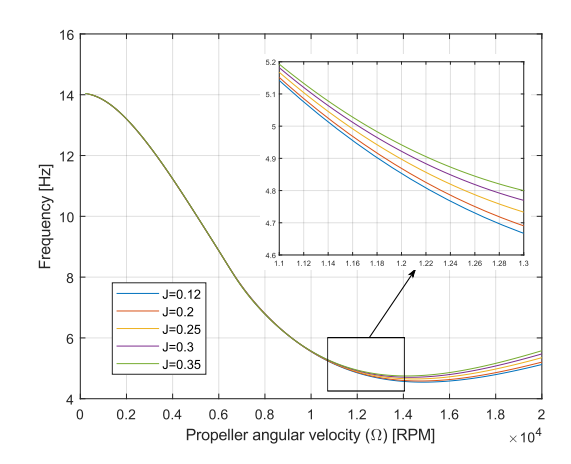
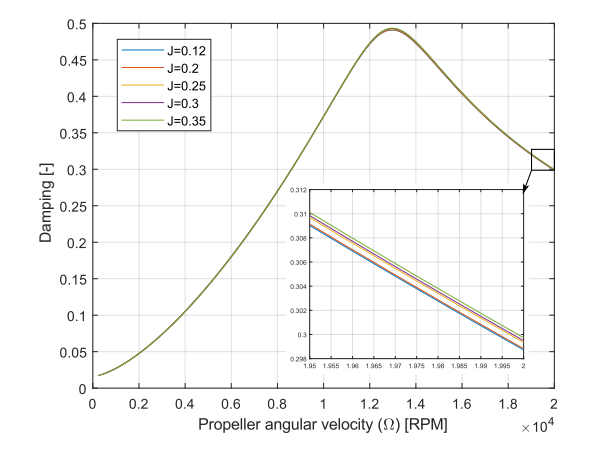


Figure 6.24: First bending z-axis mode damping coefficient for different advance ratios J and variable propeller angular velocity for a default propeller configuration

Figure 6.25: First bending z-axis mode frequency for different advance ratios J and variable propeller angular velocity for a default propeller configuration



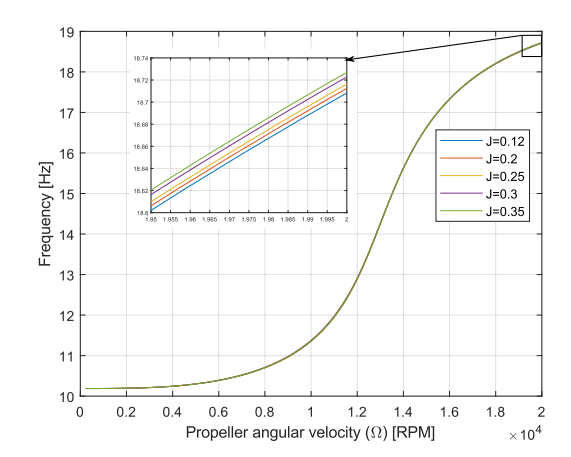


Figure 6.26: First bending z-axis mode damping coefficient for Figure 6.27: First bending z-axis mode frequency for different different advance ratios J and variable propeller angular velocity for a counter-rotating propeller configuration

advance ratios J and variable propeller angular velocity for a counter-rotating propeller configuration

 $\overline{}$

Conclusions

In the current work, a semi-analytic aeroelastic model was developed and implemented on MATLAB to predict the whirl flutter of a multirotor configuration in thrusting conditions. The model consists of a cantilever beam with a propeller-nacelle system attached to the free end. Two configurations were successfully evaluated for whirl flutter: a default configuration with one propeller at the free end of the beam, and a counter-rotating configuration with two propellers at the free end of the beam.

The propeller aerodynamics in thrusting conditions were modeled using BEMT, then the flow conditions in the propeller disk calculated with BEMT were coupled to a linear perturbation model to calculate the unsteady aerodynamic forces produced by the gyroscopic motion, which are the forces responsible for causing whirl flutter. Next, the propeller-nacelle equations of motion, the finite element beam structure equations of motion, and the propeller unsteady aerodynamic forces produced by the gyroscopic motion were coupled into the aeroelastic model in state-space form. For the default configuration, the different parts of the aeroelastic model were validated: The blade element momentum theory, the unsteady aerodynamic forces produced by the gyroscopic motion, and the beam finite element model.

After the development, the aeroelastic model was used to perform a stability analysis and predict whirl flutter in a multirotor designed by Betronka SPA. Whirl flutter was assessed for the multirotor designed flight conditions, considering the propeller in thrust and windmilling conditions. Later, whirl flutter was evaluated for propeller conditions above the designed limits, to further investigate the whirl flutter phenomena.

The main findings of this thesis can be summarized as follows:

- The multirotor manufactured by Betronka SPA does not reach whirl flutter speeds for all the designed flight conditions. At these conditions, increasing the propeller speed increases the aerodynamic damping of the z-axis first bending, which increases the stability of the system, as it is the first mode to be unstable.
- The counter-rotating configuration tends to be more stable than the conventional propeller configuration. The aerodynamic damping significantly increases by using the counter-rotating configuration. This stabilizing effect of the counter-rotating configuration can be caused by the propeller's torque direction opposition, which reduces the overall unsteady forces perceived by the structure, as one propeller torque component opposes the other.
- Thrust conditions have a stabilizing effect for the default configuration. For the multirotor designed by Betronka, it was found that high thrust conditions increased the propeller angular velocity of the whirl flutter boundary by 4% compared to flow conditions close to windmilling. Therefore, using windmilling conditions to assess whirl flutter on the multirotor will lead to a conservative whirl flutter speed boundary.
- For a counter-rotating configuration, thrust conditions have a negligible effect on the whirl flutter boundary and the system aerodynamic damping. This observation suggests that windmilling conditions can be used to assess whirl flutter in the case of two rigid counter-rotating propellers.

60 7. Conclusions

• For the model studied, the thrust conditions significantly decrease the whirl flutter boundary for inflow velocity. This occurs because close to the whirl flutter boundary, the z-axis first bending mode damping decreases with increasing propeller angular velocity. And as the multirotor propeller is a fixed-pitch propeller, increasing the thrust condition will increase the angular velocity of the propeller for a particular inflow velocity. Therefore, increasing the thrust will lead to a decrease in the z-axis first bending mode damping at a particular inflow velocity, decreasing the whirl flutter boundary for inflow velocity.

- It was found that in the case of the studied rigid and fixed-pitch propeller, the rotational symmetry approximation could be used even though the propeller had only two blades. This finding simplifies the aeroelastic stability analysis of rigid 2 blades propellers as there is no explicit time dependence on the unsteady aerodynamic forces produced by the gyroscopic motion when using the rotational symmetry approximation, allowing the use of eigenvalue and eigenmode analysis directly.
- The use of BEMT to capture the thrust conditions, the use of an analytical perturbation model for the unsteady forces produced by the propeller gyroscopic motion, and the use of a beam element finite element model kept low-computational costs in the aeroelastic stability analysis. This makes the developed model a good candidate to be applied in the preliminary design stages of multirotor aircraft.

Future work

As the model is theoretical and only the subsystems of the default configuration were validated with experimental data obtained from the literature, the validation of the coupled system and experimental research on whirl flutter using thrusting conditions are left for future research. The main recommendations for future research are:

- Future research should include the wake effects in the unsteady whirl forces model using thrust conditions, as the aerodynamic stability derivatives significantly depend on the lag effect produced by the wake.
- An experimental validation of the unsteady whirl forces for thrust conditions should be carried out.
- · Validation of the counter-rotating BEMT is recommended to evaluate the accuracy of the model.
- After the validation of the BEMT, an experimental validation of counter-rotating whirl flutter model should be investigated.
- An experimental study of the whirl flutter boundaries using thrust conditions should be carried out considering a structural beam with a propeller at the tip to validate the model developed on this thesis.
- Flight dynamics of the multirotor coupled with the aeroelastic model should be studied to assess the interaction between the different propeller-beam structures.
- In the current model, the flow was always considered to be perpendicular to the propeller plane of rotation. For future research it is recommended to also include angle dependent flow conditions for the propeller aerodynamics, due to the characteristics of multirotor flight types.
- A comparison of the time response using different 2-bladed propellers to further validate that rotational symmetry can be applied in general cases of rigid propellers should be completed.



Finite element frequency convergence study

In this appendix, the convergence study for the first 8 modes of the cantilever beam used in subsection 4.1.2 is presented. It can be inferred that 15 elements is enough to have the first 8 modes frequencies converged.

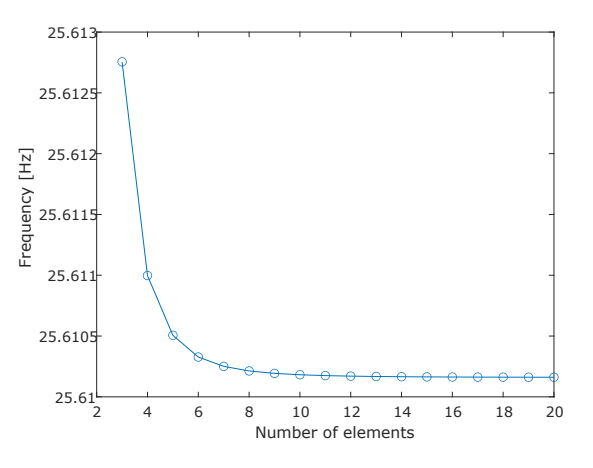


Figure A.1: Convergence study for first bending x-axis

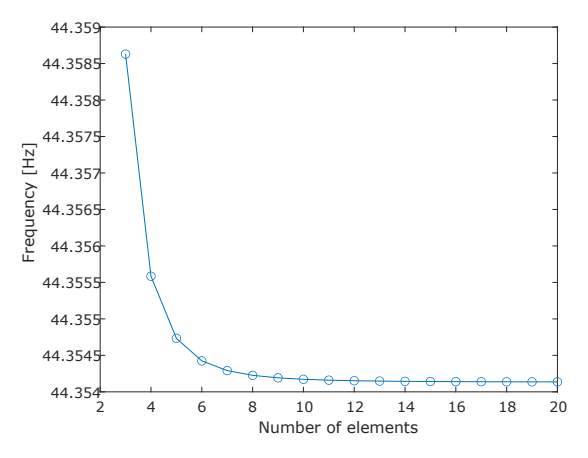


Figure A.2: Convergence study for first bending z-axis

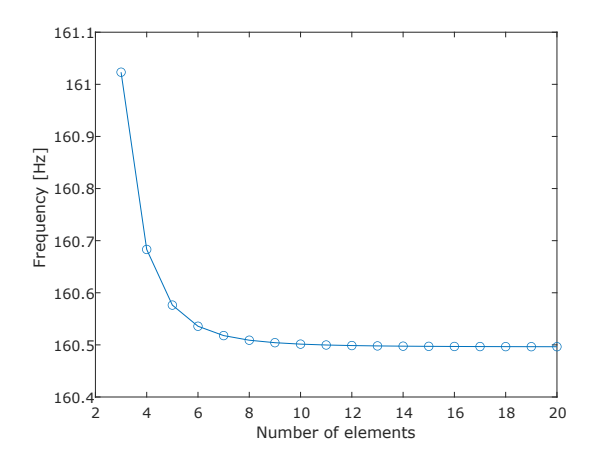


Figure A.3: Convergence study for second bending x-axis

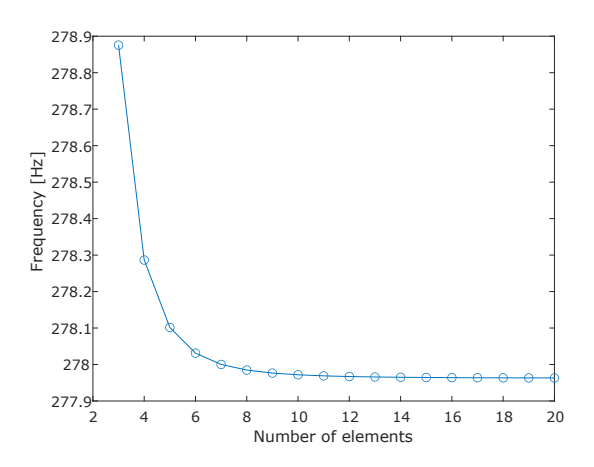


Figure A.4: Convergence study for second bending z-axis

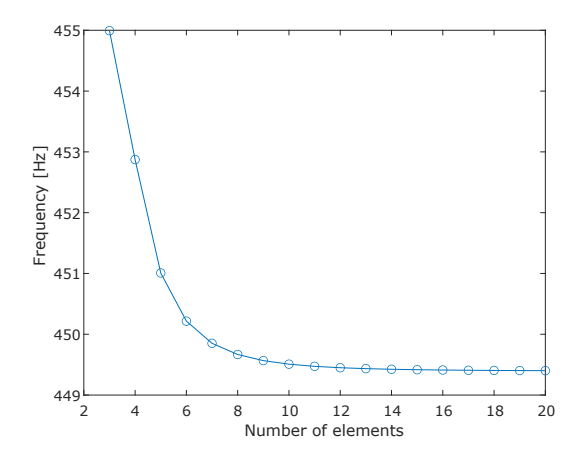


Figure A.5: Convergence study for third bending x-axis

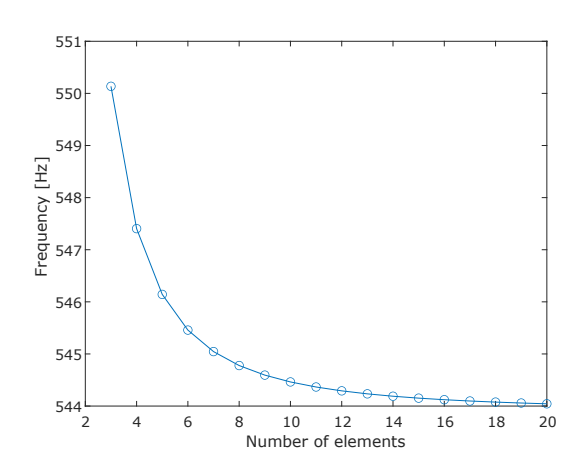


Figure A.6: Convergence study for first torsion

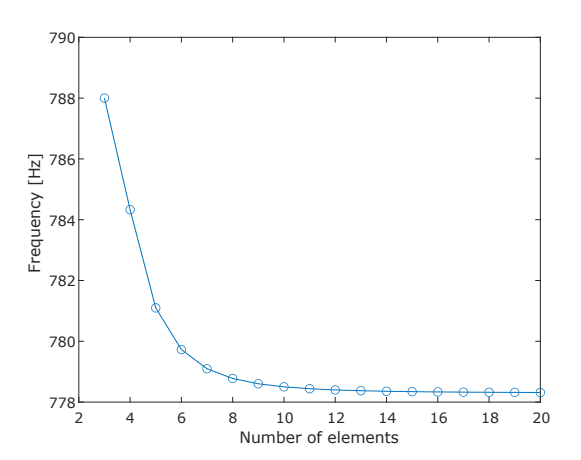


Figure A.7: Convergence study for third bending z-axis

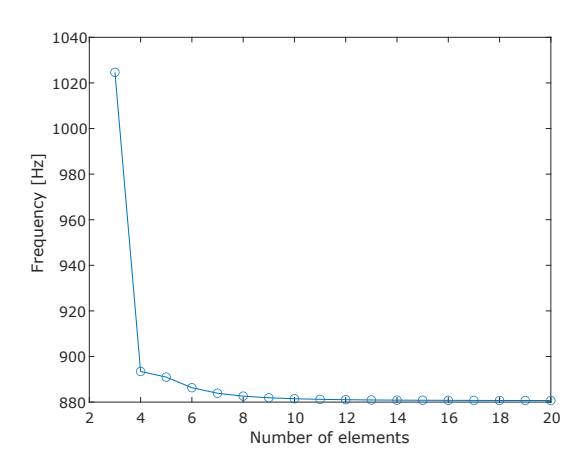


Figure A.8: Convergence study for fourth bending x-axis



Structural mode shapes

In this appendix, the mode shape of the first 8 structural modes of the studied cantilever beam are presented using software Ansys.

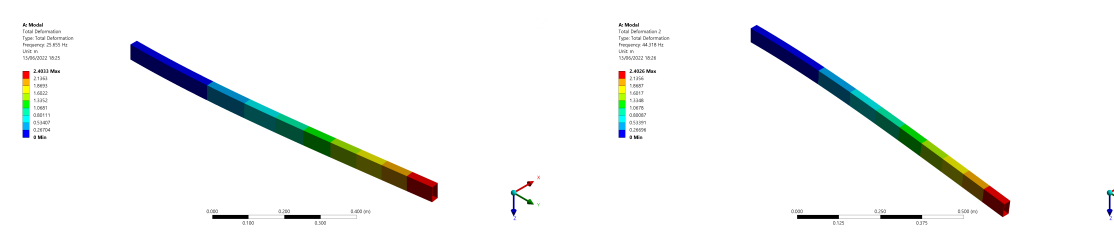


Figure B.1: Mode shape of first bending x-axis

Figure B.2: Mode shape of first bending z-axis

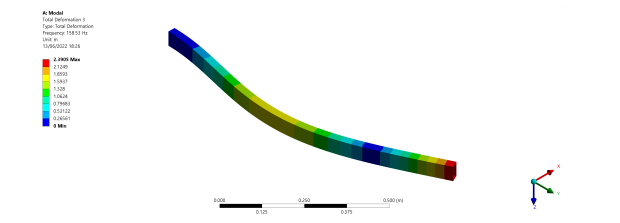


Figure B.3: Mode shape of second bending x-axis

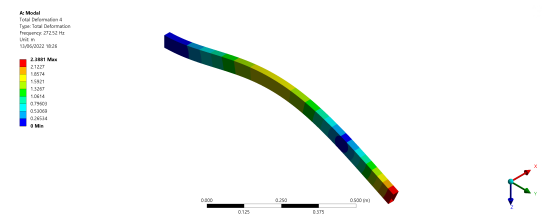


Figure B.4: Mode shape of second bending z-axis

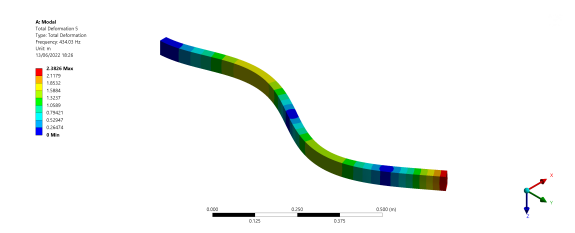


Figure B.5: Mode shape of third bending x-axis

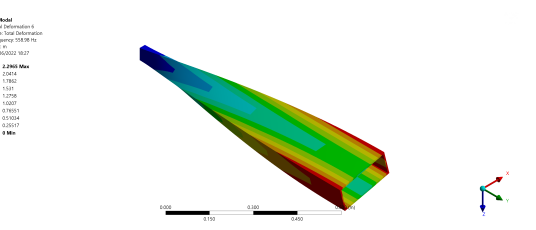


Figure B.6: Mode shape of first torsion

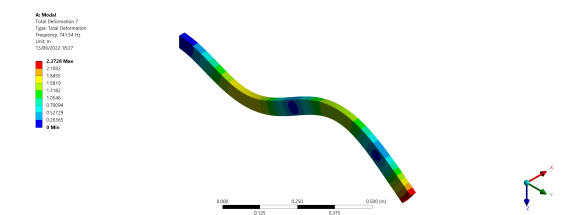


Figure B.7: Mode shape of third bending z-axis

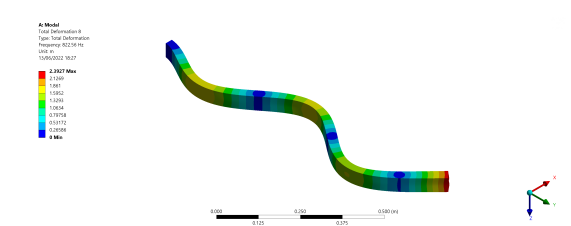
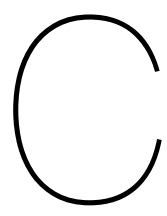


Figure B.8: Mode shape of fourth bending x-axis



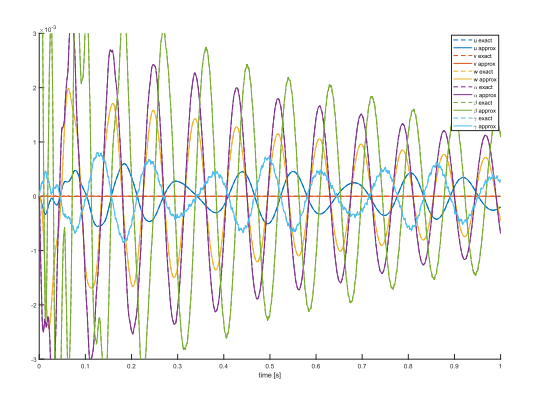
Comparison between forces using the exact solution for a 2 blades propeller and rotational symmetry approximation

Two models were previously obtained for the whirl forces: one for a 2-blade propeller, corresponding to Equation 3.68, and another using rotational symmetry obtained for a 4-blade propeller, corresponding to Equation 3.73. The latter can be adapted for different number of blades.

The advantage of using the rotational symmetry approximation over the solution for a 2-blade propeller is that the forces in Equation 3.74 do not have explicit time dependence, but only depend on the system's degrees of freedom. Then, as there is no explicit time dependence, the stability analysis using state-space representation is straightforward.

On the contrary, if the forces depend explicitly on time, as for the 2-blade propeller forces in Equation 3.68, a time domain analysis will need to be performed and then a post-process will be required to analyze the system stability.

A comparison between the two models was performed in the time domain using the octocopter beam parameters and the octocopter propeller characteristics, for a initial deflection of $\alpha_{tip} = 10^{-2}$, with $\Omega = 4000$ RPM and J = 0.15. The results shown in Figure C.1 and Figure C.2 demonstrate that the symmetry approximation can be applied to the octocopter propeller, as the error is around 2% and the overall stability behavior of the oscillations is the same. Thus, Equation 3.73 will be used for the whirl forces and no time dependence is expected in the aeroelastic matrices.



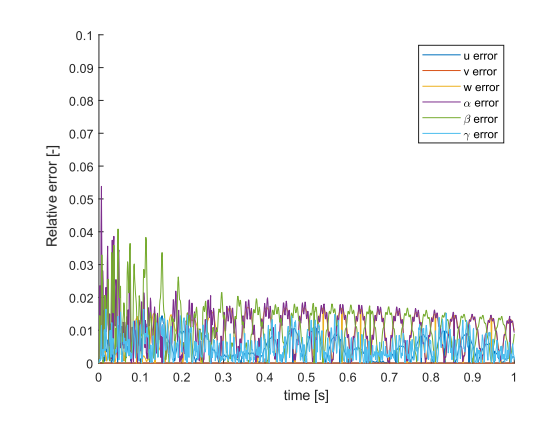


Figure C.1: Comparison between time domain solution using Figure C.2: Relative error between time domain solution using whirl forces exact solution for 2 blades or symmetry approximation

whirl forces exact solution for 2 blades or symmetry approximation

- [1] Houbolt, J. C., & Reed III, W. H. (1962). Propeller-Nacelle Whirl Flutter. *Journal of the Aerospace Sciences*, 29(3). https://doi.org/10.2514/8.9417
- [2] Facts & figures. (n.d.). Retrieved October 15, 2021, from https://www.atag.org/facts-figures.html
- [3] Higgins, R. J. (2021). *Investigation of propeller stall flutter* (Doctoral dissertation). University of Glasgow.
- [4] Stoll, A. M., Bevirt, J., Moore, M. D., Fredericks, W. J., & Borer, N. K. (2014). Drag Reduction Through Distributed Electric Propulsion. 14th aiaa aviation technology, integration, and operations conference. American Institute of Aeronautics; Astronautics. https://doi.org/doi:10.2514/6. 2014-2851
- [5] Čečrdle, J. (2015). Whirl flutter of turboprop aircraft structures. Elsevier, Woodhead Publ.
- [6] DLR Institute of Aeroelasticity. (n.d.). Whirl flutter. Retrieved October 15, 2021, from https://www.dlr.de/ae/en/desktopdefault.aspx/tabid-9667/16675%7B%5C_%7Dread-40599/
- [7] Taylor, E. S., & Browne, K. A. (1938). Vibration Isolation of Aircraft Power Plants. *Journal of the Aeronautical Sciences*, 6(2). https://doi.org/10.2514/8.760
- [8] Flight Safety Fundation. (n.d.). Retrieved October 18, 2021, from https://aviation-safety.net/database/record.php?id=19600317-0
- [9] Retha, E. A. A. (2017). Novel Concepts in Multi-rotor VTOL UAV Dynamics and Stability. https://doi.org/10.1002/9781118928691.ch20
- [10] Abbott Jr, F. T., & Kelley, H. N. (1963). Investigation of Propeller-Power-Plant Autoprecession Boundaries for a Dynamic-Aeroelastic Model of a Four-Engine Turboprop Transport Airplane. (D-1806).
- [11] Reed, Wilmer H., I., & Bland, S. R. (1961). *An Analytical Treatment of Aircraft Propeller Precession Instability* (tech. rep. No. D-659). National Aeronautics and Space Administration. Washington.
- [12] Bland, S. R., & Bennett, R. M. (1963). Wind-tunnel Measurement of Propeller Whirl-flutter Speeds and Static-stability Derivatives and Comparison with Theory (tech. rep. No. D-1807). National Aeronautics and Space Administration. Washington.
- [13] Reed III, W. H. (1966). Propeller-rotor whirl flutter: A state-of-the-art review. *Journal of Sound and Vibration*, *4*(3).
- [14] Richardson, J. R., & Naylor, H. F. W. (1962). Whirl flutter of Propellers with Hinged Blades. *Toronto: Engineering Research Associates Report*, (24).
- [15] Kvaternik, R. G., & Kohn, J. S. (1977). *An experimental and analytical investigation of proprotor whirl flutter* (NASA Technical Paper No. 1047). National Aeronautics and Space Administration.
- [16] Rose, T., & Rodden, B. (1989). Propeller/Nacelle Whirl Flutter Addition to MSC/Nastran.
- [17] Kunz, D. L. (2005). Analysis of proprotor whirl flutter: Review and update. *Journal of Aircraft*, 42(1), 172–178. https://doi.org/10.2514/1.4953
- [18] Liu Xu, V. Q. (2020). *Propeller-Wing Whirl Flutter* (Master's thesis). Delft University of Technology. http://resolver.tudelft.nl/uuid:ac4b57c8-724f-43ce-871c-0bfc326874bb
- [19] X-57 Maxwell. (n.d.). https://www.nasa.gov/specials/X57/
- [20] Beechcraft 1900C N811BE (tech. rep.). (1992). Airline Pilots Association Report.
- [21] Försching, H. W. (1974). *Grundlagen der Aeroelastik*. Springer Berlin Heidelberg. https://doi.org/10.1007/978-3-642-48285-4
- [22] Heeg, J., Stanford, B. K., Kreshock, A., Shen, J., Hoover, C. B., & Truax, R. (2019). Whirl Flutter and the Development of the NASA X-57 Maxwell. *International Forum on Aeroelasticity and Structural Dynamics*.
- [23] Johnson, W. (n.d.). CAMRAD II. http://www.johnson-aeronautics.com/CAMRADII.html
- [24] Bachau. (n.d.). Dymore Solutions. http://www.dymoresolutions.com/
- [25] Ribner, H. S. (1943). *Propellers in yaw* (tech. rep. No. 820). National Aeronautics and Space Administration. Washington.

[26] Sewall, J. L. (1962). *An analytical trend study of propeller whirl instability* (tech. rep. No. D-996). National Aeronautics and Space Administration. Washington.

- [27] Ravera, R. J. (1973). Effects of steady state blade angle of attack on propeller whirl flutter (tech. rep. ADR 06-01-63.1).
- [28] Kvaternik, R. G. (1973). Studies in tilt-rotor VTOL aircraft aeroelasticity (Doctoral dissertation). Case Western Reserve University. Ph. D. Dissertation, June 1973, Case Western Reserve University, Cleveland, Ohio.
- [29] Reed, W. H., Bennett, R. M., & Reed III, W. H. (1963). Propeller whirl flutter considerations for V/STOL aircraft. *Proceedings of the CAL/TRECOM Symposium on Dynamic Loads Problems Associated with Helicopters, Buffalo, USA, Cornell Aeronautical Laboratory*, 1–42.
- [30] Mattaboni, M., Masarati, P., & Mantegazza, P. (2012). Multibody simulation of a generalized predictive controller for tiltrotor active aeroelastic control. *Proceedings of the Institution of Mechanical Engineers, Part G: Journal of Aerospace Engineering*, 226(2), 197–216. http://journals.sagepub.com/doi/10.1177/0954410011406203
- [31] Masarati, P., Piatak, D., Quaranta, G., Singleton, J., & Shen, J. (2008). Soft-Inplane Tiltrotor Aeromechanics Investigation Using Two Comprehensive Multibody Solvers. *Journal of the American Helicopter Society*, 53, 179–192. https://doi.org/10.4050/JAHS.53.179
- [32] Krüger, W. R. (2015). Multibody analysis of whirl flutter stability on a tiltrotor wind tunnel model. *Proceedings of the Institution of Mechanical Engineers, Part K: Journal of Multi-body Dynamics*, 230(2), 121–133. https://doi.org/10.1177/1464419315582128
- [33] Kipling Edenborough, H. (1968). Investigation of tilt-rotor VTOL aircraft rotor-pylon stability. *Journal of Aircraft*, *5*(2), 97–105. https://doi.org/10.2514/3.43915
- [34] Johnson, W. (2013). *Rotorcraft Aeromechanics*. Cambridge University Press. https://doi.org/DOI: 10.1017/CBO9781139235655
- [35] Gennaretti, M., & Greco, L. (2008). Whirl flutter analysis of prop-rotors using unsteady aerodynamics reduced-order models (2016/02/03). The Aeronautical Journal, 112(1131), 261–270. https://doi.org/10.1017/S0001924000002207
- [36] Acree, C. W., Peyran, R. J., & Johnson, W. (1999). Rotor Design for Whirl Flutter: An Examination of Options for Improving Tiltrotor Aeroelastic Stability Margins.
- [37] Loureiro, E., Oliveira, N., Hallak, P., Bastos, F., Rocha, L., Delmonte, R., & Lemonge, A. (2021). Evaluation of low fidelity and CFD methods for the aerodynamic performance of a small propeller. *Aerospace Science and Technology*, *108*, 106402. https://doi.org/10.1016/j.ast.2020.106402
- [38] Sodja, J., De Breuker, R., Nozak, D., Drazumeric, R., & Marzocca, P. (2018). Assessment of low-fidelity fluid–structure interaction model for flexible propeller blades. *Aerospace Science and Technology*, 78, 71–88. https://doi.org/https://doi.org/10.1016/j.ast.2018.03.044
- [39] Kümmel, A., Stuhlpfarrer, M., Pölzlbauer, P., & Breitsamter, C. (2020). Propeller Blade Shape Optimization with a Hybrid BEMT/CFD Approach. In A. Dillmann, G. Heller, E. Krämer, C. Wagner, C. Tropea, & S. Jakirlić (Eds.), *New results in numerical and experimental fluid mechanics xii* (pp. 362–371). Springer International Publishing.
- [40] Branlard, E. (2017). The blade element momentum (BEM) method. *Research topics in wind energy* (pp. 181–211). https://doi.org/10.1007/978-3-319-55164-7_10
- [41] Froude, & W. (1920). On the Elementary Relation Between Pitch, Slip, and Propulsive Efficiency (tech. rep.). National Aeronautics and Space Administration.
- [42] Ledoux, J., Riffo, S., & Salomon, J. (2020). *Analysis of the Blade Element Momentum Theory*. https://hal.archives-ouvertes.fr/hal-02550763 working paper or preprint
- [43] Rankine, W. J. M. (1865). On the mechanical principles of the action of propellers. *Transactions of the Institution of Naval Architects*, *6*, 13–39

 Cited By :189 Export Date: 7 October 2021.
- [44] Froude, R. E. (1889). On the part played in propulsion by differences of fluid pressure. Transactions of the Institute of Naval Architects, 30, 390–405 Cited By :201 Export Date: 7 October 2021.
- [45] Kuik, G., Sørensen, J., & Okulov, V. (2015). Rotor theories by Professor Joukowsky: Momentum theories. *Progress in Aerospace Sciences*, 73, 1–18. https://doi.org/10.1016/j.paerosci.2014.10. 001

[46] Lanchester, F. W. (1915). A contribution to the theory of propulsion and the screw propeller. *Journal of the American Society for Naval Engineers*, 27(2), 509–510. https://doi.org/https://doi.org/10.1111/j.1559-3584.1915.tb00408.x

- [47] Betz, A. (1920). Das Maximum der theoretisch möglichen Ausnutzung des Windes durch Windmotoren. Zeitschrift fur das gesamte Turbinenwesten, 20.
- [48] Joukowsky, N. E. (1920). Windmill of the NEJ type. Transactions of the Central Institute for Aerohydrodynamics of Moscow, 1, 57.
- [49] Glauert, H. (1935). Airplane Propellers. *Aerodynamic theory: A general review of progress under a grant of the guggenheim fund for the promotion of aeronautics* (pp. 169–360). Springer Berlin Heidelberg. https://doi.org/10.1007/978-3-642-91487-4 3
- [50] Rwigema, M. K. (2010). Propeller blade element momentum theory with vortex wake deflection. *27th International congress of the aeronautical sciences.*
- [51] Sørensen, J. N. (2012). Aerodynamic Analysis of Wind Turbines. *Comprehensive Renewable Energy*, 2, 225–241. https://doi.org/10.1016/B978-0-08-087872-0.00209-2
- [52] Manwell, J. F., McGowan, J. G., & Rogers, A. L. (2010). Wind energy explained: theory, design and application. John Wiley & Sons.
- [53] Olczak, A., Stallard, T., Feng, T., & Stansby, P. K. (2016). Comparison of a RANS blade element model for tidal turbine arrays with laboratory scale measurements of wake velocity and rotor thrust. *Journal of Fluids and Structures*, 64, 87–106. https://doi.org/10.1016/J.JFLUIDSTRUCTS. 2016.04.001
- [54] Moriarty, P. J., & Hansen, A. C. (2005). AeroDyn theory manual (tech. rep.). National Renewable Energy Lab., Golden, CO (US).
- [55] Shen, W. Z., Mikkelsen, R., Sørensen, J. N., & Bak, C. (2005). Tip loss corrections for wind turbine computations. *Wind Energy*, 8(4), 457–475. https://doi.org/https://doi.org/10.1002/we.153
- [56] Prandtl, L., & Betz, A. (1927). Vier Abhandlungen zur Hydrodynamik und Aerodynamik. Vier Abhandlungen Zur Hydrodynamik und Aerodynamik, 88–92 Cited By :73 Export Date: 8 October 2021.
- [57] Masters, I., Chapman, J. C., Willis, M. R., & Orme, J. A. C. (2011). A robust blade element momentum theory model for tidal stream turbines including tip and hub loss corrections. *Journal* of Marine Engineering & Technology, 10(1), 25–35. https://doi.org/10.1080/20464177.2011. 11020241
- [58] Wilson, R. E., & Lissaman, P. B. S. (1974). Applied aerodynamics of wind power machines.
- [59] de Vries, O. (1979). Fluid dynamic aspects of wind energy conversion (tech. rep.). Advisory Group for Aerospace Research; Development NEUILLY-SUR-SEINE (France).
- [60] Gur, O., & Rosen, A. (2008). Comparison between Blade-Element models of propellers. The Aeronautical Journal, 112, 689–704. https://doi.org/10.1017/S0001924000002669
- [61] Shen, W. Z., Zakkam, V. A. K., Sørensen, J. N., & Appa, K. (2007). Analysis of Counter-Rotating Wind Turbines. *Journal of Physics: Conference Series*, 75, 12003. https://doi.org/10.1088/1742-6596/75/1/012003
- [62] Kumar, P. S., Bensingh, R. J., & Abraham, A. (2012). Computational Analysis of 30 Kw Contra Rotor Wind Turbine (S. Rehman, S. Li, & A. Bosio, Eds.). ISRN Renewable Energy, 2012, 939878. https://doi.org/10.5402/2012/939878
- [63] Lee, N. J., Kim, I. C., Kim, C. G., Hyun, B. S., & Lee, Y. H. (2015). Performance study on a counter-rotating tidal current turbine by CFD and model experimentation. *Renewable Energy*, 79(1), 122–126. https://doi.org/10.1016/J.RENENE.2014.11.022
- [64] Wang, J., Wang, S., Ding, B., & Cao, Y. (2020). Optimization Design on Hydrodynamic Performance of Counter-Rotating Tidal Turbine Using Blade Element Momentum Theory and CFD.
- [65] Siddappaji, K., & Turner, M. G. (2015). Counter rotating propeller design using blade element momentum theory. *Proceedings of the 22nd ISABE Conference, Phoenix, AZ, USA*.
- [66] Lee, S., Kim, H., Son, E., & Lee, S. (2012). Effects of design parameters on aerodynamic performance of a counter-rotating wind turbine. *Renewable Energy*, 42, 140–144. https://doi.org/10.1016/J.RENENE.2011.08.046
- [67] Hwang, B., Lee, S., & Lee, S. (2013). Optimization of a counter-rotating wind turbine using the blade element and momentum theory. *Journal of Renewable and Sustainable Energy*, *5*(5), 052013. https://doi.org/10.1063/1.4826940

[68] Thiele, M., Obster, M., & Hornung, M. (2019). Aerodynamic Modeling of Coaxial Counter-Rotating UAV Propellers. *VFS*, 8th Biennial Autonomous VTOL Technical Meeting.

- [69] Mahmuddina, F. (2016). The Effect of Flat Plate Theory Assumption in Post-Stall Lift and Drag Coefficients Extrapolation with Viterna Method. *Science and Engineering*, 6.
- [70] Theodorsen, T., Stickle, G. W., & Brevoort, M. J. (1937). *Characterisitics of six propellers including the high speed range* (tech. rep. No. 594). National Aeronautics and Space Administration.
- [71] Airfoil lift and drag polar diagrams. (n.d.). Retrieved February 9, 2022, from http://airfoiltools.com/polar/index
- [72] Aviv, R., & Gur, O. (2005). Propeller Performance at Low Advance Ratio. *Journal of Aircraft J AIRCRAFT*, 42, 435–441. https://doi.org/10.2514/1.6564
- [73] Leishman, J. G., & Ananthan, S. (2008). An optimum coaxial rotor system for axial flight. *Journal of the American Helicopter Society*, *53*(4), 366–381. https://doi.org/10.4050/JAHS.53.366
- [74] Dimitriadis, G. (2017). Introduction to nonlinear aeroelasticity. Wiley.
- [75] Bennett, R. M., & Bland, S. R. (1964). Experimental and analytical investigation of propeller whirl flutter of a power plant on a flexible wing (tech. rep. No. D-2399). National Aeronautics and Space Administration. Washington.
- [76] Katsikadelis, J. T. (2020). The finite element method. *Dynamic analysis of structures* (pp. 359–522). Academic Press. https://doi.org/10.1016/B978-0-12-818643-5.00011-X
- [77] Rao, S. S. (2011). Chapter 9 Analysis of Trusses, Beams, and Frames. In S. S. B. T. -- T. F. E. M. i. E. (E. Rao (Ed.). Butterworth-Heinemann. https://doi.org/https://doi.org/10.1016/B978-1-85617-661-3.00009-X
- [78] Craig, J. J. (2005). *Introduction to Robotics: Mechanics and Control*. Pearson/Prentice Hall. https://books.google.nl/books?id=MqMeAQAAIAAJ